Multidimensional electron beam-plasma instabilities in the relativistic regime

Antoine Bret, Laurent Gremillet and Mark Eric Dieckmann

Original Publication:

Antoine Bret, Laurent Gremillet and Mark Eric Dieckmann, Multidimensional electron beam-plasma instabilities in the relativistic regime, 2010, Physics of Plasmas, (17), 12, 120501-1-120501-36.
http://dx.doi.org/10.1063/1.3514586

Multidimensional electron beam-plasma instabilities in the relativistic regime

A. Bret,[1,a)] L. Gremillet,[2,b)] and M. E. Dieckmann[3,c)]
[1]*ETSI Industriales, Universidad de Castilla-La Mancha, 13071 Ciudad Real, Spain and Instituto de Investigaciones Energéticas y Aplicaciones Industriales, Campus Universitario de Ciudad Real, 13071 Ciudad Real, Spain*
[2]*CEA, DAM, DIF, F-91297 Arpajon, France*
[3]*Department of Science and Technology (ITN), VITA, Linköping University, 60174 Norrköping, Sweden*

(Received 16 July 2010; accepted 21 October 2010; published online 28 December 2010)

The interest in relativistic beam-plasma instabilities has been greatly rejuvenated over the past two decades by novel concepts in laboratory and space plasmas. Recent advances in this long-standing field are here reviewed from both theoretical and numerical points of view. The primary focus is on the two-dimensional spectrum of unstable electromagnetic waves growing within relativistic, unmagnetized, and uniform electron beam-plasma systems. Although the goal is to provide a unified picture of all instability classes at play, emphasis is put on the potentially dominant waves propagating obliquely to the beam direction, which have received little attention over the years. First, the basic derivation of the general dielectric function of a kinetic relativistic plasma is recalled. Next, an overview of two-dimensional unstable spectra associated with various beam-plasma distribution functions is given. Both cold-fluid and kinetic linear theory results are reported, the latter being based on waterbag and Maxwell–Jüttner model distributions. The main properties of the competing modes (developing parallel, transverse, and oblique to the beam) are given, and their respective region of dominance in the system parameter space is explained. Later sections address particle-in-cell numerical simulations and the nonlinear evolution of multidimensional beam-plasma systems. The elementary structures generated by the various instability classes are first discussed in the case of reduced-geometry systems. Validation of linear theory is then illustrated in detail for large-scale systems, as is the multistaged character of the nonlinear phase. Finally, a collection of closely related beam-plasma problems involving additional physical effects is presented, and worthwhile directions of future research are outlined. © *2010 American Institute of Physics*.
[doi:10.1063/1.3514586]

I. INTRODUCTION

A. A brief history of the topic

Beam-plasma systems are ubiquitous in laboratory or space plasmas, and, as a consequence, their analysis makes up a significant part of any textbook on plasma physics. Since Langmuir first suggested in 1925, the existence of oscillations in beam-plasma systems,[1,2] most of the vast literature they have engendered has been devoted to understanding their stability with respect to collective electromagnetic perturbations. In 1948, Pierce[3] demonstrated that unstable oscillations can arise within such systems and thus explained Langmuir's observation. Bohm and Gross[4] then developed a thorough kinetic theory of unstable perturbations propagating along the beam direction. This class of instability was promptly referred to as the now well-known "two-stream instability." Later on, a second class of instabilities was found in 1959 by Fried,[5] who showed that a beam-plasma system may also turn unstable against electromagnetic modulations normal to the flow. Because these unstable modes tend to break up an initially homogeneous beam profile into small-scale current filaments, they are commonly referred to as "filamentation" modes. In his article, Fried mentioned the closely related work of Weibel who, that same year, demonstrated the instability of an anisotropic two-temperature Maxwellian plasma.[6] Although the Weibel and filamentation instabilities have become almost interchangeable in the literature, we will discuss later (Sec. III F) the differences between these processes, and stick here to filamentation to label unstable normal modes in beam-plasma systems.

If perturbations both parallel and normal to the beam flow are potentially unstable, one is naturally prompted to investigate the stability of obliquely propagating modes, since a real-world perturbation consists of an infinite superposition of arbitrarily oriented modes. The problem was soon addressed in the cold-fluid limit,[7–9] and it was found that indeed, the unstable spectrum is truly *multidimensional* [at least two-dimensional (2D)] as arbitrarily oriented perturbations are likely to be unstable.

Pioneering temperature-dependent investigations of the 2D spectrum have been first performed through the electrostatic approximation,[9–11] hence failing to handle the essentially electromagnetic filamentation modes. Simple fluid models, whether covariant[12] or not,[13,14] were subsequently worked out, before comprehensive kinetic treatments[15–18]

[a)]Electronic mail: antoineclaude.bret@uclm.es.
[b)]Electronic mail: laurent.gremillet@cea.fr.
[c)]Electronic mail: mark.e.dieckmann@itn.liu.se.

managed to provide a unified vision of the entire unstable spectrum, further confirmed by particle-in-cell simulations.[19–23]

Given the potentially broad unstable spectrum of beam-plasma system, one may wonder why early results on gas discharge fluctuations were so readily attributed to a single class of instability, namely, the two-stream one. The reason is that the electrostatic two-stream instability does govern the spectrum under the nonrelativistic conditions characteristic of these early experiments.[18,24] Despite the multidimensional character of the spectrum, beam-aligned modes then grow much faster than the nonparallel ones and determine the onset of the beam evolution. For decades following Fried's and Weibel's seminal papers, nonparallel instabilities hardly received academic attention due to the relative scarcity of physical applications wherein they may have been relevant. This held even in the seemingly favorable context of relativistic electron beam-driven fusion for which one-dimensional (1D) treatments were usually justified by accounting for a strong magnetic field guide.[25–27]

One had to wait the inception of novel inertial confinement fusion (ICF) and astrophysical scenarios in the mid-1990s to see a suddenly increased interest in an accurate understanding of the entire unstable spectrum. This trend is illustrated in Fig. 1, which plots the number of citations received per year by Fried's and Weibel's papers. The two topics responsible for triggering this citation boom are the so-called fast ignition scenario (FIS) for ICF and the astrophysical problems of gamma ray burst (GRB) and cosmic rays. Studies related to these topics have spurred most of the theoretical advances in beam-plasma instabilities over the past 15 years, much effort being put into revisiting, and elaborating, the long-known result[8,9] that, within an extended parameter range, nonparallel modes may initially govern the system evolution.[18,28]

Although this review focuses on FIS and GRB physics, it is worth mentioning that beam-plasma instabilities in the relativistic regime are also relevant for solar flares physics,[29] cosmic magnetic fields generation,[30] magnetic reconnection,[31,32] or even quantum chromodynamics.[33,34]

B. Fast ignition scenario

The FIS was proposed as a strategy to increase the thermonuclear gain in ICF and/or to increase the robustness of standard approaches.[35–37] In conventional ICF, the laser-driven target compression and heating require a high degree of irradiation symmetry so as to limit the growth of hydrodynamical instabilities.[38,39] In order to fulfill drastic symmetry requirements, ICF facilities under construction such as the National Ignition Facility[40] or the Laser Megajoule[41] rely on the so-called indirect drive approach wherein nanosecond laser pulses first hit the inner walls of a high-Z hohlraum containing the DT pellet. The laser-hohlraum interaction then produces a quasihomogeneous x-ray radiation bath, which, by tailoring the incident laser intensity profile, drives a series of shock waves expected, if efficiently synchronized, to both compress and heat the target up to ignition temperatures. By contrast, the FIS proposes to decouple the compression from

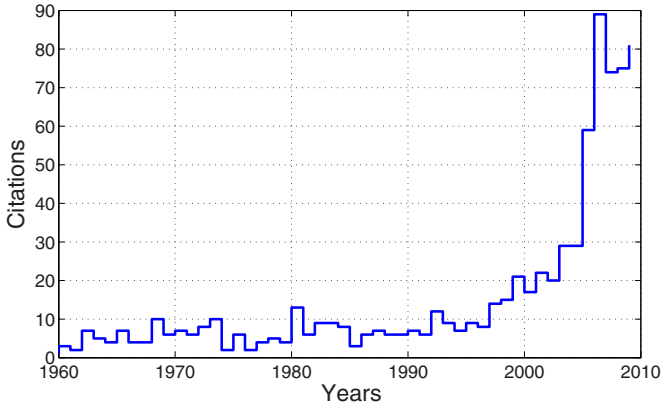

FIG. 1. (Color online) Number of citations per year received by Fried's (Ref. 5) and Weibel's (Ref. 6) 1959 articles until 2009 (from ISI Web of Knowledge).

the heating phase. After the pellet is laser-compressed almost isentropically, heating is achieved by means of an additional laser pulse shot through the plasma corona, as pictured in Fig. 2(a). The petawatt laser pulse propagates up to regions at a few times of the critical density through relativistic hole boring[42,43] or, as now generally considered, by means of a high-Z conical guide.[37,44,45] Along its path, the laser pulse partially converts into a population of relativistic electrons, which, if properly tailored, reach the dense region opaque to the laser light and ignite the thermonuclear reactions.[46] In addition to relaxing symmetry requirements, this approach takes advantage of an isochoric ignition configuration, characterized by a gain higher than the standard isobaric model.[47]

The success of this scheme evidently lies in a quantitative understanding of the transport of the laser-driven electrons through a strongly inhomogeneous plasma.[48] Near the electron acceleration region, the plasma can be assumed collisionless and weakly coupled. By contrast, close to the target center, the beam encounters a collisional, nearly degenerate, and not-so-weakly coupled medium. As a result, the FIS has inspired extensive investigations on the collisionless, relativistic filamentation instability since it is thought to mostly determine the beam divergence near the laser absorption region.[48–58] The resistive version of the filamentation instability[59–61] has also been found influential for the beam energy deposition in the subsequent stage of transport through the moderate-density, yet collisional, part of the DT plasma.

C. Gamma ray bursts and high energy cosmic rays

The second main setting involving relativistic beam-plasmas is the long-standing problem of the origin of high-energy cosmic rays (HECR) and GRBs.[62] By the end of the 1970s, Krymskii,[63] Blandford and Ostriker,[64] Bell,[65,66] and Axford *et al.*[67] found independently that the observed power-law distribution of HECR could be spontaneously generated by Fermi-like acceleration in the vicinity of a collisionless shock, provided there exists a level of wave turbulence strong enough to bounce the particle back and forth across the shock. The basic mechanism of shock-driven particle acceleration, now known as "first-order Fermi acceleration,"

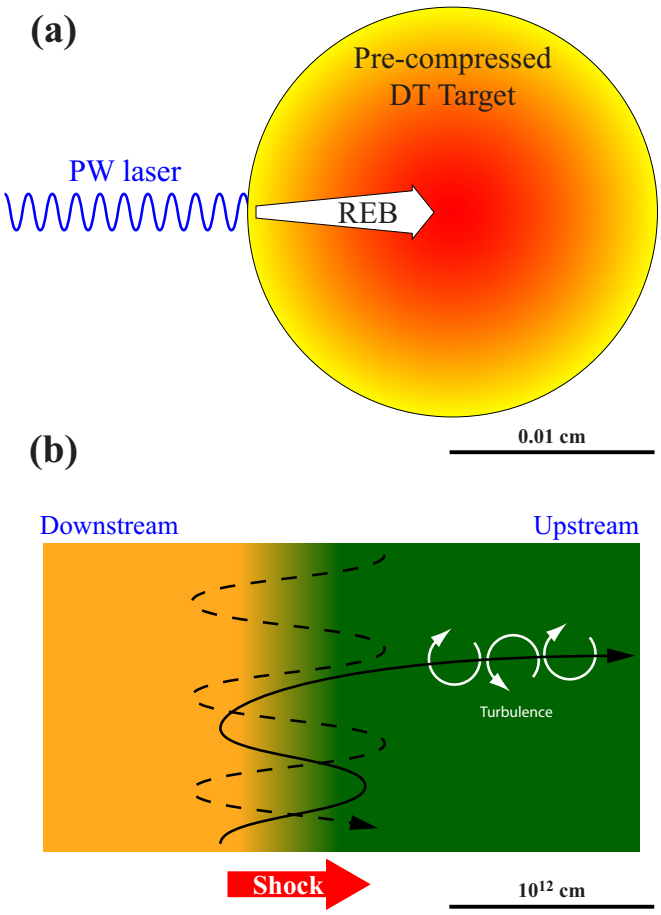

FIG. 2. (Color online) Schematic representation of the FIS and the collisionless shock context. (a) A petawatt laser generates a relativistic electron beam which then deposits its energy near the pellet center. (b) A collisionless shock travels through the interstellar medium. After particles undergo first-order Fermi acceleration (dashed line), some escape upstream (plain line) and trigger turbulence through beam-plasma instabilities. The typical size of the system is indicated in each case.

goes as follows [see Fig. 2(b)]: assume a shock propagates in the interstellar medium (ISM) at velocity V. We here consider a 1D problem with $V \ll c$ for simplicity and work in the interstellar medium rest-frame (see Refs. 68 or Ref. 69, p. 376, for a more general description). Consider a proton with velocity u heading to the shock from the upstream. When bouncing back against it, the proton comes back to the upstream with a velocity $\sim u+2V$. If scattered appropriately in the upstream, it can return to the shock and bounce back again to reach velocity $\sim u+4V$. Fewer and fewer particles experience repeatedly the process, but the more they go through it, the more energy they gain, which explains how the ultimate distribution function should decrease with the energy. This topic has been reviewed by Axford,[70] Drury,[71] and Blandford and Eichler.[72] The role of beam-plasma instability is here threefold.

To start with, particles escaping upstream interact with the ISM. The broad range of unstable modes excited in the process should here produce the turbulence needed for first-order Fermi acceleration. PIC simulations[73–77] have been highly instrumental in validating this scenario for relativistic and nonrelativistic shocks. Beam-plasma instabilities are thus a key part of the loop: Particle acceleration → beam-plasma instabilities → magnetic turbulence → particle acceleration.

But this turbulence plays another role: particles deflected in the electromagnetic fields generate synchrotron radiation, which may be up-scattered by secondary mechanisms, such as inverse Compton radiation, and subsequently observed in the X-range for supernova remnant (SNR) nonrelativistic shocks, and in the γ-range for relativistic shocks. According to the Fireball model,[78,79] the latter γ radiation could explain GRB's emissions (see Refs. 80 and 81 for more details).

The third role played by beam-plasma instabilities is the formation of the shock itself. In a collisionless environment, the instability driven by counterstreaming plasma shells constitutes the sole mechanism through which energy and momentum transfers may take place between the two populations, hence giving rise to a collisionless shock, whether relativistic[82] or not.[83]

D. Principle of particle-in-cell simulations

Particle-in-cell (PIC) simulations[84,85] have long served as powerful tools to test theoretical predictions and access the nonlinear regime of plasma instabilities.[86–93] Even though most of the simulations performed in the late 1960s and 1970s were one-dimensional, one should note that a few of them were already multidimensional. For instance, as early as 1973, Lee and Lampe[92] produced a 2D numerical study of the linear and nonlinear evolution of the relativistic filamentation instability. Its accuracy would be confirmed three decades later through refined simulations accessing the long time-scale of the ion dynamics.[51] By this time, the maximum numbers of macroparticles and time steps were about 10^5 and 1000, respectively. Nowadays, the rapid development of massively parallel supercomputers, together with the good parallelization and scalability of PIC simulations, allows to explore with unprecedented resolution the linear and nonlinear dynamics of large-scale beam-plasma scenarios and bridge the gap between theory and experiment. State-of-the-art PIC codes move up to 10^{11} macroparticles during $\sim 10^5$ time steps.[94]

As sketched in Fig. 3, the PIC technique consists in representing the plasma as a collection of N macroparticles subjected to self-consistent electromagnetic fields. Time and space are discretized so as to resolve the physics and ensure the numerical stability of the (usually explicit) algorithm.[84] For most of the systems under consideration, the mesh size is usually chosen to be of the order of the Debye length, while the time step, which has to fulfill the Courant–Friedrich–Levy condition,[95] is a fraction of the plasma period. Starting from the known particles' positions and velocities $\{\mathbf{x}_i, \mathbf{v}_i\}_{i=1\ldots N}$, the charge and current carried by the particles are projected onto the grid to yield the charge and current densities $\rho(\mathbf{r})$ and $\mathbf{J}(\mathbf{r})$. Maxwell's equations are then solved to update the electromagnetic fields $\mathbf{E}(\mathbf{r})$ and $\mathbf{B}(\mathbf{r})$, which, in turn, are used to advance the particles' positions and velocities through the relativistic Lorentz equation. Any kind of initial particle distribution function $\{\mathbf{x}_i, \mathbf{v}_i\}_{i=1\ldots N}$ can be implemented in accordance with the theoretical model under

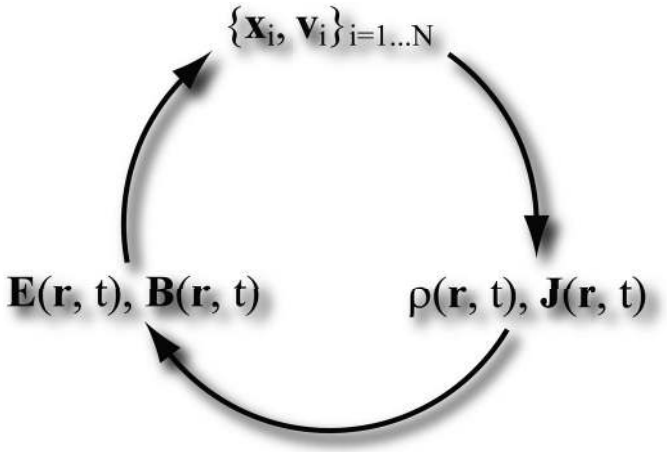

FIG. 3. Basic principle of the particle-in-cell simulation technique.

consideration. Because it solves the one-particle Vlasov equation, the PIC technique is intrinsically suited to modeling collisionless plasmas. Yet kinetic collisional processes can also be described using either Monte Carlo binary[96] or Langevin-type[97] models.

E. Scope of the review and outline

Given the variety of scientifically relevant beam-plasma systems, wherein the effects of thermal spreads, mobile ions, external magnetic field, spatial inhomogeneities, quantum degeneracy, etc., should be (or not) accounted for, we have to restrict the scope of the present article. This review will thus be devoted to the analysis of the 2D spectrum of a relativistic, unmagnetized, and uniform electron beam-plasma system. Alternate beam-plasma systems will be discussed in Sec. VI B. Unless otherwise specified, ions will be considered to form a fixed positively charged background so that only electron-electron instabilities will be dealt with (see Fig. 4). The system will be assumed charge- and current-neutralized in its unperturbed state. Although two-stream and filamentation instabilities will be discussed, the main emphasis will be put on the lesser-known oblique modes and on an unified description of the spectrum.

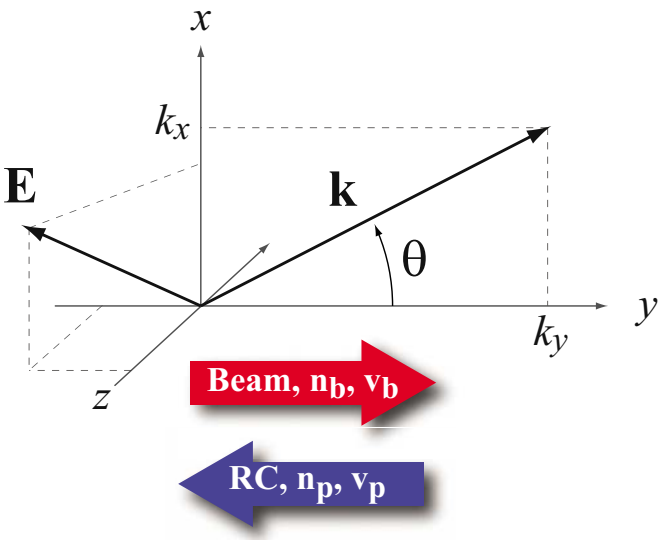

FIG. 4. (Color online) Sketch of the system considered in the present review. "RC" here stands for "return current." Ions are fixed.

Our review will be organized as follows. In Sec. II, we will summarize the linear formalism leading to the kinetic expression of the dielectric tensor. The ensuing general properties of the unstable modes arising within a beam-plasma system will be discussed. Specific electron beam-plasma systems will be considered in Sec. III. Results obtained for the full spectrum in the cold (i.e., monoenergetic) approximation will first be presented. Kinetic effects will then be addressed, first by using simple waterbag distributions, then by resorting to more realistic Maxwell–Jüttner distribution functions. The differences between the somewhat confusable filamentation and Weibel instabilities will also be clarified. In Sec. IV, the properties of the fastest-growing unstable mode will be presented as functions of the system parameters. Depending on the beam-to-plasma density ratio, the beam and plasma temperatures and the beam drift energy, two-stream, filamentation, or oblique modes will be shown to dominate the linear phase. The resulting mode hierarchy will be established for the cold and kinetic cases. Section V will be devoted to an overview of the nonlinear regime and particle-in-cell simulation studies. The fundamental patterns generated during the linear and nonlinear phases of the various instabilities will be first presented, along with the main nonlinear processes responsible for the saturation of the instabilities. Next, we will examine the interplay of multiple unstable modes in large-scale systems. We will show the accurate reproduction of the linear theory predictions and the multistaged evolution of the nonlinear phase. Section VI will report on alternate beam-plasma systems involving additional effects such as ion motion, collisions, or quantum degeneracy. Finally, we will conclude by suggesting a number of potentially fruitful further investigations.

II. LINEAR ANALYSIS: DERIVATION OF THE DIELECTRIC TENSOR FROM THE VLASOV AND MAXWELL EQUATIONS

We here derive the dielectric tensor for an arbitrary homogeneous and infinite beam plasma system composed of N species of charge q_j, mass m_j, density n_j, and mean velocity $\mathbf{v}_j$. Note that the density n_j is here measured in the *laboratory frame*, rather than in the proper frame of the related species as is sometimes the case.[59,98]

This standard calculation is explained at length in a number of plasma physics textbooks,[99–101] and we just here mention the key points. The system is initially charge and current neutral with $\Sigma_j q_j n_j = 0$ and $\Sigma_j q_j n_j \mathbf{v}_j = 0$. There are no equilibrium electromagnetic fields. Each species j is described by its initial distribution function $f_j^0(p)$ with $\int d^3 p f_j^0(p) = 1$. In the absence of collisions, the distribution function $f_j(\mathbf{r},\mathbf{p},t)$ of each species obeys the relativistic Vlasov equation,

$$\frac{\partial f_j}{\partial t} + \mathbf{v}\cdot\frac{\partial f_j}{\partial \mathbf{r}} + q_j\left(\mathbf{E} + \frac{\mathbf{v}\times\mathbf{B}}{c}\right)\frac{\partial f_j}{\partial \mathbf{p}} = 0. \quad (1)$$

The charge ρ and current density $\mathbf{J}$ are computed through

$$\rho = \sum_j n_j q_j \int\int\int d^3p f_j,$$
$$\mathbf{J} = \sum_j n_j q_j \int\int\int d^3p \mathbf{v} f_j, \tag{2}$$

and Maxwell's equations close the system. These equations are then linearized by expressing every quantity ξ, be it scalar or vectorial, in the form

$$\xi = \xi_0 + \xi_1 \exp(\imath \mathbf{k}\cdot\mathbf{r} - \imath\omega t), \quad |\xi_1| \ll |\xi_0|, \tag{3}$$

where ξ_0 denotes the equilibrium initial value and $\imath^2 = -1$. Fluctuations of the form (3) spontaneously arise in a plasma, forming the seed perturbations which can turn unstable or not. Such spontaneous emissions of magnetic field fluctuations were investigated by Yoon for isotropic particle distribution functions[102] and by Tautz and Schlickeiser for an anisotropic distribution function supporting the Weibel instability.[103] With the electromagnetic field varying according to Eq. (3), Maxwell–Faraday's and Maxwell–Ampere's equations read

$$\imath\mathbf{k}\times\mathbf{E}_1 = \imath\frac{\omega}{c}\mathbf{B}_1,$$
$$\imath\mathbf{k}\times\mathbf{B}_1 = -\imath\frac{\omega}{c}\mathbf{E}_1 + \frac{4\pi}{c}\mathbf{J}_1. \tag{4}$$

Eliminating $\mathbf{B}_1$ from Eqs. (4) yields

$$\mathbf{k}\times(\mathbf{k}\times\mathbf{E}_1) + \frac{\omega^2}{c^2}\left(\mathbf{E}_1 + \frac{4\imath\pi}{\omega}\mathbf{J}_1\right) = 0. \tag{5}$$

From this stage, the calculation roadmap consists in using Eq. (1) to express the perturbed distribution functions f_i^1 in terms of f_i^0 and $\mathbf{E}_1$, after eliminating $\mathbf{B}_1$ with Eqs. (4). The first-order current $\mathbf{J}_1$ is then computed from Eqs. (2), and the resulting expression inserted in Eq. (5) to give

$$\mathbf{T}(\mathbf{k},\omega)\cdot\mathbf{E}_1 = 0, \tag{6}$$

with

$$\mathbf{T}(\mathbf{k},\omega) = \frac{\omega^2}{c^2}\boldsymbol{\epsilon}(\mathbf{k},\omega) + \mathbf{k}\otimes\mathbf{k} - k^2\mathbf{I}, \tag{7}$$

where $\mathbf{I}$ is the unity tensor and $\mathbf{k}\otimes\mathbf{k}$ the tensorial product $(k_\alpha k_\beta)$. The dielectric tensor $\boldsymbol{\epsilon}(\mathbf{k},\omega)$ elements read

$$\epsilon_{\alpha\beta}(\mathbf{k},\omega) = \delta_{\alpha\beta} + \sum_j \frac{\omega_{pj}^2}{\omega^2}\int\int\int d^3p \frac{p_\alpha}{\gamma(\mathbf{p})}\frac{\partial f_j^0}{\partial p_\beta} + \sum_j \frac{\omega_{pj}^2}{\omega^2}\int\int\int d^3p \frac{p_\alpha p_\beta}{\gamma(\mathbf{p})^2}\frac{\mathbf{k}\cdot\left(\frac{\partial f_j^0}{\partial \mathbf{p}}\right)}{m_j\omega - \mathbf{k}\cdot\mathbf{p}/\gamma(\mathbf{p})}, \tag{8}$$

where ω_{pj} is the electronic plasma frequency of species j and $\delta_{\alpha\beta}$ is the Kronecker symbol. In the nonrelativistic limit $\gamma = 1$, and for symmetric enough distribution functions, the first sum simplifies as

$$\int\int\int d^3p p_\alpha \frac{\partial f_j^0}{\partial p_\beta} = -\delta_{\alpha\beta}. \tag{9}$$

Equation (8) shows that the Lorentz factor,

$$\gamma(\mathbf{p}) = \sqrt{1 + \frac{p_x^2 + p_y^2 + p_z^2}{m_j^2 c^2}} \tag{10}$$

couples the quadratures along the three momentum axes even though the equilibrium distribution function is separable [i.e., it can be cast under the form $f_j^0(\mathbf{p}) = f_j^x(p_x) f_j^y(p_y) f_j^z(p_z)$]. This mathematical complication, which evidently holds for any kind of coordinate system, has restricted many studies of kinetic plasma instabilities in the relativistic regime to peculiar, and often blatantly unrealistic, distribution functions allowing for a simplified handling of the Lorentz factor, and/or regimes characterized by weak (i.e., nonrelativistic) thermal spreads.[15,16,52,104–109]

Let us emphasize that no assumption whatsoever is made in Eq. (7) about the respective orientations of $\mathbf{k}$ and $\mathbf{E}_1$. Longitudinal (i.e., electrostatic) modes verify $\mathbf{k}\times\mathbf{E}_1 = 0$, while transverse waves verify $\mathbf{k}\cdot\mathbf{E}_1 = 0$. It is well-known that two-stream modes are exactly longitudinal while filamentation modes are mostly transverse (see the discussion at the beginning of Sec. III). A formalism aiming at describing the full unstable spectrum must encompass both instability classes, and therefore be fully electromagnetic. While early results on obliquely oriented modes have been obtained through the longitudinal approximation[8,9] (which, as shown in Ref. 110, allows for an accurate characterization of the dominant modes in the broad parameter range governed by oblique modes), the general kinetic dispersion relation was first numerically solved by Lee and Thode[111] for a special class of diluted, angularly spread monoenergetic beams. The first picture of the full 2D spectrum was obtained a decade later in the cold-fluid regime by Califano *et al.*[28,112,113]

Once a real wave vector $\mathbf{k}$ has been chosen, the dispersion equation follows from Eqs. (6) and (7) and simply reads

$$\det \mathbf{T}(\mathbf{k},\omega) = 0. \tag{11}$$

Denoting $\omega_{\mathbf{k}}$ the complex roots of this equation, the related modes have their electric field lying in the linear subspace defined by $\mathbf{T}(\mathbf{k},\omega_{\mathbf{k}})\cdot\mathbf{E}_1 = 0$. The angle $\widehat{(\mathbf{k},\mathbf{E})}$ follows therefore directly from the formalism instead of being assumed *a priori*.

III. UNSTABLE SPECTRUM OF AN ELECTRON BEAM-PLASMA SYSTEM

Let us consider the system sketched in Fig. 4, namely, a relativistic electron beam of density n_b, mean velocity $\mathbf{v}_b$ aligned with the y axis, and Lorentz factor $\gamma_b = (1 - v_b^2/c^2)^{-1/2}$ flowing through a plasma of ion density n_i and electron density n_p. Ions, of charge Z, are assumed at rest. The system is initially assumed in equilibrium with $n_i = n_p + n_b$ (no net charge) and $n_b\mathbf{v}_b + n_p\mathbf{v}_p = 0$ (no net current). Note that perturbations defined by Eq. (3) are applied to the system "beam+plasma." The beam itself is not the perturbation.

The formalism thus allows for arbitrarily high beam densities, which means the ratio n_b/n_p can vary over the entire range [0,1].

Given the cylindrical symmetry of the model distribution functions under consideration, the wave vector of the perturbation can be chosen in the plane (x,y) without loss of generality. For the same reason, dielectric tensor (8) is symmetric, and all off-diagonal terms but ϵ_{xy} vanish. The dispersion equation then reads[15]

$$\begin{vmatrix} \frac{\omega^2}{c^2}\epsilon_{xx} - k_y^2 & 0 & \frac{\omega^2}{c^2}\epsilon_{xy} + k_x k_y \\ 0 & \frac{\omega^2}{c^2}\epsilon_{zz} - k^2 & 0 \\ \frac{\omega^2}{c^2}\epsilon_{xy} + k_x k_y & 0 & \frac{\omega^2}{c^2}\epsilon_{yy} - k_x^2 \end{vmatrix} = 0, \quad (12)$$

yielding straightforwardly

$$\omega^2 \epsilon_{zz} - k^2 c^2 = 0 \quad (13)$$

or

$$(\omega^2 \epsilon_{yy} - k_x^2 c^2)(\omega^2 \epsilon_{xx} - k_y^2 c^2) - (\omega^2 \epsilon_{xy} + k_x k_y c^2)^2 = 0. \quad (14)$$

These expressions bear important consequences on the polarization of the unstable modes that we now detail.

The dispersion equation is found to have two main branches. The first one, defined by Eq. (13), pertains to modes with an electric field along the z axis. Such modes are therefore purely transverse for any $\mathbf{k}=(k_x,k_y)$. The second branch defines modes with an electric field lying within the (x,y) plane, which can be longitudinal, transverse, or in-between. When considering flow-aligned wave vectors with $k_x=0$, the off-diagonal term ϵ_{xy} vanishes and Eq. (14) reduces to

$$(\omega^2 \epsilon_{xx} - k_y^2 c^2)\epsilon_{yy} = 0. \quad (15)$$

Whereas the first factor may yield unstable modes, the remaining dispersion equation $\epsilon_{yy}=0$ defines modes with an electric field aligned with the flow as well. These are the two-stream modes, which are therefore purely longitudinal. If we now consider wave vectors normal to the flow, with $k_y=0$, we recover the dispersion equation for the filamentation instability,

$$\epsilon_{xx}(\epsilon_{yy} - k_x^2 c^2/\omega^2) = \epsilon_{xy}. \quad (16)$$

The simplified dispersion equation,[54,104,114,115]

$$\epsilon_{yy} - k_x^2 c^2/\omega^2 = 0, \quad (17)$$

is therefore valid provided $\epsilon_{xy}(k_x,\omega)=0, \forall (k_x,\omega)$. If this condition holds, the tensor $\mathbf{T}$ is such that the resulting modes correspond to an y-aligned electric field and are therefore purely transverse. Contrary to a common assumption, the filamentation instability is generally *not* purely transverse (i.e., it has a finite electrostatic component), since its dispersion equation is more involved than Eq. (17).[55,61,116,117] Only when the beam and return current are perfectly symmetric (i.e., with the same density, temperature, and drift energies) does the filamentation instability turn truly transverse. In order not to generate any space charge, the beam and return current should pinch at exactly the same rate. But this rate strongly depends on both the thermal spread (since thermal pressure tends to oppose magnetic pinching) and the relativistic inertia (and therefore the Lorentz factors $\gamma_{b,p}$) of the two electron populations. Charge imbalance thus arises whenever these quantities differ. This feature has more than academic interest since it can be proven that in the cold-limit, the growth rate obtained within purely transverse assumption (17) is overestimated by a factor $\propto\sqrt{\gamma_b}$.[117]

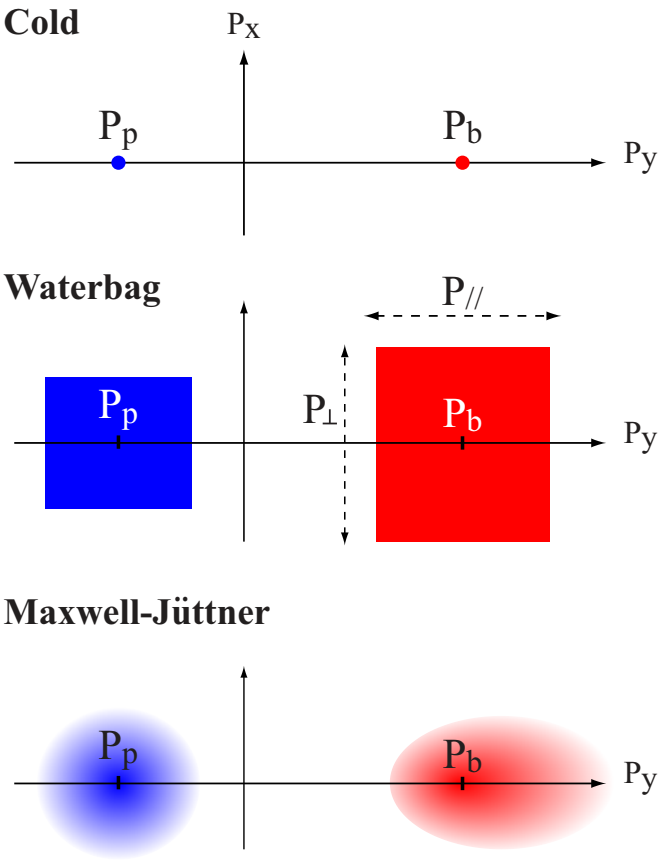

FIG. 5. (Color online) Schematic representations of the distribution functions considered.

The dispersion equations characterizing two-stream and filamentation modes have been analyzed for a large number of model distribution functions, ranging from monokinetic[7,116] to Maxwellian[118–120] through waterbag[52] or kappa[121–123] cases. To date, computations of the full 2D unstable spectrum have been carried out in the cold, waterbag and Maxwell–Jüttner cases sketched in Fig. 5. The main features of these studies will now be reviewed.

A. About the model distribution functions

Solving the dispersion equation requires to choose a distribution function. Within a collisional environment, a Maxwell–Jüttner would seem legitimate since collisions are to relax any distribution to this one.[124] In a magnetized plasma, the use of gyrotropic distributions that only depend on two momentum coordinates may also be justified. However, in the unmagnetized collisionless regime addressed in

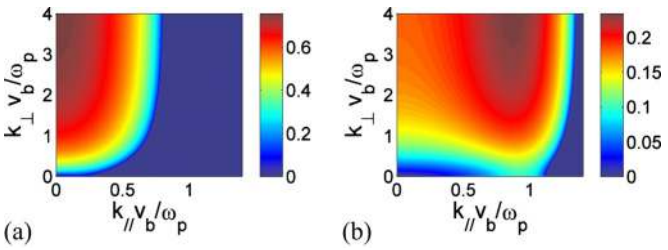

FIG. 6. (Color online) Growth rate maps (ω_p units) in the cold-limit for $\gamma_b=3$ and varying beam densities: (a) $n_b/n_p=1$ and (b) $n_b/n_p=0.1$.

most of this review, there is no obvious physical reason supporting a particular model distribution. Since there is an infinite number of ways to satisfy the vanishing-field equilibrium considered here, the choice of the three model distributions sketched in Fig. 5 is mostly motivated by their mathematical convenience. The cold distribution is the simplest possible choice, able to provide zero-order analytical estimates, whereas waterbag distributions are commonly employed as a first step to explore kinetic effects.[52,61,109,105,125,126] Owing to its smooth shape, the relativistic Maxwell–Jüttner distribution appears as a natural choice for a more realistic treatment of these effects, which, in addition, lends itself to tractable parametric numerical computations (see Sec. III E).

It is worth noting, though, that the generation of a gyrotropic distribution does not necessarily involve an external magnetic field. It may also originate from the wave-particle heating induced by an anisotropic wave spectrum. As will be seen, this is a common configuration for beam-plasma systems. A numerical illustration of such an anisotropic collective heating can be found in Ref. 19 in the case of an oblique-mode dominated system. It has also motivated the analytical and simulation studies of the Weibel instability in the context of magnetic field growth ahead of collisionless plasma shocks.[127] Anisotropic heating could then occur during the interaction between the foreshock electrons and the waves driven by the shock-reflected ion beam. Collisionless shocks are known to produce kappa, i.e., power-law, distributions which have also been investigated in connection with plasmas instabilities.[121–123]

Although studies using cold, waterbag, Maxwellian and kappa distributions make up most of the literature on beam-plasma instabilities, a few works aimed at deriving general properties of arbitrarily distributed systems, generalizing, for instance, well-known theorems such as Penrose's criterion. General results on the filamentation instability have thus been obtained by Tzoufras *et al.*[128] in the case of separable nonrelativistic distributions. Likewise, the Weibel instability has been investigated by Tautz *et al.*,[129–132] who found that the unstable **k** spectrum may be discrete instead of continuous under certain conditions.

B. Cold-limit results

The first step in analyzing the unstable spectrum consists in introducing monokinetic or "cold" distribution functions of the form

TABLE I. Analytical expressions of the maximum growth rate δ and associated wave vector k in the cold-limit for each instability class. For $\alpha=n_b/n_p\ll 1$, see Ref. 7 for two-stream, Ref. 133 for filamentation, and Ref. 8 for oblique. For $\alpha=1$, there is no oblique extremum. See Refs. 134 and 28 for two-stream and filamentation in this case.

	Two-stream	Filamentation	Oblique
$\alpha\ll 1$			
δ/ω_p	$\sim\frac{\sqrt{3}}{2^{4/3}}\frac{\alpha^{1/3}}{\gamma_b}$	$\sim\beta_b\sqrt{\frac{\alpha}{\gamma_b}}$	$\sim\frac{\sqrt{3}}{2^{4/3}}\left(\frac{\alpha}{\gamma_b}\right)^{1/3}$
$k_\parallel v_b/\omega_p$	~ 1	0	~ 1
$k_\perp v_b/\omega_p$	0	$\gg\beta_b$	$\gg 1$
$\alpha=1$			
δ/ω_p	$\frac{1}{2\gamma_b^{3/2}}$	$\beta_b\sqrt{\frac{2}{\gamma_b}}$	…
$k_\parallel v_b/\omega_p$	$\frac{\sqrt{3}}{2\gamma_b^{3/2}}$	0	…
$k_\perp v_b/\omega_p$	0	$\gg\sqrt{2}\frac{\beta_b}{\gamma_b^{3/2}}$	…

$$f_j^0(\mathbf{p})=\delta(p_x)\delta(p_z)\delta(p_y-P_j), \tag{18}$$

where $P_j=m_e\gamma_j v_j$ for the beam and plasma electrons. The corresponding 2D relativistic spectrum has first been explored through the electrostatic approximation in Refs. 8–10. Later on, Califano *et al.*[28,112,113] worked out the first exact calculation, dealing also with the nonlinear regime of the filamentation instability and exploring inhomogeneity effects. Cold-limit results may be retrieved within the present formalism, or equivalently, from linearization of the relativistic cold-fluid equations.[28,112,113] The two growth rate maps pictured in Figs. 6(a) and 6(b) have been computed from dispersion equation (14). They illustrate the main findings of the cold-fluid limit: while filamentation modes dominate for $n_b=n_p$, oblique ones take the lead in the diluted beam regime. As usual, the benefits of the cold approximation lie in the possibility to derive exact or approximate expressions which can serve as a basis for further studies.

The maximum growth rates and associated wave vectors for the two-stream, filamentation, and oblique modes have their expressions reported in Table I in terms of the dimensionless variables,

$$\alpha=\frac{n_b}{n_p},\quad \mathbf{Z}=\mathbf{k}\frac{v_b}{\omega_p},\quad \beta_b=\frac{v_b}{c}, \tag{19}$$

where

$$\omega_p^2=\frac{4\pi n_p e^2}{m_e} \tag{20}$$

is the plasma frequency of the background (i.e., return current) electrons. It is also common to normalize the wave vector to ω_p/c, or ω_e/c, where

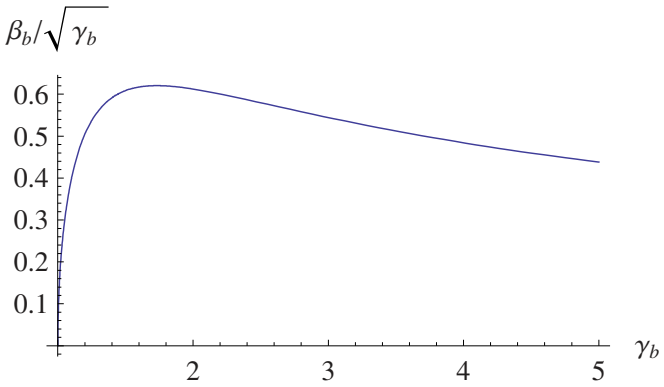

FIG. 7. (Color online) Factor $\beta_b/\sqrt{\gamma_b}$ determining the cold filamentation growth rate for both $n_b=n_p$ and $n_b \ll n_p$ (Table I), in terms of the beam Lorentz factor γ_b. The factor peaks for $\gamma_b=\sqrt{3}$.

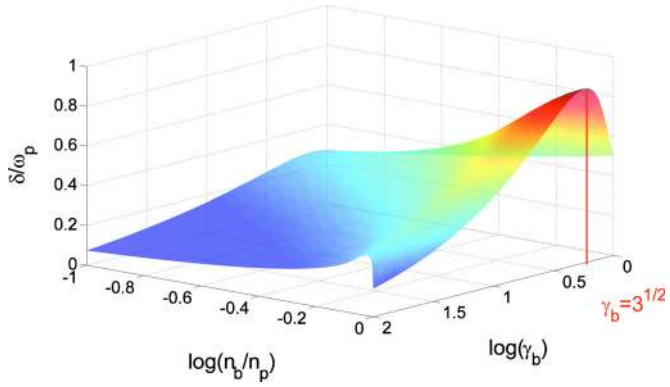

FIG. 8. (Color online) Full spectrum largest growth rate in terms of (α, γ_b). Without any free parameter left, this graph is universal. The largest growth rate the system can experience is $\delta/\omega_p=2/3^{3/4}\sim 0.87$ for $n_b=n_p$ and $\gamma_b=\sqrt{3}$.

$$\omega_e^2=\frac{4\pi(n_b+n_p)e^2}{m_e}=(1+\alpha)\omega_p^2 \tag{21}$$

is the total electron plasma frequency. The dimensionless frequency reads in this text

$$\tilde{\omega}=\frac{\omega}{\omega_p}. \tag{22}$$

For beam-aligned wave vectors, the two-stream instability growth rate reaches a maximum for $k_\parallel v_b/\omega_p\sim 1$ and vanishes for

$$k_\parallel\frac{v_b}{\omega_p}\gtrsim 1+\frac{3}{2}\alpha^{1/3}. \tag{23}$$

In the normal direction, the filamentation growth rate reads $\delta\sim k_\perp v_b\sqrt{\alpha/\gamma_b}$ for $k_\perp\ll\omega_p/c$.[133] In the opposite limit, the growth rate saturates to the value given in Table I. Oblique modes are worth mentioning as long as the growth rate map features an off-axis local maximum. Figure 6(a) suggests that such is not the case for $n_b=n_p$. Indeed, the oblique extremum vanishes above a threshold value of the beam to plasma density ratio which depends on the beam Lorentz factor (see Sec. IV A). Below this threshold, the electrostatic approximation gives the following value for the growth rate along the line $Z_y=1$ (i.e., $k_\parallel=\omega_p/v_b$),[8,9]

$$\frac{\delta}{\omega_p}=\frac{\sqrt{3}}{2^{4/3}}\frac{\alpha^{1/3}}{\gamma_b}\left(\frac{1+\gamma_b^2Z_x^2}{1+Z_x^2}\right)^{1/3}. \tag{24}$$

Let us now comment on the filamentation growth rate. Regardless of the beam density, the factor $\beta_b\gamma_b^{-1/2}$ shows that the instability is quenched at low beam velocities. At relativistic velocities, the increased relativistic inertia of the electrons also acts to inhibit the instability. In the intermediate regime (see Fig. 7), the growth rate reaches a maximum for

$$\gamma_b=\sqrt{3}(\beta_b=\sqrt{2/3}),$$
$$\left.\frac{\beta_b}{\sqrt{\gamma_b}}\right|_{\gamma_b=\sqrt{3}}=\frac{\sqrt{2}}{3^{3/4}}\sim 0.62. \tag{25}$$

The largest filamentation growth rate therefore reads $\delta/\omega_p\sim\sqrt{\alpha}\sqrt{2}/3^{3/4}$ for a diluted beam and $\delta/\omega_p\sim 2/3^{3/4}$ for $n_b=n_p$. The cold-fluid model predicts saturated growth rates in the infinite $k_\perp$ limit for any finite $k_\parallel$. Letting $k_\perp\to\infty$ in the cold dispersion equation, there follows the dispersion equation,

$$(\tilde{\omega}-Z_y)^2\gamma_b+\alpha\beta_b^2[(1+\alpha)^2-\alpha\gamma_b(\tilde{\omega}-Z_y)^2]$$
$$=(\tilde{\omega}+Z_y\alpha)^2\left[\gamma_b(\tilde{\omega}-Z_y)^2-\frac{\alpha}{\gamma_b^2}\right]\gamma_p. \tag{26}$$

Within the cold-fluid limit, this equation is exact for any set of parameters and allows for a simple numerical comparison between the fastest-growing filamentation and oblique modes. Figure 8 plots the maximum growth rate in **k**-space computed numerically from Eq. (26) in terms of (α, γ_b). In the plane $\alpha=1$ ruled by filamentation, the profile corresponding to Fig. 7 is retrieved. In the diluted-beam region where oblique modes prevail, the scaling $(\alpha/\gamma_b)^{1/3}$ is also retrieved. Less expected is that, for large γ_b's, the growth rate is a nonmonotonic function of α. Naive reasoning would suggest that an increased beam density results in a more unstable system. It turns out that from moderate Lorentz factors and onward, the growth rate reaches a maximum for a density ratio slightly smaller than unity. This can easily be understood in terms of the relativistic inertia of the return current. With a density ratio of unity, the Lorentz factor of the return current is strictly equal to the beam one. Lowering the beam density tends to reduce the growth rate, but, at the same time, the rapid drop of the return current's Lorentz factor $\gamma_p=(1-\alpha^2\beta_b^2)^{-1/2}$ yields "lighter," more unstable plasma electrons. For α slightly smaller than unity, the latter effect is found to prevail. The growth rate therefore rises up to an extremum beyond which the $\alpha^{1/3}$ scaling sets in.

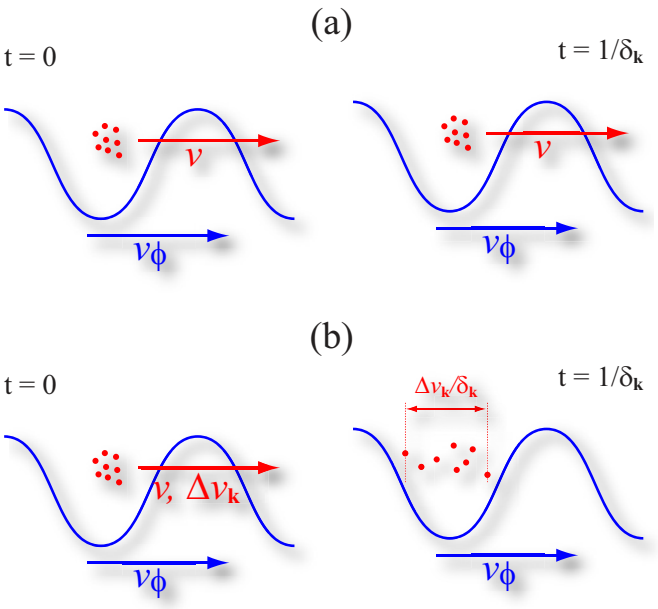

FIG. 9. (Color online) (a) A group of monokinetic electrons initially in phase with a growing wave remains so during one e-folding time. (b) A thermal velocity spread produces a spatial spread at $t=1/\delta_{\mathbf{k}}$, where $\delta_{\mathbf{k}}$ is the growth rate. If this spread is much smaller than the wavelength, the interaction is quasimonochromatic.

C. Validity of the cold-limit results and thermal effects

The domain of validity of cold theory can be simply understood by looking at the underlying mechanism of the instability in the single-mode approximation. Let us consider Fig. 9(a) where a group of monokinetic electrons with velocity v are in phase at time $t=0$ with a growing wave $(\mathbf{k},\omega)$ of growth rate $\delta_{\mathbf{k}}$ and phase velocity $v_\phi=\omega/k=v$. Because all electrons share the same velocity along the wave vector $\mathbf{k}$, they remain in phase with the growing wave during one e-folding time $1/\delta_{\mathbf{k}}$, and the energy exchange is optimum (indeed, they remain locked all along the linear phase until the particles and the mode affect each other). Consider now Fig. 9(b), where electrons have a velocity thermal spread $\Delta v_{\mathbf{k}}$ along the wave direction. Electrons are initially in phase with the wave. After one e-folding time, the velocity spread results in a spatial spread $\sim\Delta v_{\mathbf{k}}/\delta_{\mathbf{k}}$. If this quantity is much smaller than the wavelength $\sim 1/k$, one can consider that the interaction is monokinetic during one e-folding time, and the corresponding growth rate remains very close to that derived in the cold-limit (also referred to as hydrodynamical). We thus derive the approximate condition of validity of the cold approximation,[9]

$$\mathbf{k}\cdot\Delta\mathbf{v} \ll \delta_{\mathbf{k}}. \tag{27}$$

This condition may be fulfilled only in parts of the spectrum. When the inequality is reversed, the instability enters the hot (or kinetic) regime characterized by weaker growth rates.[26,110] A given configuration can therefore be cold with respect to the two-stream instability, and "hot" with respect to filamentation. Note also that the effective velocity spread involved in Eq. (27) depends in practice on the model distribution function. For instance, in the case of Maxwell–Jüttner distribution (see Sec. III E), it was found in Ref. 110 that thermal effects set in when

$$\frac{T_b}{m_e c^2} \gtrsim \frac{3}{2^{10/3}}\left(\frac{n_b}{n_p}\right)^{2/3}\gamma_b^{1/3}\frac{(1+\gamma_b^{-2})^{2/3}}{(1+\gamma_b^{-1})^2}. \tag{28}$$

The previous reasoning allows to state quite general rules about the sensitivity of the various unstable modes to thermal spreads. In the relativistic regime, the parallel velocity spread is usually much smaller than the transverse one (see Fig. 17). This follows from the relativistic contraction of the velocity distribution against the velocity of light c. Large relativistic energy (or momentum) spreads therefore yield much weaker velocity spreads. Equal energy spreads in the parallel and normal directions yield a parallel velocity spread much smaller than the transverse one. In the waterbag case, the latter is larger than the former by a factor γ_b^2.[135] For the Maxwell–Jüttner distribution in the weak-temperature limit, the factor is rather γ_b.[110] Now, the sensitivity of unstable modes to a given thermal spread depends on their orientation. Transverse spreads do not detune beam electrons from beam-aligned modes, which are therefore weakly affected. Conversely, parallel spreads hardly alter normally developing modes.

To summarize, two-stream modes will be essentially sensitive to the parallel velocity spread, which is usually rather weak, whereas filamentation modes will be mostly affected by the usually much larger transverse velocity spread. As a consequence, oblique modes will be increasingly stabilized by a given beam temperature as they make an increasing angle with the beam direction.

D. Waterbag model, limits, and results

Waterbag distributions (see Fig. 5) have been frequently used in the literature as a first step toward a more elaborate kinetic treatment.[52,105] While they cannot render Landau damping $\propto\partial f/\partial v$ and exaggerate the number of hot particles, they usually allow further analytical calculations than Maxwellian functions and make it easy to model transverse or parallel thermal spreads. Silva *et al.*[52] modeled thermal spread effects on the filamentation instability using transverse waterbags for the beam and the plasma, with no parallel thermal spreads. These calculations have been extended to the full unstable spectrum for nonrelativistic thermal spreads, $\Delta E \ll m_e c^2$.[15,16] Results reported here are valid for any thermal spread. We consider for the beam and the plasma waterbag distribution functions in momentum space,

$$f_j^0 = \frac{\delta(p_z)}{4P_{j\perp}P_{j\parallel}}[\Theta(p_x+P_{j\perp})-\Theta(p_x-P_{j\perp})] \times[\Theta(p_y-P_j+P_{j\parallel})-\Theta(p_y-P_j-P_{j\parallel})], \tag{29}$$

where $\Theta(\sigma)$ is the step function [$\Theta(\sigma)=1$ for $\sigma>0$ and 0 otherwise], P_j the mean momentum drift for the beam and the plasma, and $P_{j\parallel},P_{j\perp}$ the parallel and transverse thermal spreads. The lengthy analytical expressions of tensor elements (8) have been derived and are reported in Appendix A. Note that, instead of the (P_x,P_y) space, alternate waterbag

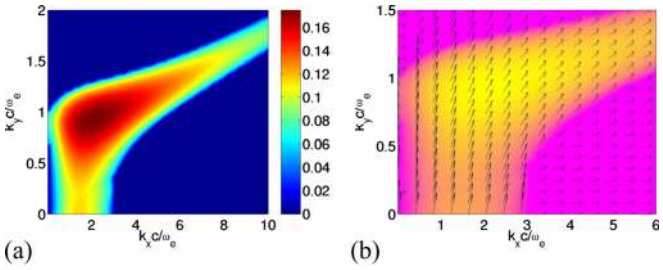

FIG. 10. (Color online) (a) Growth rate map (ω_e units) with the waterbag model for $n_b/n_p=0.1$, $\gamma_b=4$, $P_{b\parallel}=P_{b\perp}=0.2m_ec$, and $P_{p\parallel}=P_{p\perp}=0.1m_ec$. (b) Vector field representation of the corresponding electric fluctuations. The flow is along the y axis.

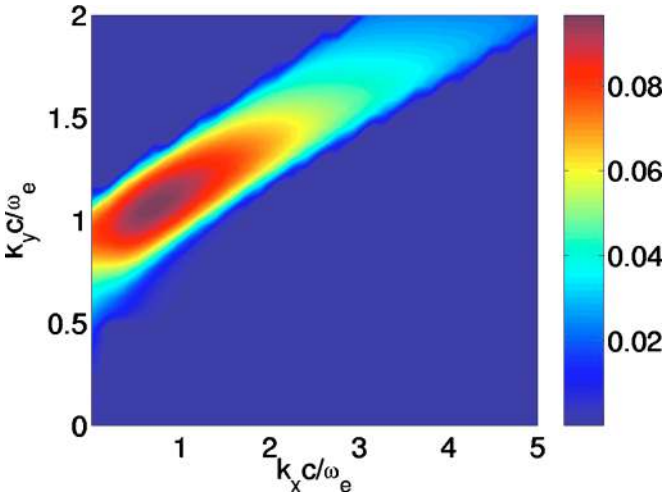

FIG. 11. (Color online) Growth rate map (ω_e units) for $P_{b\parallel}=P_{b\perp}=m_ec$. Other parameters are those of Fig. 10. The flow is along the y axis.

models have also been worked out in momentum cylindrical coordinates[105] or in the (P_y,γ) space.[57]

The limit of validity of the waterbag model can be assessed by comparing the moments of distribution (29) with those of a Maxwellian. Consider the shifted 1D Maxwellian,

$$F_M(p)=\frac{1}{\sqrt{\pi}p_T}\exp\left[-\left(\frac{p-p_0}{p_T}\right)^2\right], \tag{30}$$

and the corresponding waterbag distribution,

$$F_W(p)=\frac{1}{2p_T}[\Theta(p-p_0+p_T)-\Theta(p-p_0-p_T)], \tag{31}$$

both normalized to unity and describing a momentum distribution shifted around p_0 with thermal spread p_T. The instability analysis involves quadratures of the type $\int dpg(p)F(p)$, where g is a function of the momentum. Assuming the functions $g(p)$ can be Taylor expanded over $[p_0-p_T,p_0+p_T]$, we can assess the accuracy of the waterbag approximation by evaluating the discrepancies between the moments $\int dpp^nF(p)$, $n\in\mathbb{N}$, for the two distributions. For $n=0$ and 1, both moments are equal to 1 and p_0, respectively. For $n=2$, the moments differ with

$$\int dpp^2F_M(p)=p_0^2\left(1+\frac{p_T^2}{2p_0^2}\right),$$
$$\int dpp^2F_W(p)=p_0^2\left(1+\frac{p_T^2}{3p_0^2}\right). \tag{32}$$

A proper rescaling of the thermal spread parameter in the waterbag model can allow for the second moments to coincide.[22] But moments for $n>2$ differ anyway, and the parameter measuring the difference is clearly

$$\chi=\frac{p_T}{p_0}, \tag{33}$$

which shows that the waterbag model requires $p_T\ll p_0$. A finer analysis may unravel different criteria in terms of the thermal spread orientation or the part of the $\mathbf{k}$ spectrum under scrutiny. Overall, it turns out that waterbag models can be trusted only for nonrelativistic thermal spreads.

An additional value of the waterbag distributions is the possibility to adjust parallel or perpendicular thermal spreads. The interplay between the various temperature parameters has been reported in Refs. 15 and 16, confirming the heuristic conclusions about thermal effects reached in Sec. III C.

Figure 10(a) displays the 2D growth rate map obtained for $n_b/n_p=0.1$, $\gamma_b=4$, $P_{b\parallel}=P_{b\perp}=0.2m_ec$, and $P_{p\parallel}=P_{p\perp}=0.1m_ec$. In stark contrast to Fig. 6(b), thermal effects now single out one dominant unstable mode instead of a continuum of unstable modes. The location of the dominant mode at $(k_x,k_y)=(2.07,0.93)$ evidently depends on the chosen set of parameters (density ratio, beam drift velocity, beam, and plasma temperatures). The identification of the dominant mode in terms of the parameters is a nontrivial task and gives rise to the concept of "hierarchy map" explained in Sec. IV.

Another noticeable feature of Fig. 10(a) is a narrow oblique strip of unstable modes extending up to $k=\infty$. The critical angle associated with this unstable continuum can be derived exactly[15,16] from the overlapping of the singularities of the dispersion function $\det\mathbf{T}(\mathbf{k},\omega)$. Physically speaking, a singularity results from the resonant coupling between a wave $(\mathbf{k},\omega)$ and those electrons satisfying $\omega-\mathbf{k}\cdot\mathbf{v}_b=0$. When calculating the quadratures involved in the dispersion function with waterbag distributions, the end result is singular for a number (say, l) of frequencies $\{\omega_j^s(\mathbf{k})\}_{j=1\ldots l}$. It can be shown that for some orientation(s) of the wave vector, some singularities overlap, implying a resonant coupling with various electrons populations. As a result, waves propagating in this direction are preferentially amplified. This spurious effect is mitigated with more realistic Maxwell–Jüttner functions, as large-k waves are eventually Landau-damped.

Figure 10(b) shows a vector field representation of the electric fluctuations for the parameters of Fig. 10(a). In the cold-limit, growth rate (24) along the line $k_\parallel v_b/\omega_p=1$ has been derived through the longitudinal (i.e., electrostatic) approximation $\mathbf{k}\times\mathbf{E}_1=0$. According to Fig. 10(b), this approximation also holds in the waterbag case over a broad unstable region encompassing the dominant modes. Figure 10(b) also confirms the finite electrostatic component of filamentation modes discussed at the beginning of Sec. III.

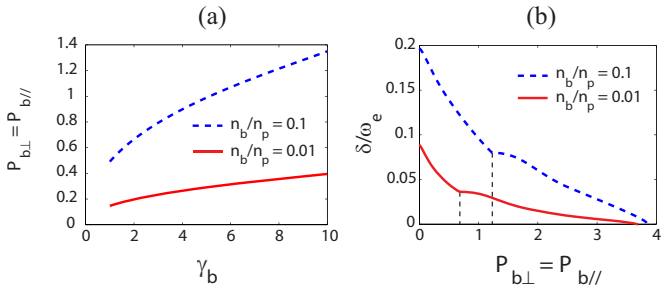

FIG. 12. (Color online) (a) Momentum spread (m_ec units) stabilizing the filamentation instability vs the beam relativistic factor in waterbag model (29) for two beam-to-plasma density ratios. (b) Maximum growth rate (ω_e units) as a function of the beam thermal spread (m_ec units) in the waterbag model for two beam-to-plasma density ratios. The beam Lorentz factor is $\gamma_b=4$. Parallel and transverse beam spreads are set equal in both cases.

Representative changes brought about by raising the beam momentum spread are depicted in Fig. 11 for $P_{b\|}=P_{b\perp}=m_ec$. The maximum growth rate is then reached closer to the parallel y axis $[(k_x,k_y)=(0.77,1.06)]$, a trend pointed out a long time ago in the electrostatic approximation.[9–11] Besides, the angle between the parallel axis and the oblique unstable ridge is decreased, in qualitative agreement with the low-temperature cases addressed in Refs. 15 and 16. The figure also exhibits a complete suppression of the filamentation instability. Such stabilization can be achieved for waterbag[15,16,52,105] or Maxwellian-like[59,104] distributions, but not with Maxwell–Jüttner functions.[110] Furthermore, the cancelation threshold, when it exists, can be very sensitive to the background plasma distribution (see Ref. 136 and discussion in Sec. III F). The stabilization process requires the thermal pressure to balance the pinching magnetic force, and the largest unstable k_x can be derived heuristically from this physical principle.[52]

For distribution (29), the stabilization condition is given in Appendix B where Eqs. (B1)–(B4) generalize the formula given in Ref. 52 for a simpler waterbag configuration. Figure 12(a) plots the resulting stabilizing momentum spread for two values of n_b/n_p. For the parameters of Figs. 10 and 11, filamentation is stabilized for $P_{b\perp}\geq 0.8$. Note that modest, nonrelativistic transverse spreads suffice to suppress the filamentation at very low ($n_b/n_p\leq 0.01$) beam densities.[52]

The evolution of the maximum growth rate as a function of the beam thermal spread is plotted in Fig. 12(b) for two values of n_b/n_p. Both curves exhibit a transition between a rapidly and more slowly decreasing behavior. The threshold thermal spread, which decreases with the beam density, corresponds to a transition from the oblique regime toward a two-stream-dominated regime.[9,19] This feature will be further discussed in Sec. IV for the case of Maxwell–Jüttner distributions.

The overall relativistic spectrum is weakly sensitive to the parallel momentum spread because of the velocity of light barrier (Sec. III C). In this respect, Figs. 12, which have been computed setting $P_{b\|}=P_{b\perp}$ in Eqs. (B1) and (B2), turn out to be almost independent of $P_{b\|}$. In this respect, Fig. 13 displays two waterbag spectra computed varying only the beam parallel spread with $P_{b\|}=2\times 10^{-2}m_ec$ for Fig. 13(a) and $P_{b\|}=2m_ec$ for Fig. 13(b). The two plots are remarkably similar, although the parallel momentum spread has been multiplied by 100 between them.

As will be shown in Sec. V B, theoretical 2D unstable spectra for waterbag distributions have been successfully checked against PIC simulations.[19–22] Yet a more realistic modeling of relativistically hot systems requires the use of smooth distribution functions, in particular, so as to properly account for the high-k-Landau damping. Such is the topic of Sec. IV.

E. Maxwell–Jüttner calculations

Although derived by Jüttner[137] in 1911, the relativistic generalization of the Maxwellian distribution function has had its validity questioned since the 1980s. These doubts were recently ruled out by molecular dynamics simulations.[124,138] For a beam drifting along the y direction, the so-called Maxwell–Jüttner distribution function in momentum space reads

$$f^0(\mathbf{p})=\frac{\mu}{4\pi\gamma^2K_2(\mu/\gamma)}\exp[-\mu(\gamma(\mathbf{p})-\beta_b p_y)], \tag{34}$$

where $\mu=m_ec^2/k_BT$ is the normalized inverse temperature and K_2 the modified Bessel function of the second kind. There result the following moments:

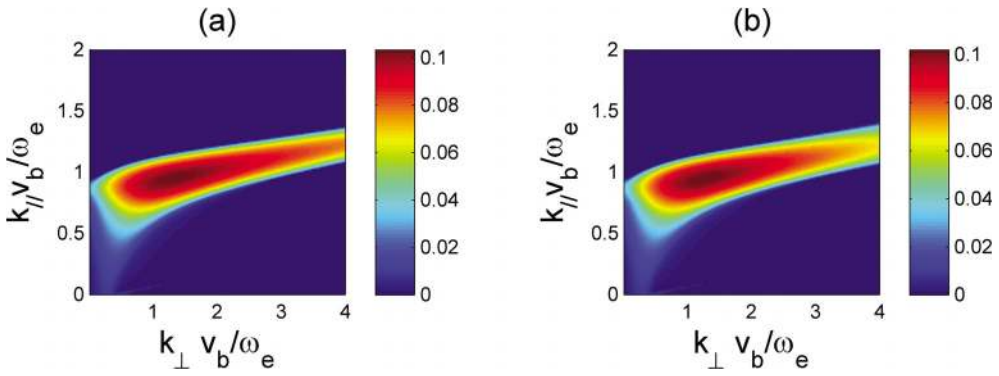

FIG. 13. (Color online) Waterbag spectra (ω_e units) for a beam parallel spread of $P_{b\|}=2\times 10^{-2}m_ec$ (a) and $P_{b\|}=2m_ec$ (b). Density ratio is $\alpha=0.1$, beam Lorentz factor $\gamma_b=10$, and plasma temperatures $P_{p\|}=P_{p\perp}=10^{-2}m_ec$. The beam transverse spread is m_ec in both cases.

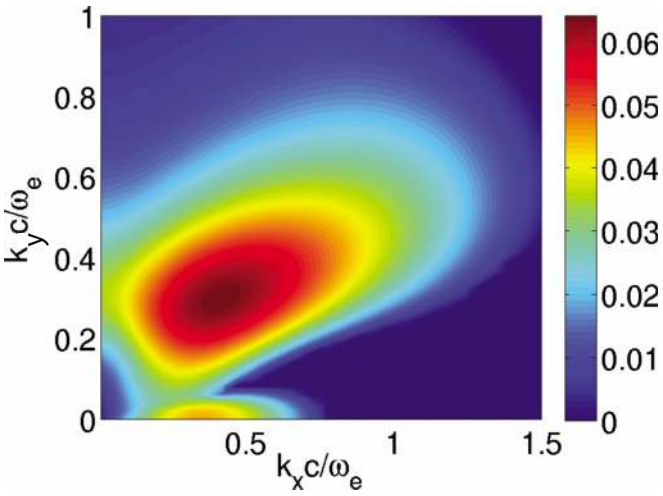

FIG. 14. (Color online) Growth rate map (ω_e units) with the Maxwell–Jüttner model for $n_b/n_p=1$, $\gamma_b=1.5$, $T_b=2$ MeV, and $T_p=5$ keV. The flow is along the y axis.

$$\int\int\int d^3p f^0(\mathbf{p}) = 1,$$

$$\int\int\int d^3p f^0(\mathbf{p}) \frac{p_y}{m\gamma(\mathbf{p})} = \beta_b. \tag{35}$$

An unexpected virtue of the Maxwell–Jüttner distribution is that the triple integrals involved in the dispersion equation can be reduced to much more tractable one-dimensional quadratures using a change of variables mentioned in Ref. 139. The effective calculation, together with the details of the numerical resolution of the dispersion equation in the complex plane, have been reported in Ref. 110. A typical calculation of the growth rate vs. $\mathbf{k}$ is plotted in Fig. 14. The system is characterized by $n_b/n_p=1$, $\gamma_b=1.5$, $T_b=2$ MeV, and $T_p=5$ keV. Oblique modes are found to govern the system, which is a purely thermal effect since cold systems with $n_b/n_p=1$ are ruled by filamentation (see Fig. 18). In contrast to the waterbag model yielding a critical direction unstable for any k's, the unstable spectrum is here bounded. This is a consequence of the Landau damping of high-k modes associated with smooth distribution functions.

The kinetic growth rate scalings for the three instability classes are reported in Table II. The correlation between two-stream and oblique modes is striking, as they only differ through the Lorentz factor scaling.

TABLE II. Kinetic scalings of the maximum filamentation, oblique and two-stream growth rates in the high γ_b- and T_b-limits (Ref. 110). For the cold-fluid scalings, see Table I.

Parameters	Filamentation	Oblique	Two-stream
$\alpha=n_b/n_p$	$\alpha^{3/2}$	α	α
γ_b ($\alpha\ll 1$)	$\gamma_b^{-1/2}$	$\gamma_b^{-1/3}$	γ_b
T_b ($\alpha\ll 1$)	$T_b^{-3/2}$	T_b^{-1}	T_b^{-1}

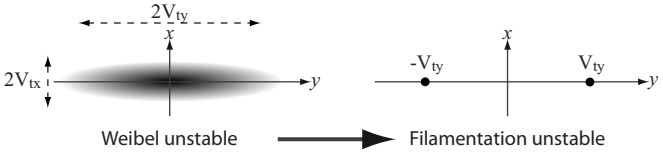

FIG. 15. Typical distribution functions subject to the Weibel and the filamentation instabilities. An anisotropic Weibel-unstable hot plasma can be approximated by a cold filamentation-unstable two-beam system.

F. Filamentation versus Weibel instabilities

Filamentation and "Weibel" instabilities are used almost interchangeably in the literature, and a brief comparative discussion of these two instabilities maybe useful at this stage. Weibel[6] found that purely transverse waves can grow exponentially within an anisotropic plasma at rest. Fried[5] provided a physical interpretation of the Weibel instability by showing that counterstreaming cold beams are also prone to modulations growing normal to the flow. To our knowledge, the oldest occurrence of the term "filamentation instability" in relation with Fried's article is due to Benford in Refs. 140 and 141. The process of beam filamentation has since then been alternatively referred to as filamentation instability,[28,51,59,92,114,142,143] Weibel instability,[52,61,104,112,113,144] or both at the same time.[54,55,145]

Figure 15 explains the basis for the analogy developed by Fried. The anisotropic hot plasma with thermal velocities $V_{ty} \gg V_{tx}$ is unstable in Weibel's sense. The fastest growing modes are found for $\mathbf{k}=k_x\mathbf{e}_x$ (Ref. 146) with a maximum growth rate,[6]

$$\delta_W = \omega_e \frac{V_{ty}}{c}, \quad k_x \gg \frac{\omega_e}{c}, \tag{36}$$

where ω_e is the electronic plasma frequency. Simply put, Weibel modes grow preferentially along the lower-temperature axis. Fried then stated that, by virtue of its extreme anisotropy, this system is similar to the one pictured on the right side. This implies that the system's dynamics should be mainly governed by the group of energetic particles located (in velocity space) around $\pm V_{ty}\mathbf{e}_y$. The cold-fluid instability analysis for this system readily gives the maximum growth rate (see Table I and Ref. 28),

$$\delta_F = \omega_e \frac{V_{ty}}{c}, \quad k_x \gg \frac{\omega_e}{c}, \tag{37}$$

for wave vectors aligned with the normal x axis [see Fig. 6(a)] (the substitution of the total plasma frequency ω_e for the background plasma frequency ω_p explains the disappearance of the factor $\sqrt{2}$ present in Table I). The two systems pictured in Fig. 15 definitely share striking features: both are unstable with respect to an extended range of wave numbers, but the dominant modes are transverse and aligned with the x-axis. Furthermore, the growth rate's expressions are very similar, although not analytically strictly identical for $k_x < \omega_e/c$.[28,146] This equivalence, however, holds only for symmetric beams. Otherwise, several important differences arise between filamentation and Weibel modes. First, Weibel modes are exactly transverse. This was assumed by Weibel

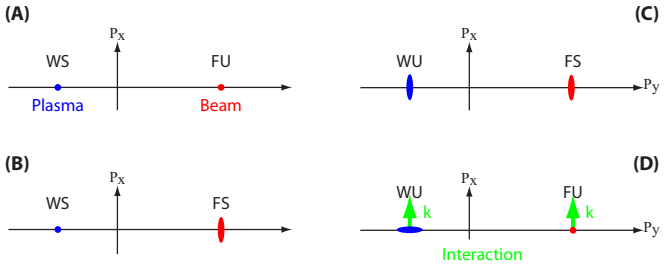

FIG. 16. (Color online) Schematic representation of various settings involving the Weibel and the filamentation instability. (a) The plasma is Weibel stable (WS), the beam is filamentation unstable (FU). (b) The plasma is Weibel stable, the beam is filamentation stable. (c) The plasma is Weibel unstable (WU), the beam is filamentation stable (FS). (d) The plasma is Weibel unstable, the beam is filamentation unstable, and the two instabilities interact.

and demonstrated by Kalman *et al.*[146] By contrast, filamentation modes are usually not transverse. As already mentioned in Sec. III, dispersion equation Eq. (17) for transverse filamentation waves is valid if and only if the tensor element $\epsilon_{xy}(k_x,\omega)=0, \forall (k_x,\omega)$. Within the framework of relativistic kinetic theory, this tensor element does not vanish unless both beams are strictly identical, i.e., have the same density and distribution function. This effect, first discussed in Ref. 116, has since then been further studied[55,117] and is sometimes referred to as "space charge effect."[55,61,147,148]

As a consequence, the filamentation and Weibel instabilities can be switched on and off independently from each other, and even made to interfere with one another (see Fig. 16). In addition to the usual case of a filamentation unstable beam propagating through a Weibel-stable plasma, a filamentation-stable beam may coexist with an anisotropic, Weibel-unstable plasma. But these two instabilities can also be coupled.[15,16] By raising the parallel plasma temperature above its perpendicular one, both the Weibel (plasma) and filamentation (beam) instabilities amplify transverse modulations. In such a configuration, the two instabilities strongly interact, and the filamentation instability gets increasingly resistant to large beam temperatures, until it can no longer be suppressed. As a result, the threshold beam temperature for stabilizing the filamentation instability could be extremely sensitive to the anisotropy of the background plasma.[136] Lazar and Stockem worked extensively on this topic,[120,121,149–151] implementing kinetic calculations for Maxwellian as well as kappa distribution functions. They found a systematic enhancement of filamentation when the plasma is hotter in the beam direction. Conversely, the effect is reversed if the plasma is colder along the beam flow.

G. Phase velocity diagram

The phase velocity v_ϕ of an unstable mode is a key quantity determining how it interacts with a given particle population. For the flow-aligned direction, it is well-known that two-stream modes travel close to the beam speed in the hydrodynamical regime, with $v_b - v_\phi = \mathcal{O}[(n_b/n_p)^{1/3}]$.[4,152] In the kinetic regime, they resonate with the part of the electron

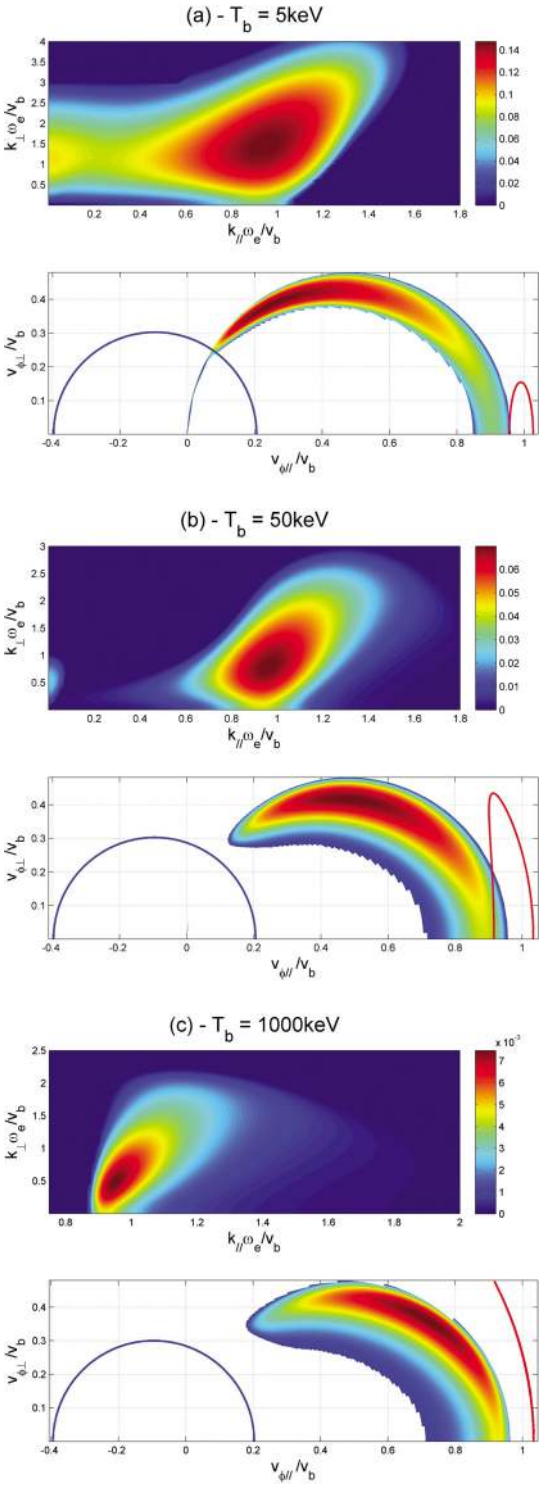

FIG. 17. (Color online) Phase velocity diagrams for a hot relativistic beam passing through a 5 keV plasma. Parameters are $n_b/n_p=0.1$ and $\gamma_b=4$. Beam temperatures are 5 keV (a), 50 keV (b) and 1 MeV (c). Upper plots: growth rate maps (ω_e units). Lower plots: phase velocity diagrams. The beam (red) and plasma (blue) velocity distributions formally extend all over the domain $v<c$. The contours shown are isocontours of the distribution functions enclosing 99% of the particles. For $T_b=1$ MeV, the contour appears like a line.

distribution satisfying $v=v_\phi$, and therefore $v_\phi \sim v_b$ for $\Delta v \ll v_b$. By contrast, filamentation modes with $\mathbf{k} \perp \mathbf{v}_b$ are purely growing modes with $v_\phi=0$.[5,153] The phase velocity vector of an arbitrarily oriented mode of real frequency ω reads

$$\mathbf{v}_\phi = \frac{\omega}{k}\frac{\mathbf{k}}{k}. \tag{38}$$

Normalizing the phase velocity to v_b and introducing the dimensionless wave vector and frequency defined in Eq. (19) gives

$$\frac{\mathbf{v}_\phi}{v_b} \equiv \mathbf{V}_\phi = \frac{\tilde{\omega}}{Z}\frac{\mathbf{Z}}{Z}. \tag{39}$$

The phase velocity diagrams shown in Fig. 17 are constructed by scanning the unstable spectrum (upper frames) and computing the phase velocity of each unstable mode. The resulting points are then plotted in velocity space (lower frames) and colored according to the growth rate. Plotted on the same graphs are the velocity extensions of the beam and plasma distributions, here taken in the Maxwell–Jüttner form with $n_b/n_p=0.1$, $\gamma_b=4$ and varying T_b. The isocontours are chosen to enclose 99% of the electrons of each population. Relativistic effects are obvious for $T_b=1$ MeV as the spread extends almost exclusively in the transverse direction. The temperature dependence exhibited in Figs. 17(a)–17(c) illustrates that qualitatively described in Sec. III C: for $T_b=5$ keV, filamentation modes are still unstable and visible near $\mathbf{v}_\phi=0$ on the phase velocity diagram. At $T_b=50$ keV, most of the intermediate modes between filamentation and the oblique have been stabilized. By $T_b=1$ MeV, all modes with $k_\parallel v_b/\omega_e \lesssim 0.8$ and $v_{\phi\parallel}/v_b \lesssim 0.2$ are damped.

The approximation $\omega \sim \mathbf{k}\cdot\mathbf{v}_b$ (valid in both the weak-velocity spread kinetic limit and the diluted-beam hydrodynamic limit) gives in dimensionless units $\tilde{\omega}=Z\cos\theta$, where θ is the angle between $\mathbf{v}_b$ and $\mathbf{k}$. In polar coordinates, Eq. (39) thus reads $V_\phi(\theta)\sim\cos\theta$, which correctly describes the upper semicircular limit of the weak-temperature case exemplified in Fig. 17(a). In general, though, the monokinetic approximation may not apply over the whole spectrum.

The hydrodynamical or kinetic character of any unstable mode of wave vector $\mathbf{k}$ and phase velocity v_ϕ can be then roughly gauged from the number of particles whose projected velocities on the $\mathbf{k}$ direction $\mathbf{k}\cdot\mathbf{v}/k$ fall close (i.e., within $\sim\delta/k$ according to Fig. 9) to v_ϕ. As a result, thermal effects appear negligible for the fastest-growing parallel mode for $T_b=5$ keV [Fig. 17(a)], whereas they most probably affect it for $T_b=1$ MeV [Fig. 17(c)]. Likewise, these diagrams reveal the kinetic coupling of the dominant oblique modes with particles having $v_\perp<0$. They also evidence the proximity of some plasma electrons with the dominant oblique modes for $T_b=5$ keV. Once amplified to a nonlinear level, these modes may then trap both beam and plasma electrons.[19] Finally, projecting the distribution functions on the filamentation axis (i.e., the vertical axis in Fig. 17) allows to understand why transverse beam spread can affect this instability more than the parallel one.

H. Fluid models

A kinetic treatment of the unstable modes is required when condition (27) is not fulfilled, that is, when there is a significant number of electrons satisfying the resonance condition (see Sec. III G). When the cold approximation is justified, the dispersion relation obtained from the kinetic calculation by setting all distributions to Dirac's δ functions evidently coincides with that derived directly from the cold-fluid equations. These write for each species j,

$$\frac{\partial n_j}{\partial t} + \nabla\cdot(n_j\mathbf{v}_j) = 0, \tag{40}$$

$$\frac{\partial \mathbf{p}_j}{\partial t} + (\mathbf{v}_j\cdot\nabla)\mathbf{p}_j = q_j\left(\mathbf{E} + \frac{\mathbf{v}_j\times\mathbf{B}}{c}\right), \tag{41}$$

where $\mathbf{p}_j=m_j\mathbf{v}_j(1-v_j^2/c^2)^{-1/2}$. The continuity equation readily yields the first-order density perturbations,

$$n_{j1} = n_{j0}\frac{\mathbf{k}\cdot\mathbf{v}_{j1}}{\omega-\mathbf{k}\cdot\mathbf{v}_{j0}}, \tag{42}$$

where subscripts 0 and 1 stand for the equilibrium and first-order quantities, respectively. Linearized momentum equation (41) yields a purely relativistic term on its left-hand side,

$$im_j\gamma_j(\mathbf{k}\cdot\mathbf{v}_{j0}-\omega)\left[\mathbf{v}_{j1} + \gamma_j^2\frac{\mathbf{v}_{j0}\cdot\mathbf{v}_{j1}}{c^2}\mathbf{v}_{j0}\right], \tag{43}$$

where $\gamma_j=(1-v_{j0}^2/c^2)^{-1/2}$. The first-order velocities $\mathbf{v}_{j1}$ are then expressed in terms of $\mathbf{E}_1$ alone, eliminating the n_{j1}'s through Eq. (42) and the magnetic field through Eq. (4). The resulting expressions allow for the calculation of the first-order current, and Eq. (5) eventually gives the dispersion equation. This approach has been used by several authors[9,112,116,154] to analyze the cold unstable spectrum, and their results are evidently those reported in Sec. III B.

Problems arise when a velocity spread is introduced at the kinetic level. A pressure term $-\nabla P_j/n_j$ then appears in the fluid (moment-based) description in the right-hand side of Eq. (41) which, in principle, is a function of higher-order moments whose space-time evolution has also to be simultaneously addressed. There results an infinite system of moment equations that has to be truncated at some point by means of a closure argument, which is made here complicated by the regime of interest being both relativistic and collisionless.

Using the fluid equation requires, in fact, a two step questioning. (1) To which extent can a velocity distribution be replaced by a single, "equivalent" fluid velocity $\mathbf{v}_{j0}$ in Eqs. (42) and (43)? (2) In case the fluid approach is valid, how to close the system of equations?

Question 1 can be answered by means of the phase velocity diagrams of the previous section, and the outcome obviously depends on the kind of mode considered. For example, Fig. 17(b) suggests that for the parameters considered, a fluid approximation aiming at the description of the most unstable oblique mode should be valid for the plasma, but not for the beam.

Turning now to question 2, the isothermal assumption is generally made because the linear analysis of electron beam-plasma instabilities is concerned with the early phase of the system evolution. In this respect, many related studies have employed classical isothermal pressure terms $\nabla P_j=3k_BT_j\nabla n_j$, which are expected to be valid for nonrelativistic temperatures $k_BT_j \ll m_jc^2$ only.[12,50,155–159] More elabo-

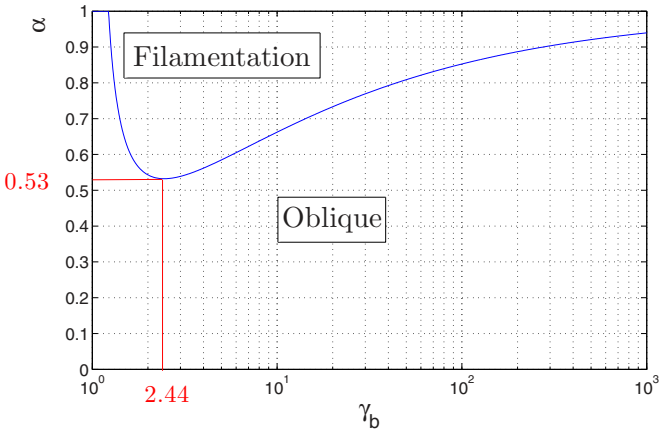

FIG. 18. (Color online) Hierarchy map in the cold-limit in terms of the beam Lorentz factor γ_b and the beam to plasma density ratio $\alpha=n_b/n_p$.

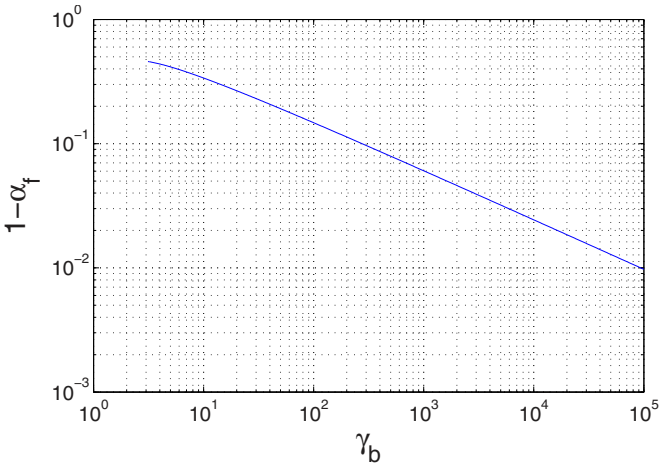

FIG. 19. (Color online) Behavior of $1-\alpha_f$ in terms of γ_b, where α_f is the frontier density ratio.

rate, and generally less tractable, covariant derivations of fluidlike equations have been given in Refs. 160–163, without being thus far exploited in the context of relativistic beam-plasma instabilities. Yet, no matter how involved they may be, fluidlike models are intrinsically flawed by their failure to capture collisionless (Landau) wave-particle resonances and are therefore restricted to describing nonresonant processes such as the quasielectrostatic (parallel or oblique) instabilities in the weak-velocity spread, nonkinetic regime, or, to some extent, the filamentation instability. Simple warm-fluid models may thus render correctly the (weak) beam temperature effects on the filamentation instability,[14,104] while failing to account for *plasma* temperature effects.[14,16] Overall, provided accurate enough closed-form expressions of the relativistic pressure tensor can be worked out, warm-fluid and waterbag approaches share similar domains of validity and yield very similar results.

The much simplified formalism associated with warm-fluid models becomes particularly valuable when addressing magnetized systems for which the kinetic formalism involves coupled three-dimensional (3D) quadratures over the velocity space due to the energy-dependent magnetic Lorentz force. The analytical effort required to compute the magnetized kinetic conductivity tensor is such that it was termed as a "daunting task" by Clemmov and Dougherty (see Ref. 100, p. 335). It is generally found more convenient to employ the fluid equations from the start rather than taking the fluid limit of the kinetic expressions. Such a direct approach was followed to address the 2D unstable spectrum of magnetized beam-plasma systems in the cold[133] or warm[98,164] limits and, lately, to assess quantum chromodynamical instabilities induced by relativistic jets.[34] Only recently was carried out the first fully kinetic treatment of a magnetized beam-plasma system.[165]

IV. DOMINANT MODE: THE HIERARCHY MAP

Given the existence of three distinct instability classes, the question naturally arises about their relative hierarchy in the system parameter space. In other words, given an arbitrary set of beam-plasma parameters, to which instability class does the fastest-growing mode belong? A two-stream governed regime will generate density stripes perpendicular to the flow and excite electrostatic modes. A filamentation regime prompts filaments and electromagnetic modes. Oblique modes are rather electrostatic and produce finite length filaments sometimes referred to as "tilted" filaments.[166,167] The kind of spatial structures[17] and the nature of the excited modes are therefore directly related to the most unstable one.

A. Cold-fluid model

This problem is readily solved in the cold-fluid limit since only two independent parameters are then involved (the beam-to-plasma density ratio and the beam energy).[134] A 2D graph $(\gamma_b,\alpha)\in[1,\infty]\times[0,1]$ therefore suffices to picture the domains governed by each instability class.

Figure 18 shows that filamentation modes govern the high beam density regime while oblique modes dominate for diluted beams. For $\gamma_b=1+\epsilon, \forall\,\epsilon>0$, two-stream modes grow slower than oblique modes, which explains why no part of the graph is dedicated to two-stream modes. The intricate part of the frontier is due to the nonmonotonic behavior of the filamentation instability (see Sec. III B). The lowest point of the filamentation/oblique frontier is reached for

$$\gamma_b = 2.44, \qquad \alpha = 0.53, \tag{44}$$

so that a cold system with $n_b/n_p<0.53$ cannot be governed by the filamentation instability. Another salient feature of the cold-limit hierarchy is the frontier behavior in the ultrarelativistic regime. Figure 18 makes it clear that the ultrarelativistic regime is governed by oblique modes as the frontier between the two domains seems to approach unity for large γ_b. Labeling $\alpha_f(\gamma_b)$ the equation of the frontier, the quantity $1-\alpha_f$ is plotted in Fig. 19 for $\gamma_b\in[20,10^5]$. A power-law scaling is obvious, with the fitting formula

$$\alpha_f \sim 1-0.93\gamma_b^{-0.395}. \tag{45}$$

The coordinates of the most unstable modes in each regime can be derived from Table I. An important point in this re-

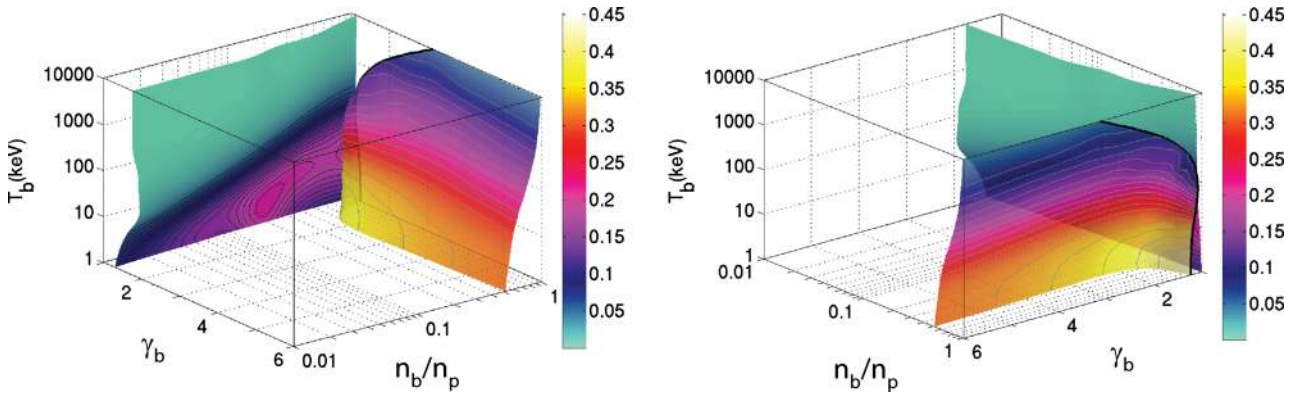

FIG. 20. (Color online) Views from two different angles of the surface boundaries delimiting the domains governed by distinct instability classes in the $(n_b/n_p, \gamma_b, T_b)$ parameter space for a 5 keV plasma. The color code refers to the maximum growth rate in ω_e units. The surface approximately parallel to the plane $\gamma_b=1$ defines the two-stream/oblique frontier (two-stream prevails in the low γ_b limit). The second surface defines the filamentation/oblique frontier (filamentation prevails in the high n_b/n_p limit).

spect is the discontinuous variation of $k_\perp$ during the transition. While the normal component of filamentation vanishes, the normal component of the most unstable oblique mode is finite. Although all functions involved are continuous (the dispersion equation is polynomial), the discontinuity stems from the multidimensional nature of the unstable spectrum. Temperature effects, which are now introduced, amplify this feature.

B. Maxwell–Jüttner kinetic theory

The temperature-dependent analysis[18,110] brings in at least two additional parameters, namely, the beam and plasma temperatures. The introduction of both transverse and parallel thermal spreads would lead to a daunting six-dimensional parameter space. For the sake of tractability, the kinetic mode hierarchy has been determined using the Maxwell–Jüttner functions presented in Sec. III E. Since these functions involve a single thermal parameter, only four parameters are involved in the hierarchy analysis. Once the plasma temperature has been fixed, the domains governed by the various instabilities can be sketched on a 3D graph. While the frontier between two domains is a 1D curve in the cold-limit, the frontiers here are 2D surfaces, which are depicted in Fig. 20 for a 5 keV plasma.

The surface boundary approximately parallel to the $\gamma_b=1$ plane defines the two-stream/oblique transition. As expected, two-stream modes govern the nonrelativistic regime. Through a balance between thermal and relativistic effects, some weakly relativistic systems up to $\gamma_b \sim 2$ turn out to be dominated by two-stream modes. The filamentation/oblique frontier, confined to rather high density ratios, is more involved. Its overall shape along the γ_b direction stems from the behavior of the filamentation growth rate observed in Fig. 7 and commented in Sec. III B. Note that the frontier profile in the plane $T_b=1$ keV matches the 1D curve plotted in Fig. 18. The surface behavior along the T_b axis now results from the sensitivity of the filamentation to the beam temperature. According to the reasoning exposed in Sec. III C, filamentation modes are more vulnerable to the beam thermal spread than oblique and two-stream modes. As a result, for Maxwell–Jüttner distributions, it is found that oblique modes always end up taking over filamentation for high enough beam temperatures.

V. PARTICLE-IN-CELL SIMULATIONS AND NONLINEAR REGIME

A huge wealth of simulation studies of beam-plasma instabilities have been reported over the past 40 years. This section is mostly devoted to a selection of recent PIC simulation results on multidimensional, relativistic beam-plasma systems, performed with the goal of supporting the aforementioned linear theory, as well as extending it to the nonlinear regime.[19–22] In line with our theoretical framework, this review is limited to the evolution of uniform systems, that is, initial-condition problems. Configurations where the beam is injected into a semi-infinite plasma (thus far mostly considered in the GRB context[74,76]) will not be addressed here.

A. Elementary nonlinear structures and saturation mechanisms

Before analyzing the interplay of multiple unstable waves as they grow and saturate in a realistic high-dimensional system, we briefly discuss the elementary nonlinear structures arising during the nonlinear evolution of unstable systems of counterstreaming electron beams. These are the *electron phase space holes*, which evolve out of the electrostatic two-stream instability, and the *current filaments* that develop when the filamentation instability saturates. Understanding the formation of these structures allows for simple analytical modeling of the primary instabilities which have spawned them. We will demonstrate key aspects of their growth and saturation with simulation case studies.

1. Two-stream and oblique instabilities

The parallel two-stream instability that we first consider here results in the growth of sine waves, which give rise to periodic chains of electron phase space holes upon saturation.[177,169] This coherent structuring of the phase space implies that a single mode eventually dominates the unstable

spectrum, which is usually the case in the cold (hydrodynamical) regime.[26] In the opposite kinetic case, the wave spectrum is broad enough to cause the quasilinear relaxation of the beam. This weak-turbulence problem has been tackled in Refs. 9, 10, and 26 where it was found that a proper modeling of the beam relaxation requires accounting for nonlinear ion-induced scattering and parametric processes. The scattering in velocity space of the primary unstable waves outside the beam-resonant region limits their growth and the related beam energy loss.[170,171] This intricate issue is clearly beyond the scope of the present review. In the following discussion, we shall ponder instead on the single-mode regime of the wave saturation.

Electron phase space holes have been observed first in the numerical experiment in Ref. 86 and were identified as nonlinear BGK modes.[172] A local excess of positive charge results in an electrostatic potential, in which the trapped electrons oscillate and form a vortex in phase space. Electrons are trapped if their kinetic energy in the wave frame of reference is not sufficient to overcome the wave potential. Equating the electron kinetic energy and its potential energy in the wave field gives a separatrix, which is analogous to that of the nonlinear pendulum in classical mechanics. It subdivides the phase space into intervals with trapped electrons and untrapped electrons. The separatrix contains an x-point, which corresponds to the unstable equilibrium of the nonlinear pendulum. The oscillation time of the electron goes to infinity as we approach the separatrix.

An estimate of the fraction of the initial beam energy converted into electric field energy can be made by describing the beam dynamics in a coherent wave whose amplitude has grown suddenly from thermal level to a value high enough to trap beam electrons. In the nonrelativistic limit, the beam electrons gyrate almost rigidly in the phase space.[168,173] Assuming their initial distribution function in the wave frame is $f_b(t=0)=\delta(v'-v_b')$ (where $v_b'=v_b-\omega/k$), it becomes after half a trapping period $f_b(t=\tau_{tr}/2)=\delta(v'+v_b')$. In the laboratory frame, the beam has then lost an amount of energy $\Delta W_b=\frac{1}{2}n_b m_e[(\omega/k+v_b')^2-(\omega/k-v_b')^2]\sim 2n_b m_e v_b v_b'$. For a cold diluted beam, we have $v_b'=2^{-4/3}(n_b/n_p)^{1/3}v_b$, which yields the relative energy loss,

$$\frac{\Delta W_b}{W_b}=2\left(\frac{n_b}{2n_p}\right)^{1/3}, \tag{46}$$

where $W_b=\frac{1}{2}n_b m_e v_b^2$ is the initial beam energy density. Since the plasma electrons remain untrapped in the cold regime, the energy loss is equally split into electric field energy and plasma kinetic energy. The electric energy density is therefore $W_E=\langle E^2\rangle/8\pi=\Delta W_b/2$. This expression can be recast as[174]

$$\omega_{BE}=\left(\frac{eE_0k}{m_e}\right)^{1/2}=\frac{2^{3/2}}{9^{1/4}}\delta, \tag{47}$$

in terms of the linear growth rate δ and the (nonrelativistic) electrostatic bouncing frequency ω_{BE} of the electrons trapped close to the potential bottom of the sine wave of amplitude E_0. The above formula simply states that the saturation of the dominant wave occurs when the response of the beam electrons can no longer be treated as a linear perturbation of the ballistic motion.

Applying the previous simple reasoning to the relativistic regime of interest here is straightforward, provided the beam dynamics in the wave frame remains nonrelativistic.[93] Given the phase velocity of the dominant beam-aligned mode $\beta_\phi=\omega/kc=\beta_b[1-(n_b/n_p)^{1/3}/2\gamma_b]$, a Lorentz transform yields the momentum of the beam electrons in the wave frame,

$$\frac{p_b'}{m_e c}=\gamma_\phi\left(\frac{p_b}{m_e c}-\gamma_\phi\gamma_b\right)\sim\frac{\gamma_b\beta_b}{2}\left(\frac{n_b}{2n_p}\right)^{1/3}, \tag{48}$$

where $\gamma_\phi=(1-\beta_\phi^2)^{-1/2}$. The nonrelativistic approximation therefore holds in the wave frame if $\gamma_b\beta_b(n_b/2n_p)^{1/3}\ll 1$. Assuming again a rigid rotation of the beam in the phase space, we have $f_b(t=0)=\delta(p'-p_b')$ and $f_b(t=\tau_{tr}/2)=\delta(p'+p_b')$. The minimum energy of the beam particles in the laboratory frame thus reads $\gamma_b(\tau_{tr}/2)\sim\gamma_\phi\left[1-\frac{1}{2}\gamma_b\beta_b^2(n_b/2n_p)^{1/3}\right]$, hence the fractional energy loss,

$$\frac{\Delta W_b}{W_b}\sim\frac{\gamma_b^2\beta_b^2}{\gamma_b-1}\left(\frac{n_b}{2n_p}\right)^{1/3}, \tag{49}$$

where we have used $\gamma_\phi\sim\gamma_b\left(1-\frac{1}{2}\gamma_b\beta_b^2(n_b/2n_p)^{1/3}\right)$. In the limit $\gamma_b\gg 1$, the energy loss therefore appears to depend on a single parameter, namely,[93]

$$S=\gamma_b\beta_b^2\left(\frac{n_b}{2n_p}\right)^{1/3}. \tag{50}$$

Within the assumption of nonrelativistic wave-frame dynamics ($S\ll 1$), the beam is expected to lose only a small fraction of its incident energy. The opposite limit $S\gtrsim 1$ of strongly relativistic wave-particle interaction is complicated by the energy variation of the bouncing frequency.[26,93] The rigid-motor model then no longer holds: some electrons are decelerated, while others are accelerated so as to get phase-locked with the wave. The number of electrons coherently pumping energy into the wave is therefore lowered, as is the overall energy loss. A semianalyical estimate of the relative energy loss, valid in both weakly and strongly relativistic regimes, has been derived by Thode and Sudan[93] in the case of a square-shaped wave. It reads

$$\frac{\Delta W_b}{W_b}\sim\frac{S}{(S+1)^{5/2}}. \tag{51}$$

This formula predicts a maximum energy loss $\Delta W_b/W_b\sim 0.1$ at $S=2/3$. 1D relativistic PIC simulations have confirmed the dependence of the fractional energy loss on the sole parameter S and agree within 50% with the theoretical estimates.[26,175]

The coupling efficiency of the beam with oblique waves was first assessed numerically by Thode[175] by generalizing the reduced simulation method of O'Neil.[168] This simplified scheme consists in computing numerically the beam electrons' trajectories while treating the plasma as a mere cold dielectric. The evolution of the fixed-k wave is calculated self-consistently through Poisson's equation. For $S<0.45$, the fractional energy loss is found to scale as in Eq. (51) and is mostly due to parallel modes. For $S>0.45$, the beam-wave

interaction is stronger within the range $0<k_\perp<(n_b/n_p)^{1/3}$. The fractional energy loss then proves essentially insensitive to S and equals $\Delta W_b/W_b \sim 0.18$. These results, based on the assumption of a unique unstable wave vector, mainly serve to indicate qualitative trends. As will be shown by the PIC simulations of Sec. V C, a quantitative description of the beam energy loss requires accounting for the temporal change of the orientation of the dominant mode, and therefore a configuration space at least 2D is needed. Also, it will be shown that in the oblique interaction regime, the dominant waves may be slow enough to trap part of the background electrons.

In the postsaturation phase of the parallel instability, neighboring electron phase space holes typically merge or collapse due to the coalescence instability, until only solitary ones remain.[86] A second instability affecting electron phase space holes is the trapped particle sideband instability.[176,177] The oscillation frequency ω_{BE} of the trapped electrons close to the bottom of the electrostatic wave potential is Doppler-shifted by the motion of the electron phase space hole, to give observable upper and lower sidebands.[178] The trapped electrons can couple energy through these sidebands to other wave modes.

Stable equilibrium distributions between the electrostatic potential and the modulated electron phase space distribution can be constructed in form of solitary phase space holes, if the sideband instability is inefficient. Such distribution functions can be found straightforwardly, if the wave potential is planar; the phase space distribution is then a function only of the direction and of the velocity component parallel to the wave vector. Such electron phase space holes and related electrostatic structures are revised in depth in Ref. 179.

Electron phase space holes in more than one dimension are also unstable to transverse instabilities,[88] which are different from the coalescence and sideband instabilities discussed above. The self-focusing instability amplifies any charge modulation orthogonal to the wave vector of a planar electron phase space hole until it is disrupted. A guiding magnetic field can slow down this instability,[180] prolonging the lifetime of the multidimensional electron phase space hole. Despite this multitude of instabilities, the lifetime of electron phase space holes is sufficient to allow for their observation in space[181] and in laboratory plasmas, where proton radiography now permits measurements of their multidimensional electric field distribution at a good time resolution.[182]

2. Filamentation instability

Pioneering PIC simulations of the filamentation instability of counterstreaming electron beams have been performed in Refs. 91, 92, and 183 and in many consecutive numerical studies. The filamentation instability is the fastest growing one if the interacting electron beams have comparable densities and if their speed is at least mildly relativistic (see Figs. 18 and 20). The wave vectors of the fastest-growing waves and the direction vectors of the growing magnetic field are in this case transverse to the beam direction. The displacement current then couples the growing magnetic field to a weak beam-aligned electric field. No transverse electrostatic field grows during the linear growth phase of the filamentation instability, unless the beams are asymmetric.[55,117] However, the Lorentz force imposed by the growing transverse magnetic field on the beam-aligned currents and, more specifically, the magnetic pressure gradient result in the growth of transverse electrostatic fields long before the instability saturates, even if the beams are perfectly symmetric.[184]

The development of this instability can be understood as follows. Individual electrons of both beams interact through their microscopic currents. Electrons moving in opposite directions repel each other, while comoving electrons are attracted to each other. The initial charge- and current-neutral equilibrium is thus unstable. A macroscopic (collective) magnetic field grows by the rearrangement of the beam electrons into spatially separated current filaments, until the electromagnetic fields become sufficiently strong to confine the particles to within a filament. This nonlinear saturation mechanism is termed magnetic trapping.[91] If only one spatial direction orthogonal to the beam direction is resolved, then the current distribution can reach a stationary final state for nonrelativistic beam speeds.[184] Resolving a second orthogonal direction permits the repelling filaments to move around each other and to merge with other attractive filaments to larger ones. The typical filament size increases approximately linearly with time.

Magnetic trapping was early identified as the main mechanism responsible for quenching the initial filamentation growth.[91,183] Similarly to the previous analysis of electrostatic two-stream modes, a rough saturation criterion may be obtained by expressing the fact that the magnetic fluctuations have reached a level high enough to significantly deflect the particle trajectories. To this goal, let us assume that the particles (initially flowing at the velocity $\mathbf{v}_0$) evolve under the influence of a stationary magnetic modulation of amplitude B_0 and wave vector k. Their transverse motion then obeys the equation

$$\frac{d^2x}{dt^2} = \frac{ev_y}{m_e c\gamma} B_0 \sin(kx). \tag{52}$$

Particles near $x=0$ therefore oscillate at the magnetic trapping frequency

$$\omega_{BM} = \left(\frac{ev_0 k B_0}{m_e c \gamma_0}\right)^{1/2}, \tag{53}$$

where the variations in the longitudinal velocity have been neglected. We can assume that the instability linear phase is over when the bouncing frequency becomes of the order of the growth rate $\omega_{BM} \sim \delta$.[52,91,126] There follows the saturated field amplitude,

$$\frac{eB_{\mathrm{sat}}}{m_e \omega_e c} \sim \left\langle \frac{\gamma}{\beta_y} \right\rangle \frac{\omega_e}{kc} \left[\frac{\delta(k)}{\omega_e}\right]^2, \tag{54}$$

where $\langle \gamma/\beta_y \rangle$ denotes an appropriate average of γ/β_y over the particle distribution. Alternative estimates of the stabilized magnetic field can be derived by equating the cyclotron frequency to the growth rate or the gyroradius to the modu-

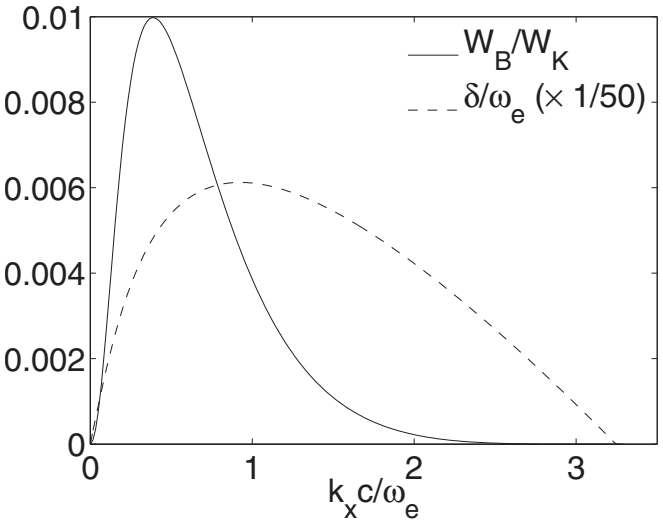

FIG. 21. Theoretical estimate of the saturated magnetic energy density W_B normalized to the total electron energy density W_K (solid) and corresponding growth rate (dashed). A Maxwell–Jüttner model is assumed with $n_b/n_p=0.8$, $\gamma_b=3$, $T_b=100$ keV, and $T_p=5$ keV.

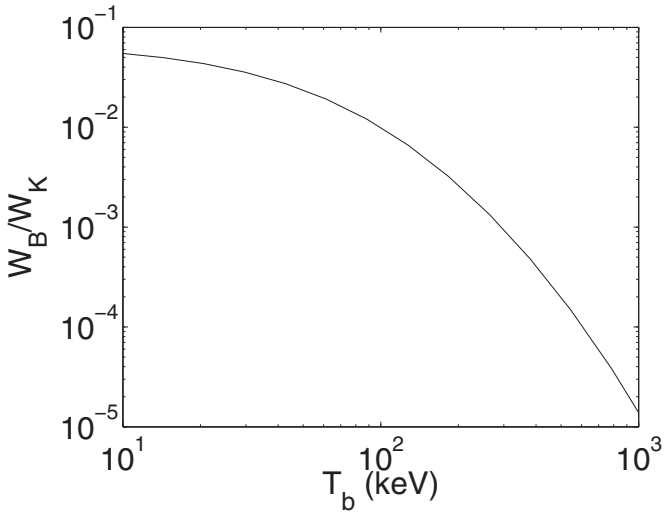

FIG. 22. Predicted saturated magnetic energy density W_B/W_K as a function of the beam temperature T_b. A Maxwell–Jüttner model is assumed with $n_b/n_p=0.8$, $\gamma_b=3$, and $T_p=5$ keV.

lation wavelength.[82,113,185–187] The dominant filamentation mode at saturation may be determined by computing Eq. (54) over the whole unstable spectrum. This is illustrated in Fig. 21 in the case of a Maxwell–Jüttner system with $n_b/n_p=0.8$, $\gamma_b=3$, $T_b=100$ keV, and $T_p=5$ keV. The filamentation instability is the dominant instability for this set of parameters. The solid line plots the k-resolved magnetic energy density normalized to the unperturbed kinetic energy density. The wave vector associated with the maximum magnetic energy is slightly lower than the one maximizing the growth rate (dashed line). This behavior is consistent with the numerically observed shift of the magnetic spectrum toward low k's as the mean transverse temperature of the beam increases due to magnetic deflections.[91,126] The normalized magnetic energy appears to be a decreasing function of T_b as is shown in Fig. 22 for the same parameters as before. Furthermore, as already pointed out in Ref. 52, it amounts to only a small fraction of the initial total electron energy even in the low-temperature limit.

The late-time interplay of filaments has been examined with PIC simulations, which resolve the plane orthogonal to the beam velocity vector,[184,188] and it has been found that the characteristic size of filaments increases approximately linearly with time through the mergers, if the initially spatially uniform electron beams were equally dense. If the initial conditions are such that both electron beams differ substantially in their density ($\alpha \ll 1$), then the electrons of the diluted beam are strongly compressed and this beam expels locally the electrons of the dense beam. The tenuous beam electrons are channeled into beams, which are immersed in the almost uniform background of the electrons of the dense beam. Such current filaments can be remarkably stable,[189] which has been confirmed with PIC simulations.[51,58] Further magnetic pinching of the beam electrons produces a strong electric field accelerating the ions in the radial direction.[51,190]

3. Case studies: PIC simulations

We now illustrate the nonlinear evolution of the two-stream and filamentation instabilities in form of four idealized case studies. The most favorable setup for the growth of the filamentation instability is selected, by modeling two identical counterstreaming electron beams with $\gamma_b=\sqrt{3}$ (Fig. 7). Initially, both spatially uniform electron beams have a Maxwellian velocity distribution with a weak temperature (570 eV) in their respective rest-frames. The total current vanishes in the simulation frame of reference by $n_b=n_p$ and by $v_b=-v_p$. Ions are fixed in all four case studies. We illustrate the nonlinear evolution of the two-stream and filamentation instabilities in form of four idealized case studies.

The 1D simulation of the two-stream instability will be followed by a 1D simulation of the filamentation instability. A third case study addresses the interplay of the two-stream instability and the filamentation instability by selecting a beam velocity vector in the 2D simulation plane. Case study 4 illustrates the filament dynamics, if the beams flow orthogonally to the simulation plane. All three momentum components are resolved, even if the simulations are limited to fewer spatial dimensions. We use 600 grid cells to resolve the x and y directions in the 1D simulations, where we set the box lengths either to $L_x=14c/\omega_p$ or to $L_y=14c/\omega_p$. The 2D simulations resolve a box of size $L_x \times L_y$ by 600^2 grid cells. The beam velocity vectors are parallel to y in case studies 1–3 and parallel to z in case study 4. All boundary conditions are periodic. Here we consider the initial value problem with the electromagnetic and relativistic particle-in-cell code TwoDEM.[191]

The 1D simulation box with the length L_y resolves one two-stream mode with a wave number close to the $k_y v_b/\omega_p \sim \sqrt{3}/2\gamma_b^{3/2}$ and $v_b/c \sim 0.82$ of the fastest growing one (case study 1). We align a box with length L_x with x in case study 2. Figure 23 compares the time evolution of the box-averaged field energy densities computed by these two 1D simulations, which are normalized to the initial electron en-

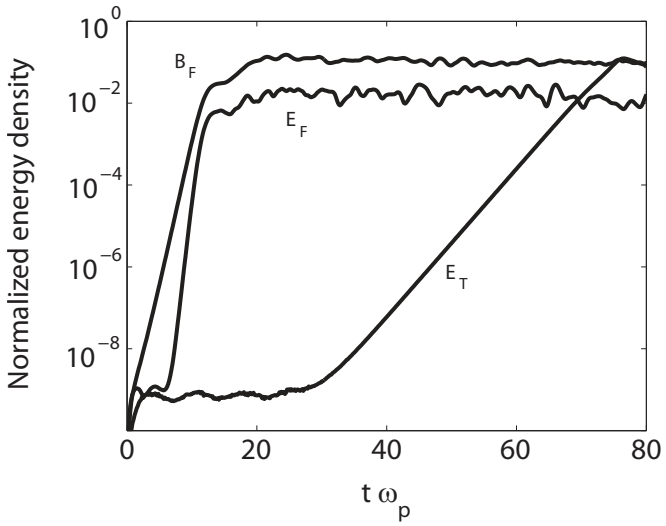

FIG. 23. Normalized box-averaged field energy densities in the 1D simulation: That of E_y driven by the two-stream instability is E_T. The energy densities of the magnetic B_z and electrostatic E_x component of the filamentation instability are denoted as B_F and E_F.

ergy density. The energy density of the electrostatic E_y, which is driven by the two-stream instability, is E_T. That of the magnetic B_z component and the electrostatic E_x that grow due to the filamentation instability are B_F and E_F.

The energy density E_T of the two-stream instability increases beyond the noise levels at $\omega_p t \sim 30$. Even if we take into account that a growth of E_T becomes visible only after it exceeds the noise levels, there is still a time lag. The growth of a charge density wave requires the collective interaction of electrons at least over a spatial scale that is comparable to its wavelength. A signal moving at the light speed crosses a wavelength L_y in about $14/\omega_p$ and no coherent wave can grow before this time. The rapid growth of the filamentation instability can probably be attributed to its electromagnetic character and the much shorter wavelengths in the cold-limit. The beam speed v_b in the simulation is larger than the electron thermal speed by a factor of ~ 25.

The growth phase of the two-stream instability is characterized by an exponential growth rate of the energy density $E_T \propto E_y^2$, that is, well below the B_F and E_F of the filamentation instability, in accordance with the computed linear growth rates. The magnetic energy density B_F grows exponentially up to a value, which is comparable to the saturation value of E_T. The energy density E_F grows after a few ω_p^{-1}, when B_F has already reached a value of $\sim 10^{-5}$. Its exponential growth rate is, however, twice that of B_F in a 1D simulation and it reaches a high value when the filamentation instability saturates. According to the solution of the linear dispersion relation, no E_F should grow in response to the filamentation instability if both beams are perfectly symmetric. Furthermore, if the E_F would grow in the linear regime, then the amplitude of E_x should be proportional to that of B_z. E_F should grow in this case at the same rate as B_F. The source mechanism of E_F must thus be nonlinear.

The growth of this electrostatic field has been discussed for $\gamma_b = 1$, but for otherwise similar initial conditions in Ref. 184. We repeat this discussion here and demonstrate that the nonrelativistic description holds initially qualitatively for the $\gamma_b = \sqrt{3}$ considered here.

Each electron beam is initially a fluid s with the density n_s and mean speed $\mathbf{v}_s \| \mathbf{y}$. Both beams are identical, apart from their velocity direction along y, and we consider only one of them. The fluid evolves according to

$$\partial_t(n_s \mathbf{v}_s) + \nabla \cdot (n_s \mathbf{v}_s \mathbf{v}_s) = \frac{q_s n_s}{m_s}\left(\mathbf{E} + \frac{\mathbf{v}_s \times \mathbf{B}}{c}\right), \tag{55}$$

where the contribution by the thermal pressure has been neglected.

We sum up the two fluid components and consider the right-hand side of the resulting one-fluid momentum equation. The summation gives with $n_e = n_1 + n_2$ and the equal charge and mass of all particles the expression $q_s n_e \mathbf{E}/m_s + (cm_s)^{-1} q_s (n_1 \mathbf{v}_1 + n_2 \mathbf{v}_2) \times \mathbf{B}$. The total plasma current $\mathbf{J}_e = q_s(n_1 \mathbf{v}_2 + n_2 \mathbf{v}_2)$ is rewritten using Ampere's law $\mathbf{J}_e = (c/8\pi)(\nabla \times \mathbf{B})$, where we have neglected the displacement current. The right-hand side of the one-fluid momentum equation then becomes: $q_s n_e \mathbf{E}/m_s + (8\pi m_s)^{-1}(\nabla \times \mathbf{B}) \times \mathbf{B}$, which can be transformed further with the vector equation $(\nabla \times \mathbf{B}) \times \mathbf{B} = -\nabla \mathbf{B}^2/2 + \nabla \cdot (\mathbf{BB})$.

The displacement current is neglected here because its force contribution in the simulation is about an order of magnitude weaker than that due to the magnetic pressure gradient. The fluid equation then becomes with $q_s = -e$

$$\sum_{s=1,2} (\partial_t(n_s \mathbf{v}_s) + \nabla \cdot (n_s \mathbf{v}_s \mathbf{v}_s)) = \frac{-en_e}{m_e}\mathbf{E} - \frac{1}{8\pi m_e} d_x \mathbf{B}^2. \tag{56}$$

We have exploited that in the considered 1D geometry of case study 2, the spatial derivatives $d_y = d/dy$ and $d_z = d/dz$ are zero, so that the magnetic stress tensor vanishes. Only B_z grows due to the filamentation instability and we arrive at the simplified equation of the Lorentz force acting on the current of beam s and modulating the x-component v_{sx} of the beam velocity vector,

$$\sum_{s=1,2} (\partial_t(n_s \mathbf{v}_{sx}) + d_x(n_s v_{sx}^2)) = -\frac{en_e}{m_e}E_x - \frac{B_z d_x B_z}{4\pi m_e}. \tag{57}$$

The growth of B_z implies that the second term on the right hand side is not zero. In the nonrelativistic limit, an electric field grows to an amplitude $E_B = -B_z d_x B_z / 8\pi e n_s$ and both terms cancel. We bring forward more evidence for this connection between B_z and E_x below. A more detailed overview over the plasma dynamics in the 1D simulations is now given.

Case Study 1. The two-stream instability is expected to give rise to a sine wave in the simulation box with length L_y. Lower wave numbers than $2\pi/L_y$ are not resolved and the first harmonic $4\pi/L_y$ does, according to the solution of the linear dispersion relation, not correspond to a fast-growing wave. However, wave harmonics driven by nonlinear processes are always observed in PIC simulations, when the electrostatic waves have reached a high enough amplitude. Figure 24(a) demonstrates that the electrostatic waves saturate at $\omega_p t \sim 70$ and that they oscillate around an equilibrium distribution after that, which is not a monochromatic sine

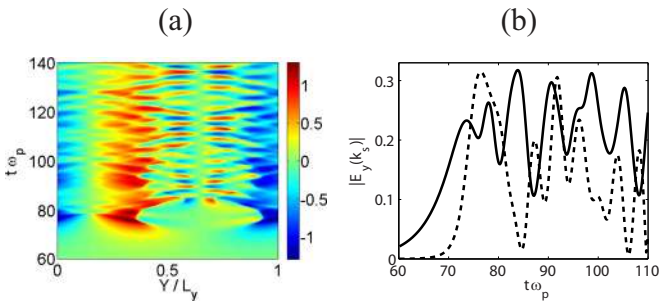

FIG. 24. (Color online) (a) displays the electrostatic $E_y(y,t)$ computed by the 1D simulation of the two-stream instability in units of $\omega_p c m_e/e$. (b) shows the amplitude modulus in the wavenumber $2\pi/L_y$ (solid curve) and in $4\pi/L_y$ (dashed curve).

wave in space. This is confirmed by a comparison of the amplitudes of the first two Fourier modes in the simulation box in Fig. 24(b). The first harmonic grows rapidly during $65<\omega_p t<75$ and it saturates shortly after the initial mode. The amplitudes of both Fourier modes are comparable for $\omega_p t>75$.

The cause of the growth of the first harmonic in our case study is revealed by the electron phase space distribution $f_e(y,p_y,t)$ in Fig. 25. Initially, the mean momentum along p_y of each electron beam oscillates sinusoidally as a function of y, which is a consequence of the electron motion across the electrostatic wave potential. That is, practically sinusoidal at $\omega_p t=63$ [Fig. 24(b)]. The phase velocity of the two-stream instability vanishes for the symmetric beams we consider here, and the wave potential grows aperiodically in the box frame of reference. This is reflected by the steadily increasing amplitude of the electron beam modulation in time, which is visualized in the time-animation of Fig. 25 in the online material.

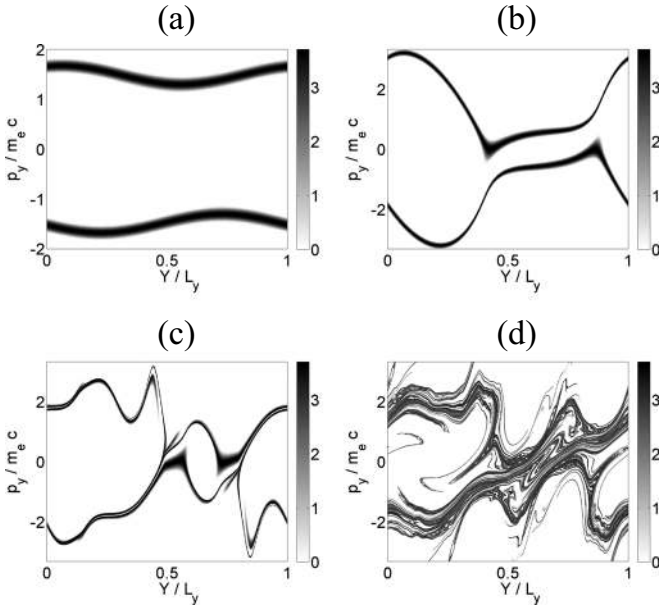

FIG. 25. Ten-logarithmic electron phase space distributions computed by the 1D simulation of the two-stream instability at the times $\omega_p t=63$ (a), 74 (b), 83 (c), and 133 (d). (enhanced online). [URL: http://dx.doi.org/10.1063/1.3514586.1]

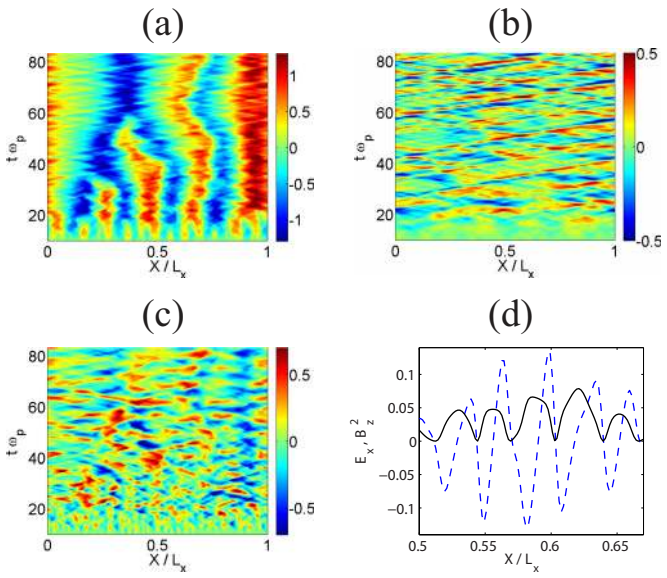

FIG. 26. (Color online) The fields normalized with $s_0=e/m_e c\omega_p$ computed by the 1D simulation: (a) shows $s_0 B_z$, (b) shows $s_0 E_y$ and (c) $s_0 E_x$. The normalized magnetic pressure $\propto B_z^2$ (solid black curve) is compared to $s_0 E_x$ at the time $\omega_p t=11$ in (d). The filaments merging process are clearly evidenced in (a).

The electron phase space distribution has changed qualitatively at $\omega_p t=74$, when the large primary phase space hole is about to form in the interval $0.85<y/L_y<0.4$ (periodic wrap-around) and a separate structure fills the remainder of the simulation box. If the beam speeds were nonrelativistic, and if we would have a periodic train of phase space holes, then the structure in the interval $0.4<y/L_y<0.85$ would become the x-point of the separatrix between the parts of the phase space corresponding to untrapped and trapped electrons. Here the substantial relativistic electron mass variations change the shape of the separatrix and, instead of an x-point, a secondary phase space hole has formed at $\omega_p t=83$ in the interval $0.5<y/L_y<0.8$. The primary electron phase space hole reveals in Fig. 25(c) large-amplitude perturbations of its boundary. It is not a stationary phase space hole, which explains the electric field oscillations in Fig. 24. Its oscillatory electric fields cause the rotation and the compression of the secondary phase space hole in the time-animation of Fig. 25. The electrons have filled up a significant part of phase space at $\omega_p t=133$. However, the primary and secondary phase space holes have not yet merged. The enhanced stability of relativistic electron phase space holes against the coalescence instability compared to their nonrelativistic counterparts in a one-dimensional system has been demonstrated by parametric PIC simulation studies.[192]

Case Study 2. We consider now the filamentation instability in its most basic form. The simulation box of length L_x is oriented along x and orthogonally to the beam flow direction y. Figure 26 shows the spatiotemporal distribution of the B_z, of the E_y that is driven by the displacement current, and of the electrostatic E_x.

It also compares E_x with the magnetic pressure B_z^2 at an early time $\omega_p t=11$. The distribution of B_z evidences an initial growth phase prior to $\omega_p t\sim 15$, in which small filaments of

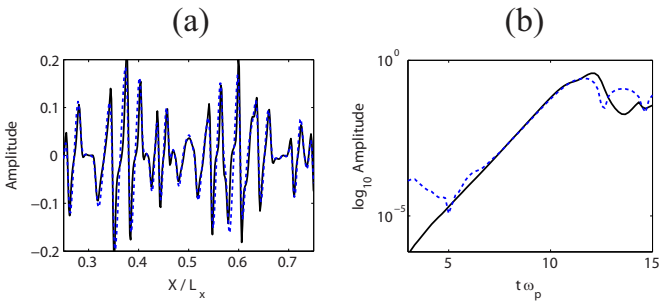

FIG. 27. (Color online) The electrostatic $1.25 \cdot E_x$ (blue dashed curve) is compared in panel (a) to $E_B = -B_z d_x B_z / 8\pi e n_s$ (solid black curve) at $\omega_p t = 11$. In (b), the time-evolution of these amplitudes are compared at the position $X/L_x \sim 0.6$, where both are maximally positive. All curves are expressed in units of $\omega_p m_e c/e$.

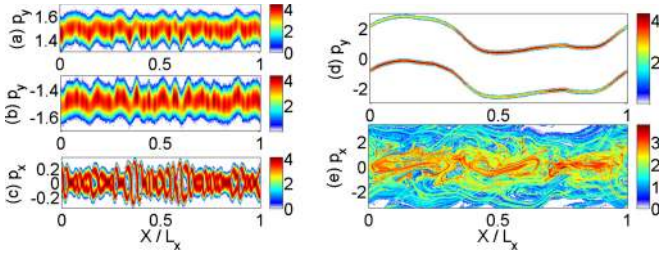

FIG. 28. (Color online) The ten-logarithmic electron phase space distributions. The distributions for the momentum component along the beam direction are shown in (a) and (b) at the time $t\omega_p = 10.8$, while (c) displays the total distribution for the momentum component along the simulation direction. The total distribution for the momentum component along the beam (d) and in the simulation direction are shown in (e) at $\omega_p t = 83$. (enhanced online). [URL: http://dx.doi.org/10.1063/1.3514586.2]

width $\sim L_x/20$ grow. Figure 23 shows that the exponential growth phase of B_F ends at this time. Its value continues to increase, but not exponentially. A different growth mechanism must be at work.

Figure 26(a) reveals that this further increase of B_F is linked to the merging of filaments after the initial quasiequilibrium has been established. The flow-aligned E_y or the electrostatic E_x in Figs. 26(b) and 26(c) do not show a clear correlation with B_z at late times. The rapid growth of the filamentation instability implies that, although the wave growth is aperiodic, the filamentation mode can couple to high-frequency modes in the plasma. The strong B_z supports the extraordinary modes in a plasma, to which E_y can couple, while the E_x can couple to the upper-hybrid wave branch.[193] However, the linear dispersion relation of these waves will be modified by the oscillations of B_z and of the plasma frequency.

The electrostatic waves are at least partially pumped by the magnetic pressure gradient force, as it can be seen at an early simulation time in Fig. 26(d), when the electrostatic field does not yet couple to the eigenmodes of the plasma. The electric field vanishes, whenever $B_z = 0$ or $dB_z/dx = 0$, or, consequently, when $B_z dB_z/dx = 0$. This provides a first hint of the connection between E_x and the magnetic pressure gradient force.

Figure 27(a) compares $E_B = -B_z d_x B_z / 8\pi e n_s$ with E_x, where n_s is the unperturbed density of one electron beam. The match would be accurate for nonrelativistic beam speeds.[184] We have multiplied here E_x by an empirically determined proportionality factor of 1.25. Both curves agree well at $\omega_p t = 11$, clearly evidencing their connection. This proportionality also holds as a function of time, as it is demonstrated by Fig. 27(b). Initially, the E_x is due to the noise arising from statistical charge density fluctuations in the simulation. In the interval $6 < \omega_p t < 11$, the curve $1.25E_x$ matches E_B at the selected position. After this time, both curves diverge as the turbulent wave spectrum develops in Fig. 26(c).

Figure 28 visualizes the electron phase space distributions at two simulation times. The projection $f_e(x, p_y)$ of the electron phase space distribution shows clusters of electrons. A location with a higher density on one beam corresponds to a density depletion on the other; electrons moving in the same direction attract each other, while those moving into opposite directions repel each other magnetically. The electrostatic E_x field results in the formation of electron phase space holes in the projection $f_e(x, p_x)$ of the electron phase space distribution.

The electron beams are still compact in the projection $f_e(x, p_y)$ at the late time, but the mean momentum along p_y of each beam varies strongly with x and also with time, as the time-animation of Fig. 28 demonstrates, and we can expect relativistic mass variations amounting to several rest masses. The $f_e(x, p_x)$ distribution reveals that electrons have been heated to relativistic temperatures, which introduces a spread in the relativistic electron masses at any position x. This mass variation probably results in the filament merging at late times here and in simulations of relativistically colliding leptonic flows[194] because the saturation condition (magnetic trapping) for the filamentation instability depends on the electron cyclotron frequency [see Eq. (54)]. The latter is here neither uniform in space or time nor uniform for all electrons at any given position. By contrast, 1D PIC simulations, with a value of v_b that do not introduce notable relativistic mass variations, evidence a steady state distribution of the filaments after the saturation.

Case Study 3. We illustrate now the consequence of resolving a second spatial dimension. We consider first a beam velocity vector parallel to y in the simulation's $x-y$ plane, which combines case studies 1 and 2. The selection of beam parameters favors the growth of the filamentation instability over the two-stream mode and the oblique modes because of first a larger exponential growth rate and, second, because of the delayed growth of the two-stream instability (Fig. 23).

Figure 29 plots the time-evolution of the box-averaged energy density of the magnetic B_z component and of the total electric field energy density, which are both normalized to the total initial kinetic energy density of the electrons. It also displays the spatial distribution of the relevant field components at the time $\omega_p t = 22$, when the magnetic field energy density reaches its maximum in this 2D simulation. The magnetic energy density does not show the smooth exponential growth as in the 1D simulation of the filamentation instability, where a uniformity along y was enforced by the simulation geometry that resolved only x. So we expect that

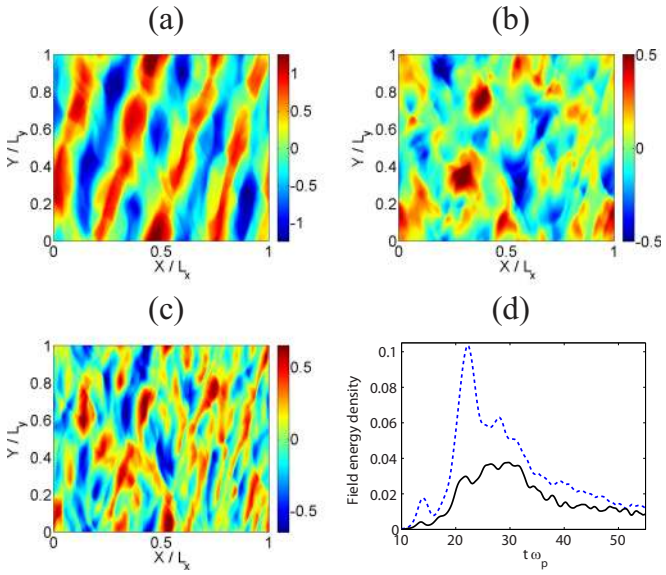

FIG. 29. (Color online) The electromagnetic fields at $\omega_p t=22$ in the 2D simulation, which resolves the $x-y$ plane, and has the beam direction aligned with y: The distributions [(a)–(c)] display B_z, E_y, and E_x, normalized to $\omega_p m_e c/e$. The normalized field energies of B_z (dashed blue curve) and of $\mathbf{E}$ are plotted in (d) in units of the initial electron kinetic energy density. (enhanced online). [URL: http://dx.doi.org/10.1063/1.3514586.3]

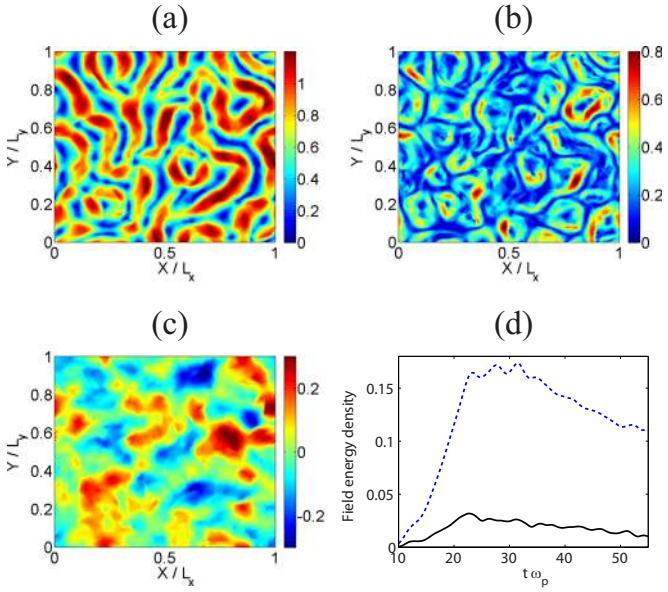

FIG. 30. (Color online) The electromagnetic fields at $t\omega_p=22$ in the 2D simulation, which resolves the $x-y$ plane, and has the beam direction aligned with z: The distributions [(a)–(c)] display $|B_x+iB_y|$, $|E_x+iE_y|$, and E_z, normalized to $\omega_p m_e c/e$. The box-averaged field energy densities $\mathbf{B}^2$ (dashed blue curve) and $\mathbf{E}^2$ are plotted in (d) in units of the initial electron kinetic energy density. (enhanced online). [URL: http://dx.doi.org/10.1063/1.3514586.4]

the magnetic field distribution is not uniform along y. The magnetic energy density exceeds the electric one by a factor of 3 at $\omega_p t\sim 22$, but both converge to similar and much lower values at late simulation times. We observe a strong magnetic field only during a limited time interval.

The distribution of B_z in Fig. 29(a) reveals a two-dimensional structuring. The magnetic field stripes are neither perfectly planar nor aligned with y. Wave modes with $k_y\neq 0$ must be present. The oscillation period of B_z along y is L_y, which equals that of the two-stream mode. However, we find this modulation only in B_z, while the E_y component in Fig. 29(b), which is associated with the two-stream instability, does not show such oscillations. The spectrum of B_z in the k_x,k_y plane (not shown) reveals that these modes still belong to the filamentation mode branch. This is in line with the solution of the linear dispersion relation in Fig. 14(a), which predicts the wave growth for small $k_y\neq 0$. These modes were excluded geometrically in case study 2.

The uniform oblique angle is a finite box effect. The periodic boundary conditions result in a discrete wave spectrum, and here a single dominant mode is responsible for the uniform tilt. The time-animation of Fig. 29 reveals that initially small filaments grow, with approximately the same size as those found in case study 2 prior to $\omega_p t\sim 11$. The magnetic energy density of these small-scale filaments peaks at $\omega_p t\sim 13$, when the magnetic energy density in Fig. 29(d) reaches its first maximum. Thereafter, the magnetic field shows an intermittent phase, during which the small filaments merge in various locations as in case study 2. We can then observe in the time-animation of Fig. 29 the development of larger magnetic stripes. These saturate at $\omega_p t\sim 22$ and are responsible for the absolute maximum in the magnetic energy density. The magnetic field becomes diffuse after $\omega_p t>22$, as the time-animation of Fig. 29 evidences. The distribution of B_z continues to show a preferential direction though. Magnetic stripes with a positive or negative amplitude follow the beam (y) direction.

The time-animation of Fig. 29 shows a clear connection of B_z, E_x, and E_y prior to $\omega_p t\sim 13$, while no such correlation is visible after this time. The average size of the structures in E_x in Fig. 29 is much smaller than that of those in E_y at $\omega_p t\sim 22$, suggesting different source mechanisms and wave modes that are responsible for these fields at late times.

The nonplanarity of B_z and of its generating currents after $\omega_p t\sim 13$ imply that we cannot necessarily connect the turbulent wave fields of E_y to the displacement current and of E_x to the magnetic pressure gradient force. At this advanced simulation time, both sources will also have coupled significant energy into the plasma eigenmodes, which would complicate further a straightforward interpretation of the data. What is, however, clear is that the two-stream instability has not developed, since we do not find a modulation of E_y along y at this time and later, which could be approximated by a sine wave with period L_y. The rapid decrease of the field energy densities in Fig. 29(d) furthermore demonstrates that the plasma has thermalized at the simulation's end and the two-stream instability cannot develop anymore. This case study 3 confirms our previous hypothesis based on the linear growth rate that the filamentation instability is the dominant one for symmetric counterstreaming electron beams with $\gamma_b=\sqrt{3}$.

Case Study 4. Now we let the electron beams move orthogonally to the $x-y$ simulation plane to study the interplay of the filaments. Figure 30 displays the box-averaged energy densities of the electric field $\propto\mathbf{E}^2$, as in Fig. 29. It also displays the box-averaged energy density of the trans-

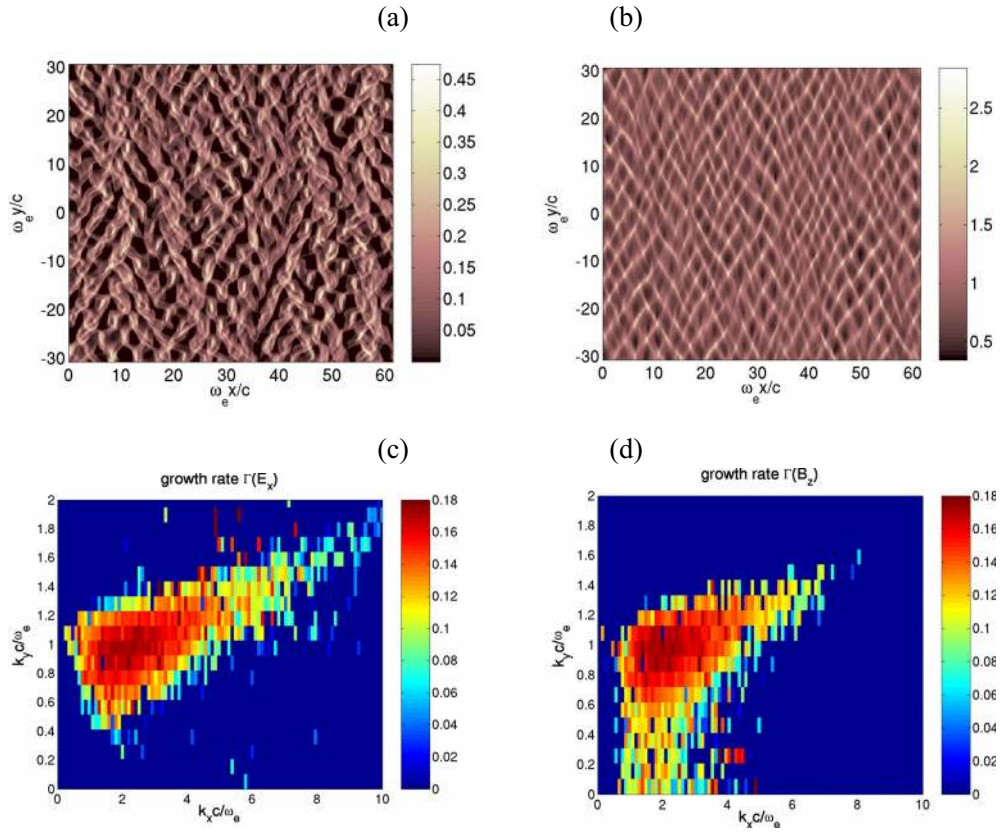

FIG. 31. (Color online) 2D PIC simulation of a waterbag beam-plasma system with $n_b/n_p=0.1$, $\gamma_b=4$, $P_{b\|}=P_{b\perp}=0.2$, $P_{p\|}=P_{p\perp}=0.1$: (a) beam and (b) plasma density profiles at the end of the linear phase; simulated growth rate maps calculated from (c) $E_x(\mathbf{k})$ and (d) $B_z(\mathbf{k})$ spectra over $30\leq\omega_e t\leq 40$. The beam flows along the y-axis.

verse magnetic field $\propto(B_x^2+B_y^2)$, which grows in response to the
filamentation instability. The transverse magnetic field $B_\perp=|B_x+iB_y|$ is compared to the transverse electric field $E_\perp=|E_x+iE_y|$ and the beam-aligned E_z.

The comparison of the electric field energy density $\propto\mathbf{E}^2$ in Figs. 29(d) and 30(d) demonstrates that both grow to about the same peak value $\sim$0.04 at $\omega_e t\sim 22$. This is a further evidence for an absence of the two-stream instability in case study 3, as it is excluded geometrically in case study 4. The magnetic energy densities in case studies 3 and 4 differ. Only B_z grows in case study 3, while B_x and B_y grow in case study 4. The magnetic energy density $\propto(B_x^2+B_y^2)$ in Fig. 30(d) peaks at a value of $\sim$0.16, which is approximately twice that of the magnetic energy density $\propto B_z^2$ in case study 3. This suggests that each magnetic degree of freedom reaches about the same energy density.

Furthermore, we note that the magnetic energy density in Fig. 30(d) maintains a high value, which makes it comparable to that in the 1D case study 2. The rapid decrease of the magnetic energy density in Fig. 29(d) should thus be linked to the nonuniform distributions along the beam flow direction y that accelerates the plasma thermalization. The transverse magnetic and electric fields in Figs. 30(a) and 30(b) show the well-known banded structure, which is characteristic for a filamentation instability driven by counterstreaming symmetric electron beams.[92] The magnetic bands are separating the individual current filaments and they change continuously their shape, as evidenced in the time-animation of Fig. 30. This time-animation reveals on various occasions, in particular, at late times, x-points in $|B_\perp|$, which occur when the filaments merge in 2D. The time-animation further demonstrates that the filament size becomes through the mergers comparable to the box size at $\omega_p t\sim 50$ and we stop the simulation here.

We now turn away from these idealized case studies, in which the filamentation instability did outgrow all other instabilities, and in which we could isolate individual nonlinear structures driven by relativistic electron beams. We consider now a more realistic setting, in which wave modes with different polarizations on different wave branches compete and interact simultaneously with the electrons.

B. Large-scale simulations: Validation of the linear theory and related effects

Accurate comparisons between linear and simulation results during the early phase of beam-plasma instabilities have been carried out in Refs. 19–22. For illustrative purposes, let us first consider the waterbag configuration yielding the theoretical growth rate map of Fig. 10. This system was simulated by means of the parallel CALDER code with the same parameters as linear theory.[19] Periodic boundary conditions are applied for both fields and particles while ions are kept immobile. Fields are found to develop rapidly up to $\omega_e t=60$, at which time the beam density profile undergoes

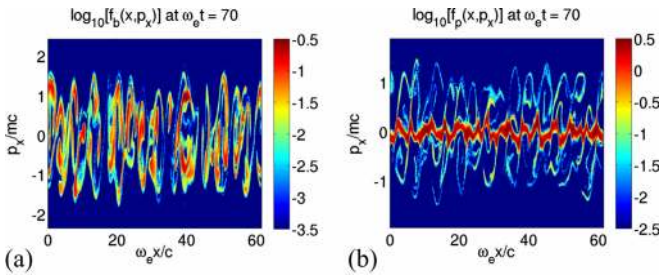

FIG. 32. (Color online) (x,p_x) phase spaces of (a) beam and (b) plasma electrons close to the field saturation time. The parameters are those of Fig. 31.

strong oblique modulations ($\delta n_b/n_b \sim 5$), as displayed in Fig. 31(a). These modulations translate in the (x,p_x) phase space into vortex structures indicative of complete trapping along the oblique dominant wave direction [Fig. 32(a)]. Trapping therefore proves to be the main mechanism causing the field saturation. According to past numerical studies of 1D beam-plasma instabilities,[93,168] this is an expected result given the hydrodynamical character of the instability in the present case ($\mathbf{k}\cdot\Delta\mathbf{v} \sim 0.1 < \delta \sim 0.18$). The time history of the normalized (to the initial beam energy) particle kinetic energies plotted in Fig. 33(a) shows at the saturation time ($\omega_e t \sim 90$), the beam has lost about 30% of its initial energy. This is 50% higher than the theoretical estimate of Ref. 175.

The rather slow wave phase velocity of the dominant oblique modes ($\omega/k=0.34$, as compared to $\omega/k=0.91$ for the fastest-growing parallel mode) results in an efficient coupling with the plasma electrons, hence exhibiting pronounced density modulations $\delta n_p/n_p \sim 3$ [Fig. 31(b)]. This efficient interaction with plasma electrons gives rise to the partially trapped structures observed in the (x,p_x) phase space of Fig. 32(b), as well as to the quasi-instantaneous beam-to-plasma energy transfer seen in Fig. 33(a). This feature constitutes a major difference with the usual 1D picture of the relativistic beam-plasma interaction wherein, in the hydrodynamical regime, the plasma response can be assumed linear.[26,168,175]

A close comparison between linear theory and simulation is provided by Figs. 31(c) and 31(d) which plots the **k**-resolved growth rates extracted from the exponential evolution of the $E_x(\mathbf{k})$ and $B_z(\mathbf{k})$ spectra over the time interval

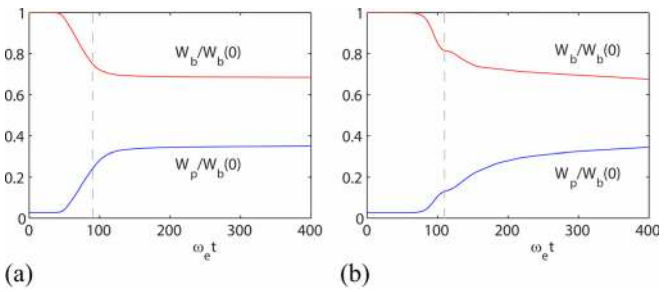

FIG. 33. (Color online) Time histories of beam (red) and plasma (blue) kinetic energies for (a) $P_{b\|}=P_{b\perp}=0.2$ (a) and $P_{b\|}=P_{b\perp}=1$ (b). The other parameters are $n_b/n_p=0.1$, $\gamma_b=4$, $P_{p\|}=P_{p\perp}=0.1$. All energies are normalized to the initial beam energy. The gray dashed line indicates the saturation time of the fields following the linear phase.

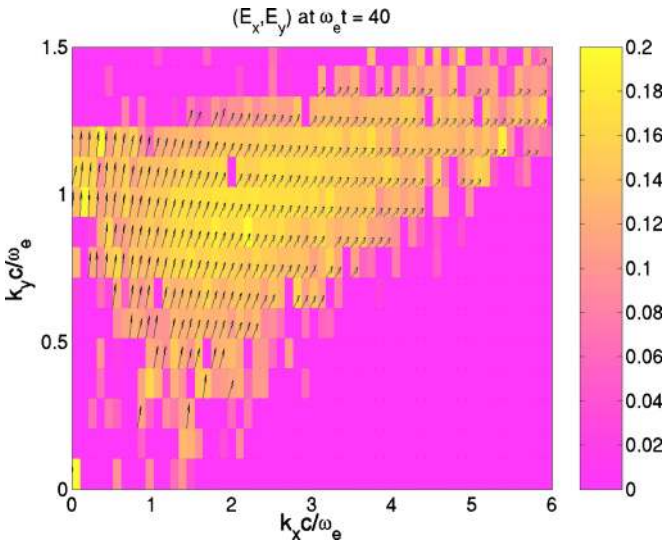

FIG. 34. (Color online) Vector field representation of the simulated electric fluctuations at $\omega_e t=40$. The parameters are those of Fig. 31. The color code refers to the simulated growth rate.

$30 \leq \omega_e t \leq 40$. The main features of Fig. 10(a) are quantitatively reproduced. Note that, because of their relatively weak E_x content, the growth of the filamentation modes can only be accurately accessed through the B_z spectrum. The essentially electrostatic nature of the dominant oblique modes is demonstrated by plotting in Fig. 34 the electric field orientation of the simulated electric fields during the linear phase. We observe that the simulation result closely agrees with the prediction of Fig. 10(b).

The effect of increasing the beam thermal spread to $P_{b\|}=P_{b\perp}=1$ is illustrated by Figs. 35(a) and 35(b) which displays the numerically extracted growth rate maps. The map obtained from $E_y(\mathbf{k})$ accurately matches that of Fig. 11. The displacement of the dominant mode toward the parallel axis is well reproduced. However, the agreement is not that good as regards the evolution of the filamentation modes expected to be wholly suppressed in the present configuration. Even though the magnetic field energy is found to be lower than the electric energy by about two orders of magnitude, it is seen to grow at a comparable rate as evidenced in Fig. 35(b). This stems from the rapid smoothening of the initial waterbag-shaped distribution during the development of the dominant electrostatic modes. There results a distribution function slightly differing from the waterbag form for which the theoretical predictions no longer exactly apply. The anomalous resistivity generated by the resulting high-frequency electric fluctuations has also been invoked as an additional mechanism for the enhancement of filamentation modes.[61,159] Complete suppression of the filamentation instability therefore appears difficult to achieve in the parameter range under consideration, as also further discussed in Ref. 23. Furthermore, one should pay attention to the fact that, because of an increased wave phase velocity ($\omega/k \sim 0.6$) as compared to the previous case, the initially dominant electrostatic waves interact much less efficiently with the plasma electrons. Consequently, only the beam electrons are subject to electrostatic trapping [Fig. 36(a)], while the plasma elec-

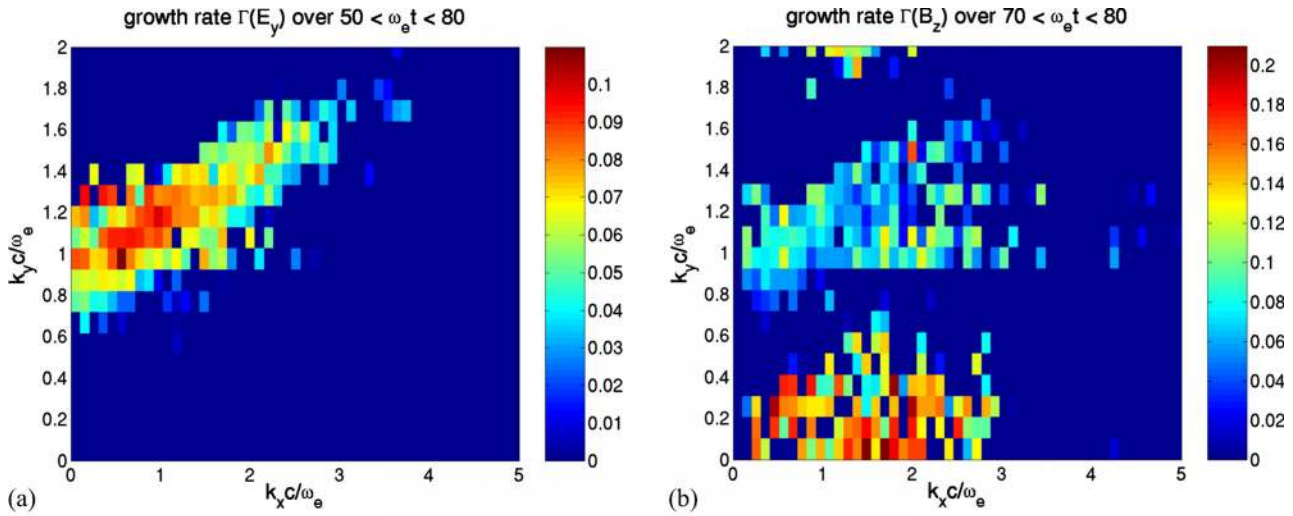

FIG. 35. (Color online) 2D PIC simulation of a waterbag beam-plasma system with $n_b/n_p=0.1$, $\gamma_b=4$, $P_{b\|}=P_{b\perp}=1$, $P_{p\|}=P_{p\perp}=0.1$: simulated growth rate maps calculated from E_y (a) and B_z spectra (b) over $50\leq\omega_e t\leq 80$ and $70\leq\omega_e t\leq 80$, respectively. The beam drift is along the y-axis.

trons exhibit anharmonic, yet untrapped, motion [Fig. 36(b)]. As a result, at field saturation, the beam energy loss is equally converted into plasma heating and field energy [Fig. 33(b)]. The total electron distribution function remaining double-peaked, beam slowing down and plasma heating proceeds, yet at a much reduced quasi-linear rate.[115,195] The observed instantaneous energy transfer between both populations suggests the occurrence of nonlinear Landau damping, whose matching condition $\omega-\omega'\sim(\mathbf{k}-\mathbf{k}')\cdot\mathbf{v}$, where $(\omega,\mathbf{k})$ and $(\omega',\mathbf{k}')$ denote two unstable waves, is easily fulfilled in 2D geometry.[175]

2D PIC simulations have also been used to support the hierarchy map of Fig. 20 within the Maxwell–Jüttner model.[18] In Figs. 37(a) and 37(b) are plotted the beam and plasma profiles obtained around the end of the linear phase for $n_b/n_p=1$, $\gamma_b=3$, $T_b=1000$ keV, and $T_p=5$ keV. As expected, the filamentation instability prevails, thus yielding mostly transverse modulations (that stand out more clearly on the plasma profile due to its weaker temperature). As a result, the magnetic energy is found to prevail over the electric energy, despite a significant contribution of the E_x field to the charge separation induced by nonequal electron temperatures. Varying the beam drift energy and temperature to $\gamma_b=1.5$ and $T_b=2000$ keV causes the system evolution to be governed by oblique modes [Figs. 37(c) and 37(d)]. By contrast, changing to a colder and more diluted beam with $n_b/n_p=0.1$ and $T_b=500$ keV leads to a two-stream-dominated system [Figs. 37(e) and 37(f)].

A noticeable, if somewhat academic, feature of the Maxwell–Jüttner hierarchy map is that the surface boundaries almost make contact for $n_b/n_p=1$, $\gamma_b=1.1$, and $T_b=100$ keV (see Fig. 20). It has been found[110] that the spectrum associated with this set of parameters is characterized by an almost isotropic (in $\mathbf{k}$-space) continuum of unstable modes growing at approximately the same rate $\delta\sim 0.1$. Figures 38(a) and 38(b) shows that both the beam and plasma density profiles are strongly modulated at the end of the linear phase without exhibiting a clearly defined pattern. The growth rate maps numerically extracted from the $E_y(\mathbf{k})$ and $B_z(\mathbf{k})$ spectra indeed reveal a very broad unstable spectrum encompassing both instability classes. It is worth mentioning that even although the magnetic field energy ends up exceeding by more than an order of magnitude the electric energy at later times $(100\leq\omega_e t\leq 400)$, no coherent structure is then seen to form.

C. Comparisons between 1D and 2D simulations in the oblique regime

Assuming the initial broadband unstable spectrum gets sufficiently narrowed at the outcome of the linear stage, one may think that the beam-plasma dynamics in the oblique regime can be captured in a good approximation by means of a 1D PIC simulation whose spatial axis is parallel to the dominant oblique mode. In fact, such a reduced numerical description does not manage to accurately predict the beam slowing down obtained through a 2D simulation. This failure is illustrated here with the waterbag beam-plasma parameters of Fig. 31. For these parameters, the initially dominant mode propagates at an angle $\theta=65°$ with respect to the beam direction. Plotted in Fig. 39 are the temporal evolutions of the beam (a) and electric (b) energies as predicted by three 1D PIC simulations whose spatial axis makes a varying angle ($\theta=0°$, 55°, and 65°) with the beam axis. As expected, the

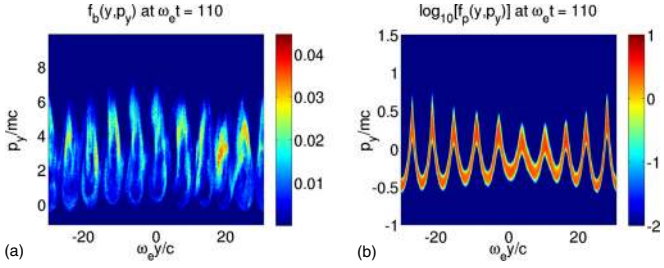

FIG. 36. (Color online) (x,p_x) phase spaces of (a) beam and (b) plasma electrons at the field saturation time. The parameters are those of Fig. 35.

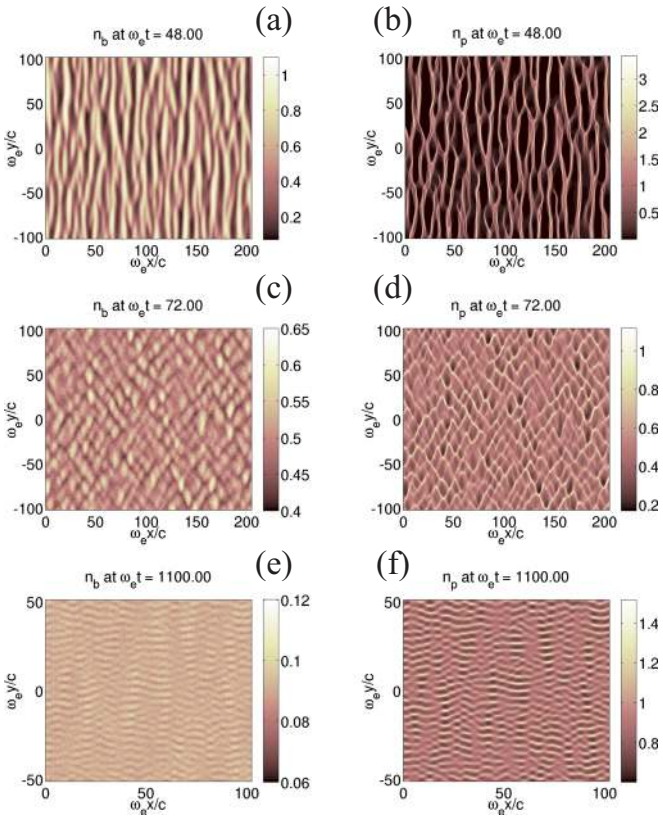

FIG. 37. (Color online) 2D PIC simulations of Maxwell–Jüttner beam-plasma systems: beam [(a), (c), and (e)] and plasma [(b), (d), and (f)] density profiles at the end of the linear phase with [(a) and (b)] $n_b/n_p=1$, $\gamma_b=3$, $T_b=1000$ keV, [(c) and (d)] $n_b/n_p=1$, $\gamma_b=1.5$, $T_b=2000$ keV, [(e) and (f)] $n_b/n_p=0.1$, $\gamma_b=1.5$, $T_b=500$ keV. In all cases, $T_p=5$ keV and the beam flows along the y-axis.

$\theta=0°$ case (restricted to weaker two-stream modes) leads to a field growth slower than that predicted when resolving the most unstable direction. However, the field energy keeps an approximately constant value after reaching saturation. This strongly contrasts with the rapid drop of the postsaturation electric energy observed in the large-angle 1D simulations, in fair agreement with the 2D case. This decrease points to the instability in the oblique geometry of the trapping structures generated at the end of the growth stage. Despite these differences, all 1D simulations predict close values ($\sim$7–10%) of the late-time energy loss, which significantly underestimate the 2D value ($\sim$30%). This discrepancy stems from the failure of the 1D simulations to account for the time-varying direction of the dominant mode. Consequently, the largest reservoir of unstable modes available in a 2D geometry yields an increased beam slowing down along with a longer-duration phase of field growth, as evidenced in Fig. 39(b).

D. Dynamic transition between distinct regimes of instability

As already hinted at in Sec. V B, a general result of multidimensional simulations of diluted-beam-plasma systems initially governed by quasielectrostatic (oblique or parallel) modes is the late-time domination of filamentation. This takes place through a multiple-stage process as illustrated here by a 3D simulation. A Maxwell–Jüttner configuration is considered with $n_b/n_p=0.1$, $\gamma_b=3$, $T_b=50$ keV, and $T_p=5$ keV. The numerical box consists of 360^3 cells with $\Delta x=\Delta y=\Delta z=0.15c/\omega_e$. In contrast to previous cases, ion motion is here accounted for with a realistic mass ratio $m_i/m_e=1836$, but it does not affect the system evolution up to the final simulation time $\omega_e t=600$.

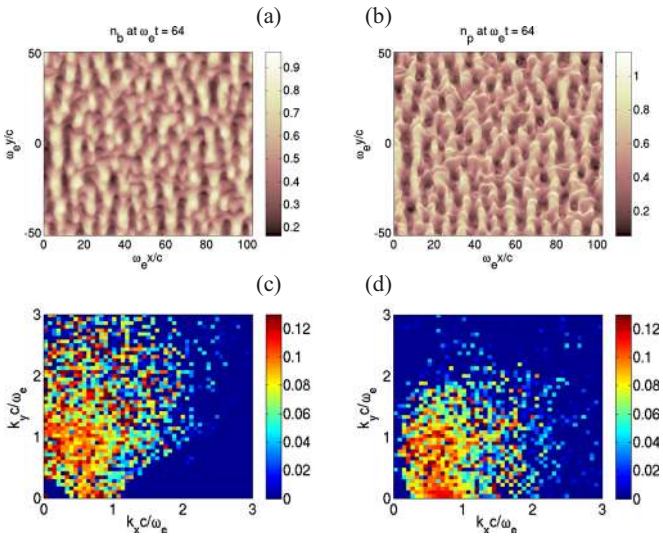

FIG. 38. (Color online) 2D PIC simulations of a Maxwell–Jüttner beam-plasma system with $n_b/n_p=1$, $\gamma_b=1.1$, $T_b=100$ keV, and $T_p=5$ keV: (a) beam and (b) plasma density profiles; growth rate maps obtained from (c) $E_y(\mathbf{k})$ and (d) $B_z(\mathbf{k})$ spectra.

Isosurfaces of the beam and plasma density profiles are displayed in Fig. 40 at various times. At $\omega_e t=80$, oblique modulations clearly stand out in both profiles, in agreement with the theoretical prediction that the system is initially dominated by oblique modes characterized by $\delta_{\max}/\omega_e=0.07\omega_e$ at $(k_\parallel,k_\perp)=(1,0.75)\omega_e/c$ [Fig. 41(a)]. The initially prevailing oblique modes get rapidly stabilized by the heating and slowing down of the beam, thus allowing purely parallel modes to take the lead in the field growth. This results in the flow-aligned modulations affecting the beam and plasma profiles at $\omega_e t=160$. This transition can be readily understood from linear theory using the real-time electron distribution. Beam electrons can be fitted by a Maxwell–Jüttner distribution with $\gamma_b=1.6$ and $T_b=200$ keV, whereas the plasma distribution remains essentially unchanged. For

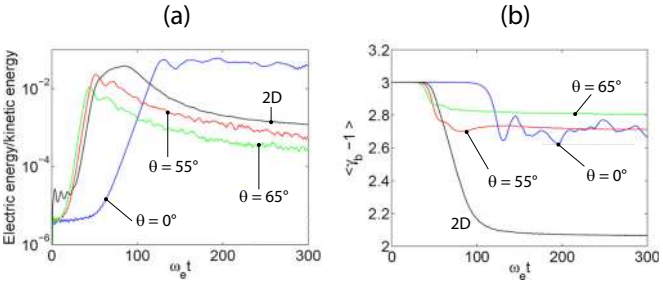

FIG. 39. (Color online) Comparison between 1D and 2D simulations in the oblique regime: time evolutions of the normalized electric energy (a) and kinetic beam energy (b). The spatial axis resolved in the 1D simulations makes a varying angle (from 0° to 65°) with the beam axis.

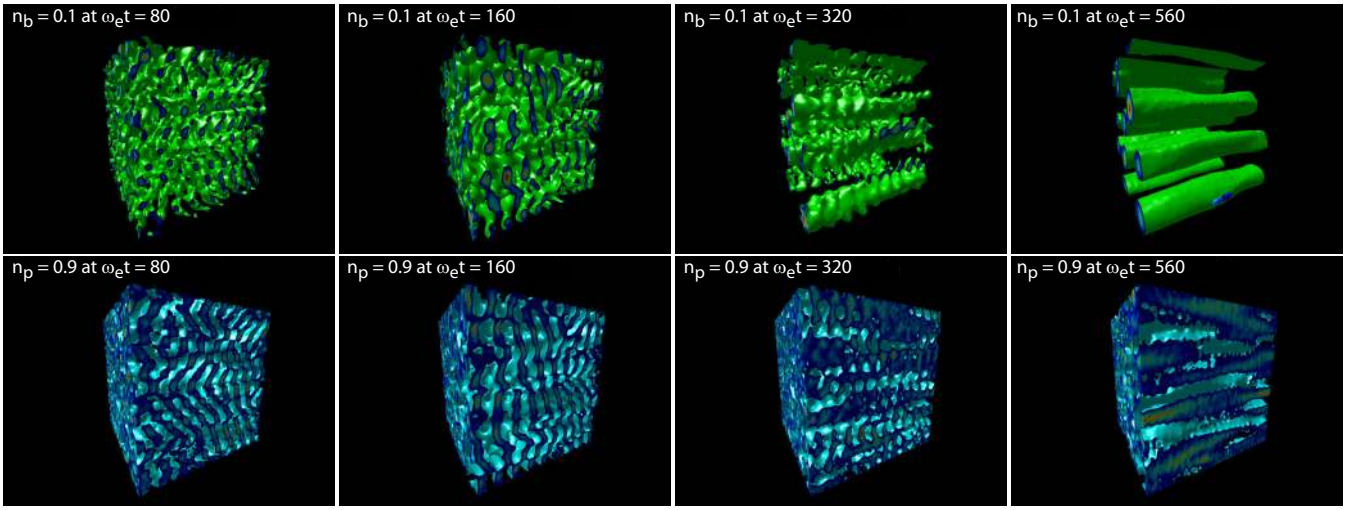

FIG. 40. (Color online) 3D PIC simulation of a Maxwell–Jüttner beam-plasma system with $n_b/n_p=0.1$, $\gamma_b=3$, $T_b=50$ keV, $T_p=5$ keV, and $m_i/m_e=1836$: isosurfaces of the beam (upper plots) and plasma (lower plots) density profiles at successive times. The beam flows rightward.

these parameters, the hierarchy map depicted in Fig. 20 predicts the system has indeed shifted to the two-stream regime. The corresponding growth rate map shows a reduced peak growth rate $\delta_{\max}/\omega_e=0.016$ reached $k_\parallel=1.3$ [Fig. 41(b)]. We find that the beam experiences its highest deceleration rate during the oblique-to-parallel transition phase, losing about 20% of its initial energy over the time interval $80\leq\omega_e t\leq 160$.

Stabilization of the parallel modes subsequently occurs through further spreading of the beam and plasma distributions until a single-peaked distribution is formed. Because of its strong enough anisotropy, the resulting beam-plasma distribution remains unstable against filamentation modes, whose development is depicted in Fig. 40 at $\omega_e t=320$ and $\omega_e t=560$. Note, in particular, how remaining parallel modulations are smoothened out during this time interval. There results a typical filamentary configuration consisting of microcurrents of beam electrons (of radial extent $\sim 10c/\omega_e$) surrounded by counterflowing plasma electrons (Fig. 42). A this stage, though, the beam-plasma distribution function proves too severely distorted to be accurately fitted by Maxwell–Jüttner functions. The magnetic energy is seen to grow exponentially over $200\leq\omega_e t\leq 600$ (with $B_\perp^2\gg B_\parallel^2$) at the effective rate $\delta/\omega_e\sim 0.005$. By the end of the simulation, the beam loss, which amounts to ~30% of its initial energy, has been entirely transferred to plasma electrons.

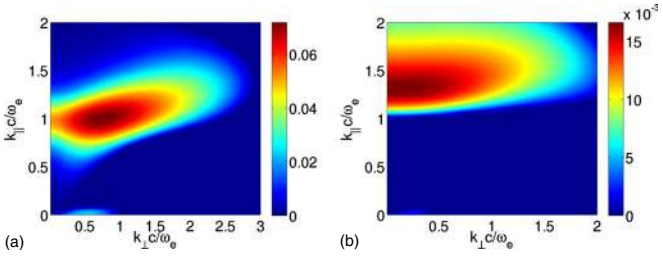

FIG. 41. (Color online) (a) Theoretical growth rate map with the parameters of Fig. 40. (b) Growth rate map for the parameters best fitting the simulated beam-plasma at $\omega_e t=160$: $n_b/n_p=0.1$, $\gamma_b=1.6$, $T_b=200$ keV, and $T_p=5$ keV.

VI. BEYOND THE BASIC ELECTRON BEAM-PLASMA SYSTEM

Many extensions of the aforementioned results have been published over the past decades. The basic system we have been describing, namely, two relativistic counterstreaming electron beams, can be enriched in many ways. On the one hand, extra physical ingredients can be added such as finite mass ions, collisions, background magnetic field, quantum effects, etc. On the other hand, one can modify the system itself by varying the number and nature of the interacting species. For instance, proton beam-plasma instabilities may be relevant for the proton-driven FIS[196,197] as well as some astrophysical settings. Collisions of counterstreaming e-i or pair (e^-e^+) plasmas are also under scrutiny for their potential role in GRBs. Since the present model can be end-

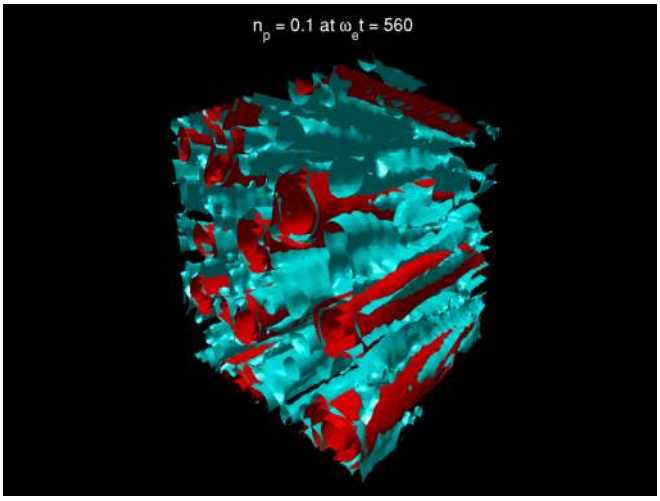

FIG. 42. (Color online) Superimposed iso-surfaces of beam (red) and plasma (blue) density profiles at $\omega_e t=560$.

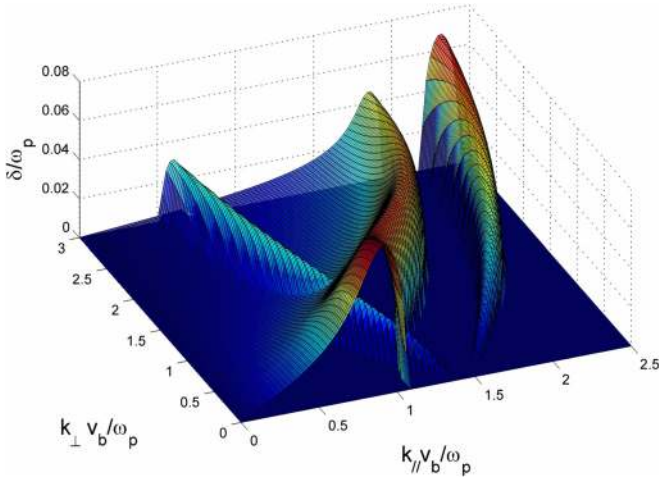

FIG. 43. (Color online) Growth rate map (ω_p units) of the electron beam-plasma system with a guiding magnetic field. Parameters are $\alpha=0.1$, $\Omega_B=2$, and $\gamma_b=4$. Filamentation is stabilized, and some wave vectors support more than one unstable mode. Ions are fixed. The flow is along the y axis.

lessly refined, we shall restrict the present section to an overview of its most investigated and/or worthwhile extensions.

A. Same system, additional effects

Moving ions, collisions, or an external magnetic field may add unstable modes which were not excited before. Mathematically speaking, new branches of the dispersion equation can appear, which may or not overlap in the **k**-space. If they do, the full dispersion equation will have more than one complex root $\omega+i\delta$ with $\delta>0$ for a given wave vector.

A guiding magnetic field was the first additional ingredient considered to potentially affect the multidimensional unstable spectra of REB systems.[133] Calculations were performed within the cold-limit, where an analytical treatment of the magnetic field remains tractable. Here, the strength of magnetization is measured through the parameter $\Omega_B=\omega_c/\omega_p$, where $\omega_c=|q|B_0/m_ec$ is the nonrelativistic electronic cyclotron frequency. A salient feature of the magnetized system is the suppression of the filamentation instability. For a diluted beam, the threshold is $\Omega_B>\beta_b\sqrt{\alpha\gamma_b}$ (this result has been extended to arbitrary beam densities in Ref. 164). Dividing the inequality by γ_b yields a very intuitive relation for the suppression of filamentation instability,

$$\frac{qB_0}{\gamma_b m_e c} > \omega_p \beta_b \sqrt{\frac{\alpha}{\gamma_b}}, \tag{58}$$

as one recognizes on the right-hand side the growth rate of the unmagnetized filamentation instability reported on Table I. The equation above simply states that when the relativistic cyclotron frequency becomes larger than the filamentation growth rate, the electron dynamics is dictated by the external magnetic field rather than by the instability-driven magnetic perturbations. This prediction has since then been confirmed by PIC simulations.[198] Figure 43 shows a filamentation stabilized spectrum. The two-stream profile remains unchanged (because $\mathbf{B}_0\|\mathbf{v}_b$), but the rest of the two-stream/filamentation branch is deeply affected. More unstable branches appear and intersect, yielding portions of the spectrum where the same wave vector supports various unstable modes. Some warm fluid models have been implemented in the magnetized regime,[98,164] and Timofeev *et al.*[165] worked out the full-spectrum kinetic calculation, considering a cold plasma and a monoenergetic beam distribution function of the form $f^0(\mathbf{p}) \propto \delta(p-P_b)e^{-\theta^2/\Delta\theta^2}$, where $\Delta\theta$ defines the angular spread. This first step toward the completion of Clemmow and Dougherty's "daunting task" unraveled a spectrum much richer than the one coming out of a simpler fluid approach. The adjunction of a non-flow-aligned magnetic has also been investigated in the cold-limit,[199] mainly in connection with astrophysics.[200]

Accounting for the ion motion may be mandatory in very weakly unstable cases, or when relativistic effects make the beam electrons' inertia comparable to that of the ions. If the beam is diluted enough, the electron return current remains nonrelativistic. Relativistic effects then result in an "heavy" electron beam interacting with background ions and a "light" electronic return-current. Still in the cold regime, it has been found that the ion motion in the linear phase cannot be neglected for $\gamma_b>\alpha Zm_i/m_e$, where Z and m_i are the ion charge and mass, respectively.[201] It turns out that a finite ion mass triggers unstable Buneman modes arising from the ion/return current interaction.[7,202,203] Note that this criterion applies to the full spectrum and may differ if restricted to parallel or transverse wave vectors. Regarding the latter case, Fiore *et al.*[61] found that ion motion renders filamentation more robust to thermal effects. This conclusion is relevant to relativistic collisionless shocks which are believed to be mediated through the filamentation instability.[82]

Lately, much attention has been paid to quantum effects. Quantum kinetic linear,[204,205] nonlinear,[206] or fluid linear[207] treatments of the "pure" Weibel instability are available, showing a new purely quantum branch and a general weakening (if not suppression) of the instability. Similar development can be found for the two-stream instability,[208] and a purely quantum branch arising from the theory has indeed been found connected with the classical one when extending the calculations to the full 2D unstable spectrum.[209] The quantum fluid equations,[210–212] where quantum correction terms are added to the right-hand side of the nonrelativistic version of Eq. (41), have been instrumental in dealing with the filamentation instability, with[213] or without guiding magnetic field,[214] the two-stream instability in a magnetized plasma,[215] or quantum effects on streaming instabilities in dusty plasmas.[216] Here again, the fluid approach has usually been selected first to deal with magnetic effects. The same fluid approach remains so far the basis for multidimensional investigations of the quantum unstable spectrum.[209,217]

Collisional effects have also inspired many studies, aiming, in particular, to characterize the instabilities possibly excited within the dense precompressed target core in the FIS. Given the then-expected low beam density, it seems legitimate to account for the sole collisionality of the (nonrelativistic) background electrons. Two approaches have been mainly developed so far. The simpler one consists in

adding a Krook collision term $\nu(f^0-f)$ to the right-hand side of Vlasov equation (1) for the collisional species.[57,114,148,218] The fluid counterpart of this technique features a friction term to the right-hand side of Euler equation (41) and has also been implemented by some authors.[156,217] The simplicity of the Krook approach makes it widely employed in spite of its known drawbacks (no relaxation to a Maxwellian, nonconservation of particle number, etc.). More elaborate treatments for the filamentation[219] or the two-stream[220] instabilities rely on a kinetic Fokker–Planck collision operator,[221]

$$\left(\frac{\partial f}{\partial t}\right)_c = \frac{\partial}{\partial \mathbf{v}}\left[-\mathbf{F}(\mathbf{v})f + \frac{1}{2}\frac{\partial}{\partial \mathbf{v}}:(\mathbf{D}(\mathbf{v})f)\right], \tag{59}$$

where $\mathbf{F}(\mathbf{v})$ and $\mathbf{D}(\mathbf{v})$ are friction and diffusion operators in velocity space (see Ref. 99 p. 231, or Ref. 100, p. 315 for more details). Noteworthily, a coherent picture of the effects of collisions has not yet emerged. While some authors find collisions trigger some extra unstable branch(es),[155,217,222] others find they only modify the existing collisionless unstable branch. A general trend, observed regardless of the number of branches, is that collisions tend to generate larger filaments by displacing the fastest growing filamentation modes toward the lower k's. This is in accordance with works on the *resistive* filamentation of a diluted beam in a collisional plasma ruled by Ohm's law, which predict the formation of filaments whose typical width is the *beam* skin depth instead of the plasma one.[60,223]

Finally, some authors focused on cumulative effects on a given part of the unstable spectrum. For example, Molvig[59] and then Cary *et al.*[104] developed a kinetic theory of the collisional (Krook term) filamentation instability in the presence of a guiding magnetic field. They found that the stabilizing effects of magnetic field, collisions, and temperature do add-up, although in a nontrivial way. The full unstable spectrum accounting for ion motion and a guiding magnetic field has been recently computed within the cold-fluid limit, revealing an intricate mode competition.[224]

B. Other relevant beam-plasma systems

Beam-plasma systems involving more than two species are relevant in a number of astrophysical scenarios. For instance, collisionless shocks may arise from colliding pair/pair[225] or e-p/e-p (Ref. 77) plasma shells ("pair" stands for a pair e^+e^- plasma and e-p for electron/proton plasma). The unmagnetized dispersion relation of such a four-stream system has recently been investigated by Michno and Schlickeiser.[226] Filamentation is found to prevail in the relativistic regime, whereas the electrostatic instability rules the nonrelativistic regime. At a later stage, both in GRB or SNR contexts, as the shock propagates and some Fermi-accelerated particles (cosmic rays, CR) interact with the upstream, the very nature of the unstable system may also vary. CRs are usually assumed to be protons.[227] Some authors then have considered a beam of protons neutralized by a cloud of comoving electrons,[228–230] while others superimposed to the CRs a beam of slow protons originating from the upstream.[231] Accounting, in addition, for an external $\mathbf{B}$-field[133] of arbitrary orientation and strength,[199,200] as well as for thermal effects (that may depend on the model distribution functions) multiplies the number of potentially relevant configurations. In this context, much attention was devoted in recent years to a new instability, first pointed out by Bell through a MHD approach.[232] It involves nonresonant Alfvén-like waves destabilized by cosmic rays streaming through a magnetized plasma with mobile ions. The issue at stake here, already mentioned in Sec. I C, is the generation of the magnetic turbulence needed to accelerate particles at the shock. Now, the level of scattering provided by the interstellar medium turbulent magnetic field seems insufficient to account for cosmic rays above a few GeV (see Ref. 229 for more details). In this respect, the now so-called Bell's modes appear as plausible candidates to explain the observational evidence because they are predicted to saturate at a magnetic field level much higher than that expected for other electromagnetic streaming instabilities such as filamentation. They are thus able to amplify a seed magnetic field to the desired level for the particle acceleration process. While these modes are found for arbitrarily oriented wave vectors, they grow the most for flow aligned $\mathbf{k}$'s.[233]

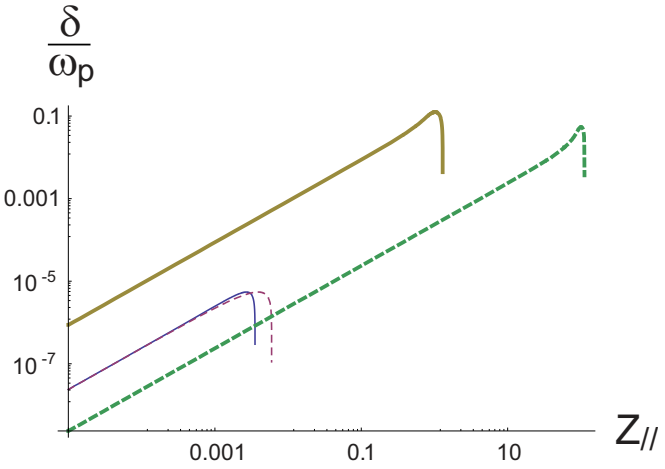

FIG. 44. (Color online) Growth rate of the flow aligned unstable modes for a cold proton beam with $\beta_b=0.4$ interacting with a cold plasma 100 times denser. A guiding magnetic field is accounted for such as $\omega_c=10^{-2}\omega_p$. Blue (thin plain): resonant Alfvén unstable modes. Purple (thin dashed): nonresonant Bell's unstable modes. Yellow (bold plain): Two-stream instability. Green (bold dashed): Buneman instability. The proton to electron mass ratio is 1836.

Figure 44 plots the growth rate of each unstable branch as a function of $Z_y=k_y v_b/\omega_p$ for $Z_\perp=Z_x=0$. The setup considered here consists of a nonrelativistic beam of protons interacting with a much denser plasma in the presence of a guiding magnetic field. The plasma electrons initially drift with the protons so as to cancel the net current. For these wave vectors, the dispersion equation can be cast under the form

$$\det\begin{vmatrix} a & d & 0 \\ -d & b & 0 \\ 0 & 0 & c \end{vmatrix} = 0, \tag{60}$$

which clearly factorizes into three branches $(ab+\imath d)(ab-\imath d)c=0$. The first two factors give rise to the low-k Alfvén and Bell's modes. The third branch $c=0$ yields two-stream

modes arising from the proton/proton interaction and Buneman modes between the electron and the background plasma. In spite of the fact that Bell's modes do not govern the spectrum, the orders of magnitude separating the two-stream/Buneman modes from the Alfvén/Bell modes certainly play a role. Two-stream and Buneman modes grow so rapidly, and on so small a scale-length, that they should saturate even before Bell's modes start "noticing" them. It is thus probable that the growth of the former modes simply results in mere heating of the plasma from the standpoint of the latter. Bell's modes have motivated many studies over the past years, and a number of theoretical[229,234] and numerical works[230,235,236] have now enriched the initial MHD theory.

The proton beam/plasma interaction is also relevant for the proton-driven FIS (Ref. 196) which has been proposed as a more robust alternative to the electron-driven FIS, owing to the higher ion inertia. This scheme proposes to exploit the recently discovered possibility of generating intense beams of high energy protons from the rear surface of solid targets irradiated by ultraintense lasers.[237–239] This option is being extensively investigated with the goal of designing the target and igniting beam parameters (see Ref. 240 and references therein). Stability issues were numerically addressed by Ruhl *et al.*[241] before an analytical kinetic treatment[242] found that flow aligned unstable modes should be completely stabilized under normal conditions.

VII. CONCLUSIONS

The linear and nonlinear processes ruling the evolution of a relativistic electron beam-plasma system have been reviewed. Three instability classes governing the early-time system's dynamics have been identified in the 2D **k**-space. Section II of this review explained the linear formalism needed to deal with arbitrarily oriented waves in the relativistic regime for a beam plasma system. Section III then focused on a current-neutralized relativistic electron beam. Ions were considered as fixed. The complete 2D unstable spectrum has been characterized for three kinds of distribution functions. The differences between filamentation and Weibel instabilities have been discussed, together with a full spectrum phase velocity analysis and the possibility of using a fluid formalism to deal with the problem. The hierarchy of the competing modes has been established in the system parameter space in Sec. IV both in the cold-fluid and kinetic regimes, using in the latter case waterbag and Maxwell–Jüttner distribution functions. Section V has dealt with PIC simulations. Theoretical predictions have been confronted to highly resolved, multimode simulations of the early evolution of large-scale beam-plasma setups. The main nonlinear structures generated by the saturated primary beam-plasma instabilities have been illustrated by reduced case studies and explained through simple reasoning.

To this stage, the reader may have noticed that a kinetic evaluation of the multidimensional spectrum accounting for some realistic distribution functions has only been achieved for the simplest case of an unmagnetized, fixed-ion, relativistic electron beam-plasma system. Given the number of alternate systems reviewed in Sec. VI, a considerable amount of work remains to be done. Besides the systematic approach consisting in dealing with these cases one by one, it could be possible to unify some of them. For example, the linear phase of the REB/Plasma case reviewed here is equivalent to a pair/pair collision as long as there is no external magnetic field. The reason is that the unmagnetized linear response only depends on the square of the particle charges. Since positrons and electrons have the same mass, a pair beam of electronic density n_b is equivalent to an electron beam of density $2n_b$. The second pair beam then plays the role of the return current with doubled density, and all the linear results exposed in Secs. III and IV can be readily applied, making sure the dimensionless coefficients from Eq. (19) are properly rescaled. Maybe it is possible to generalize this approach, by finding "classes" of equivalent systems. All setups pertaining to the same class would share the same linear phase, allowing thus for a drastic reduction of the overall calculations.

Giving up the assumption of an infinite and uniform system could allow for a deeper understanding of the beam-plasma physics relevant in the context of FIS and GRBs.[243] For it to be valid, this approximation first implies that the situation of interest be defined by scale-lengths much larger than the modulation scales of the unstable modes. While this condition is generally fulfilled for most of the collisionless electron-electron processes, it may be more easily violated for a system supporting collisional or Bell's modes (see Fig. 44).

Another limitation of the present review is its exclusive focus on initial-condition problems. For instance, as regards the FIS, a number of simulation studies have shown that the filamentation instability rapidly develops, and saturates, over a narrow region encompassing the laser absorption region.[48,56] A space-time model of the magnetic spraying of an electron beam injected through the front surface of a plasma would then match more closely the actual FIS parameters. A difficulty, however, would be to provide an accurate enough description of the fast electron source given the demonstrated coupling between the laser-acceleration process and the self-generated magnetic fluctuations.[56] A similar space-time model, further accounting for the filamentation-scattered beam distribution, would also prove most valuable for quantifying the subsequent growth of quasielectrostatic modes and the associated anomalous stopping power. Such a model could draw upon the dynamic quasilinear theories worked out to explain type III solar radio bursts.[244,245] In the GRB context, the aforementioned theoretical results are frequently applied to model the unstable processes arising within colliding plasma shells prior to the shock formation. But the concept of plasma shell collision necessarily implies that these shells have borders. Once they start interpenetrating, simulations reveal shocks emerging through each shell's borders,[246] at which location the uniformity assumption clearly fails. In this case, a space-time, finite-beam size theory could shed new light on the shock formation.

ACKNOWLEDGMENTS

The authors acknowledge the financial support by Vetenskapsrådet and by Project No. ENE2009-09276 of the Spanish Ministerio de Educación y Ciencia and Project No. PAI08-0182-3162 of the Consejería de Educación y Ciencia de la Junta de Comunidades de Castilla-La Mancha.

Thanks are due to Didier Bénisti, Cesar Huete, Marie-Christine Firpo, Erik Lefebvre, Mikhail Medvedev, Milos Milosavljevic, Ehud Nakar, Guy Pelletier, Roberto Piriz, Luis Silva, Anatoly Spitkovsky, Jean-Luc Vay, and Gustavo Wouchuk for useful discussions. The CALDER simulations were performed using the computing facilities of CEA/CCRT.

Finally, we are grateful to Claude Deutsch who has been willing to read the manuscript.

APPENDIX A: TENSOR ELEMENTS FOR 2D WATERBAG DISTRIBUTION FUNCTIONS

The tensor elements have been derived in Refs. 15 and 16 for monokinetic electron beams as well as waterbag distribution functions with nonrelativistic thermal spreads. For such functions, results for 2D and 3D momentum spaces are strictly equivalent. Albeit lengthy, closed-form expressions can also be worked out in the case of 2D waterbag space with arbitrarily large momentum spreads. Omitting for brevity subscripts defining beam or plasma components, the resulting tensor elements then read

$$\varepsilon_{kl} = \delta_{kl} + \sum_{\alpha} \frac{n_\alpha^2}{\omega^2}(\mathcal{A}_{kl} + k_x \mathcal{B}_{kl} + k_y \mathcal{C}_{kl}), \tag{A1}$$

with

$$\mathcal{A}_{xx} = -\frac{1}{2P_\perp}\ln\left[\frac{P+P_\parallel+\sqrt{1+(P+P_\parallel)^2+P_\perp^2}}{P-P_\parallel+\sqrt{1+(P-P_\parallel)^2+P_\perp^2}}\right], \tag{A2}$$

$$\mathcal{A}_{yy} = \frac{P-P_\parallel}{4PP_\parallel}\ln\left[\frac{P_\perp+\sqrt{1+(P-P_\parallel)^2+P_\perp^2}}{-P_\perp+\sqrt{1+(P-P_\parallel)^2+P_\perp^2}}\right] - \frac{P+P_\parallel}{4PP_\parallel}\ln\left[\frac{P_\perp+\sqrt{1+(P+P_\parallel)^2+P_\perp^2}}{-P_\perp+\sqrt{1+(P+P_\parallel)^2+P_\perp^2}}\right],$$

$$\mathcal{A}_{xy} = 0, \tag{A3}$$

$$\mathcal{B}_{xx} = \frac{P_\perp}{4P_\parallel\sqrt{1+P_\perp^2}}\left[\mathcal{F}_0\left(x, \frac{k_x P_\perp}{\sqrt{1+P_\perp^2}}, \omega, -k_y\right) - \mathcal{F}_0\left(x, -\frac{k_x P_\perp}{\sqrt{1+P_\perp^2}}, \omega, -k_y\right)\right]_{\sinh^{-1}(P-P_\parallel)/\sqrt{1+P_\perp^2}}^{\sinh^{-1}(P+P_\parallel)/\sqrt{1+P_\perp^2}}, \tag{A4}$$

$$\mathcal{B}_{yy} = \frac{\sqrt{1+P_\perp^2}}{4P_\perp P_\parallel}\left[\mathcal{F}_2\left(x, \frac{k_x P_\perp}{\sqrt{1+P_\perp^2}}, \omega, -k_y\right) - \mathcal{F}_2\left(x, -\frac{k_x P_\perp}{\sqrt{1+P_\perp^2}}, \omega, -k_y\right)\right]_{\sinh^{-1}(P-P_\parallel)/\sqrt{1+P_\perp^2}}^{\sinh^{-1}(P+P_\parallel)/\sqrt{1+P_\perp^2}}, \tag{A5}$$

$$\mathcal{B}_{xy} = -\frac{1}{4P_\parallel}\left[\mathcal{F}_1\left(x, \frac{k_x P_\perp}{\sqrt{1+P_\perp^2}}, \omega, -k_y\right) - \mathcal{F}_1\left(x, -\frac{k_x P_\perp}{\sqrt{1+P_\perp^2}}, \omega, -k_y\right)\right]_{\sinh^{-1}(P-P_\parallel)/\sqrt{1+P_\perp^2}}^{\sinh^{-1}(P+P_\parallel)/\sqrt{1+P_\perp^2}}, \tag{A6}$$

$$\mathcal{C}_{xx} = \frac{\sqrt{1+(P-P_\parallel)^2}}{4P_\perp P_\parallel}\left[\mathcal{F}_2\left(x, -\frac{k_y(P-P_\parallel)}{\sqrt{1+(P-P_\parallel)^2}}, \omega, -k_x\right)\right]_{-\sinh^{-1}P_\perp/\sqrt{1+(P-P_\parallel)^2}}^{\sinh^{-1}P_\perp/\sqrt{1+(P-P_\parallel)^2}} - \frac{\sqrt{1+(P+P_\parallel)^2}}{4P_\perp P_\parallel} \times\left[\mathcal{F}_2\left(x, -\frac{k_y(P+P_\parallel)}{\sqrt{1+(P+P_\parallel)^2}}, \omega, -k_x\right)\right]_{-\sinh^{-1}P_\perp/\sqrt{1+(P+P_\parallel)^2}}^{\sinh^{-1}P_\perp/\sqrt{1+(P+P_\parallel)^2}}, \tag{A7}$$

$$\mathcal{C}_{yy} = \frac{P-P_\parallel}{4P_\perp P_\parallel}\left[\mathcal{F}_0\left(x, -\frac{k_y(P-P_\parallel)}{\sqrt{1+(P-P_\parallel)^2}}, \omega, -k_x\right)\right]_{-\sinh^{-1}P_\perp/\sqrt{1+(P-P_\parallel)^2}}^{\sinh^{-1}P_\perp/\sqrt{1+(P-P_\parallel)^2}} - \frac{P+P_\parallel}{4P_\perp P_\parallel} \times\left[\mathcal{F}_0\left(x, -\frac{k_y(P+P_\parallel)}{\sqrt{1+(P+P_\parallel)^2}}, \omega, -k_x\right)\right]_{-\sinh^{-1}P_\perp/\sqrt{1+(P+P_\parallel)^2}}^{\sinh^{-1}P_\perp/\sqrt{1+(P+P_\parallel)^2}}, \tag{A8}$$

$$\mathcal{C}_{xy}=\frac{P-P_{\parallel}}{4P_{\perp}P_{\parallel}}\left[\mathcal{F}_1\left(x,-\frac{k_y(P-P_{\parallel})}{\sqrt{1+(P-P_{\parallel})^2}},\omega,-k_x\right)\right]_{-\sinh^{-1}P_{\perp}/\sqrt{1+(P-P_{\parallel})^2}}^{\sinh^{-1}P_{\perp}/\sqrt{1+(P-P_{\parallel})^2}}-\frac{P+P_{\parallel}}{4P_{\perp}P_{\parallel}}$$
$$\times\left[\mathcal{F}_1\left(x,-\frac{k_y(P+P_{\parallel})}{\sqrt{1+(P+P_{\parallel})^2}},\omega,-k_x\right)\right]_{-\sinh^{-1}P_{\perp}/\sqrt{1+(P+P_{\parallel})^2}}^{\sinh^{-1}P_{\perp}/\sqrt{1+(P+P_{\parallel})^2}}. \tag{A9}$$

The functions $\mathcal{F}_n(x,a,b,c)$ are determined by the indefinite integral

$$\mathcal{F}_n(x,a,b,c)=\int dx\frac{\sinh^n x}{a+b\cosh x+c\sinh x}. \tag{A10}$$

For $n=(0,1,2)$, we obtain

$$\mathcal{F}_0=\frac{2}{\sqrt{b^2-a^2-c^2}}\tan^{-1}\left[\frac{(b-a)\tanh\frac{x}{2}+c}{\sqrt{b^2-a^2-c^2}}\right], \tag{A11}$$

$$\mathcal{F}_1=\frac{cx}{c^2-b^2}-\frac{b}{c^2-b^2}\ln(a+b\cosh x+c\sinh x)$$
$$+\frac{2ac}{(c^2-b^2)\sqrt{b^2-a^2-c^2}}\tan^{-1}\left[\frac{(b-a)\tanh\frac{x}{2}-c}{\sqrt{b^2-a^2-c^2}}\right], \tag{A12}$$

$$\mathcal{F}_2=-\frac{a(b^2+c^2)x}{(b^2-c^2)^2}-\frac{c\cosh x}{b^2-c^2}+\frac{b\sinh x}{b^2-c^2}$$
$$+\frac{2abc}{(b^2-c^2)^2}\ln(a+b\cosh x+c\sinh x)$$
$$-2\frac{a^2(b^2+c^2)-b^2(b^2-c^2)}{(b^2-c^2)^2\sqrt{b^2-a^2-c^2}}\tan^{-1}\left[\frac{(b-a)\tanh\frac{x}{2}-c}{\sqrt{b^2-a^2-c^2}}\right]. \tag{A13}$$

APPENDIX B: STABILIZATION CONDITION FOR THE FILAMENTATION INSTABILITY WITHIN THE WATERBAG MODEL

From the tensor elements given in Appendix A, it is easy to derive the condition for stabilizing the filamentation instability. It writes

$$AB-C^2\le 0, \tag{B1}$$

where

$$A=\sum_{j=b,p}\omega_{pj}^2\left\{\frac{P_j-P_{j\parallel}}{4P_{j\perp}P_{j\parallel}}\ln\left[\frac{P_{j\perp}+\sqrt{1+P_{j\perp}^2+(P_j-P_{j\parallel})^2}}{-P_{j\perp}+\sqrt{1+P_{j\perp}^2+(P_j-P_{j\parallel})^2}}\right]-\frac{P_{jd}+P_{j\parallel}}{4P_{j\perp}P_{j\parallel}}\ln\left[\frac{P_{j\perp}+\sqrt{1+P_{j\perp}^2+(P_j+P_{j\parallel})^2}}{-P_{j\perp}+\sqrt{1+P_{j\perp}^2+(P_{jd}+P_{j\parallel})^2}}\right]\right.$$
$$\left.-\frac{1+P_{j\perp}^2}{4P_{j\perp}P_{j\parallel}}\ln\left[\frac{P_{jd}+P_{j\parallel}+\sqrt{1+P_{j\perp}^2+(P_j+P_{j\parallel})^2}}{P_j-P_{j\parallel}+\sqrt{1+P_{j\perp}^2+(P_j-P_{j\parallel})^2}}\right]+\frac{P_j+P_{j\parallel}}{4P_{j\perp}P_{j\parallel}}\sqrt{1+P_{j\perp}^2+(P_j+P_{j\parallel})^2}-\frac{P_j-P_{j\parallel}}{4P_{j\perp}P_{j\parallel}}\sqrt{1+P_{j\perp}^2+(P_j-P_{j\parallel})^2}\right\}, \tag{B2}$$

$$B=\sum_{j=b,p}\omega_{pj}^2\frac{1+P_{j\perp}^2}{4P_{j\perp}P_{j\parallel}}\left\{\ln\left[\frac{P_j+P_{j\parallel}+\sqrt{1+P_{j\perp}^2+(P_j+P_{j\parallel})^2}}{P_j-P_{j\parallel}+\sqrt{1+P_{j\perp}^2+(P_j-P_{j\parallel})^2}}\right]+\frac{P_j+P_{j\parallel}}{4P_{j\perp}P_{j\parallel}}\sqrt{1+P_{j\perp}^2+(P_j+P_{j\parallel})^2}\right.$$
$$\left.-\frac{P_j-P_{j\parallel}}{4P_{j\perp}P_{j\parallel}}\sqrt{1+P_{j\perp}^2+(P_j-P_{j\parallel})^2}\right\}, \tag{B3}$$

$$C=\sum_{j=b,p}\omega_{pj}^2\frac{P_{jd}}{P_{j\perp}^2}. \tag{B4}$$

[1] I. Langmuir, Phys. Rev. **26**, 585 (1925).
[2] R. J. Briggs, *Electron-Stream Interaction with Plasma* (MIT Press, Cambridge, MA, 1964).
[3] J. R. Pierce, J. Appl. Phys. **19**, 231 (1948).
[4] D. Bohm and E. P. Gross, Phys. Rev. **75**, 1851 (1949); **75**, 1864 (1949).
[5] B. D. Fried, Phys. Fluids **2**, 337 (1959).
[6] E. S. Weibel, Phys. Rev. Lett. **2**, 83 (1959).
[7] S. A. Bludman, K. M. Watson, and M. N. Rosenbluth, Phys. Fluids **3**, 747 (1960).
[8] K. M. Watson, S. A. Bludman, and M. N. Rosenbluth, Phys. Fluids **3**, 741 (1960).

[9] Y. B. Faĭnberg, V. D. Shapiro, and V. Shevchenko, Sov. Phys. JETP **30**, 528 (1970).
[10] L. I. Rudakov, Sov. Phys. JETP **32**, 1134 (1971).
[11] R. L. Ferch and R. N. Sudan, Plasma Phys. **17**, 905 (1975).
[12] L. O. Silva, R. A. Fonseca, J. W. Tonge, and W. B. Mori, Bull. Am. Phys. Soc. **46**, 205 (2001).
[13] T. Taguchi, T. M. Antonsen, Jr., and K. Mima, Comput. Phys. Commun. **164**, 269 (2004).
[14] A. Bret and C. Deutsch, Phys. Plasmas **13**, 042106 (2006).
[15] A. Bret, M.-C. Firpo, and C. Deutsch, Phys. Rev. E **70**, 046401 (2004).
[16] A. Bret, M.-C. Firpo, and C. Deutsch, Phys. Rev. E **72**, 016403 (2005).
[17] A. Bret, M.-C. Firpo, and C. Deutsch, Phys. Rev. Lett. **94**, 115002 (2005).
[18] A. Bret, L. Gremillet, D. Bénisti, and E. Lefebvre, Phys. Rev. Lett. **100**, 205008 (2008).
[19] L. Gremillet, D. Bénisti, E. Lefebvre, and A. Bret, Phys. Plasmas **14**, 040704 (2007).
[20] M. E. Dieckmann, J. T. Frederiksen, A. Bret, and P. Shukla, Phys. Plasmas **13**, 112110 (2006).
[21] J. T. Frederiksen and M. E. Dieckmann, Phys. Plasmas **15**, 094503 (2008).
[22] X. Kong, J. Park, C. Ren, Z. M. Sheng, and J. W. Tonge, Phys. Plasmas **16**, 032107 (2009).
[23] A. Karmakar, N. Kumar, A. Pukhov, O. Polomarov, and G. Shvets, Phys. Rev. E **80**, 016401 (2009).
[24] A. Bret, M.-C. Firpo, and C. Deutsch, Nucl. Instrum. Methods Phys. Res. A **544**, 427 (2005).
[25] R. B. Miller, *An Introduction to the Physics of Intense Charged Particle Beams* (Plenum, New York, 1982).
[26] R. N. Sudan, in *Handbook of Plasma Physics*, edited by M. N. Rosenbluth and R. Z. Galeev (North-Holland, Amsterdam, 1984), Vol. 2.
[27] S. Humphries, *Charged Particle Beams* (Wiley Interscience, New York, 1990).
[28] F. Califano, R. Prandi, F. Pegoraro, and S. V. Bulanov, Phys. Rev. E **58**, 7837 (1998).
[29] M. Karlický, Astrophys. J. **690**, 189 (2009).
[30] M. Lazar, R. Schlickeiser, R. Wielebinski, and S. Poedts, Astrophys. J. **693**, 1133 (2009).
[31] F. Califano, N. Attico, F. Pegoraro, G. Bertin, and S. Bulanov, Phys. Rev. Lett. **86**, 5293 (2001).
[32] S. Zenitani and M. Hesse, Phys. Plasmas **15**, 022101 (2008).
[33] S. Mrówczynski, Phys. Lett. B **214**, 587 (1988).
[34] M. Mannarelli and C. Manuel, Phys. Rev. D **76**, 094007 (2007).
[35] M. Tabak, J. Hammer, M. E. Glinsky, W. L. Kruer, S. C. Wilks, J. Woodworth, E. M. Campbell, M. D. Perry, and R. J. Mason, Phys. Plasmas **1**, 1626 (1994).
[36] M. Tabak, D. S. Clark, S. P. Hatchett, M. H. Key, B. F. Lasinski, R. A. Snavely, S. C. Wilks, R. P. J. Town, R. Stephens, E. M. Campbell, R. Kodama, K. Mima, K. A. Tanaka, S. Atzeni, and R. Freeman, Phys. Plasmas **12**, 057305 (2005).
[37] R. Kodama, P. A. Norreys, K. Mima, A. E. Dangor, R. G. Evans, H. Fujita, Y. Kitagawa, K. Krushelnick, T. Miyakoshi, N. Miyanaga, T. Norimatsu, S. J. Rose, T. Shozaki, K. Shigemori, A. Sunahara, M. Tampo, K. A. Tanaka, Y. Toyama, Y. Yamanaka, and M. Zepf, Nature (London) **412**, 798 (2001).
[38] A. R. Piriz, J. Sanz, and L. F. Ibanez, Phys. Plasmas **4**, 1117 (1997).
[39] A. L. Velikovich, J. P. Dahlburg, A. J. Schmitt, J. H. Gardner, L. Phillips, F. L. Cochran, Y. K. Chong, G. Dimonte, and N. Metzler, Phys. Plasmas **7**, 1662 (2000).
[40] J. D. Lindl, *Inertial Confinement Fusion: The Quest for Ignition and Energy Gain Using Indirect Drive* (Springer-Verlag, New York, 1998).
[41] C. Cavailler, Plasma Phys. Controlled Fusion **47**, B389 (2005).
[42] S. C. Wilks, W. L. Kruer, M. Tabak, and A. B. Langdon, Phys. Rev. Lett. **69**, 1383 (1992).
[43] A. Pukhov and J. Meyer-ter-Vehn, Phys. Rev. Lett. **79**, 2686 (1997).
[44] P. Norreys, R. Allott, R. J. Clarke, J. Collier, D. Neely, S. J. Rose, M. Zepf, M. Santala, A. R. Bell, K. Krushelnick, E. Dangor, N. C. Woolsey, R. G. Evans, H. Habara, T. Norimatsu, and R. Kodama, Phys. Plasmas **7**, 3721 (2000).
[45] R. J. Mason, Phys. Rev. Lett. **96**, 035001 (2006).
[46] C. Deutsch, H. Furukawa, K. Mima, M. Murakami, and K. Nishihara, Phys. Rev. Lett. **77**, 2483 (1996).
[47] S. Atzeni, Phys. Plasmas **6**, 3316 (1999).
[48] C. Ren, M. Tzoufras, J. Tonge, W. B. Mori, F. S. Tsung, M. Fiore, R. A. Fonseca, L. O. Silva, J. C. Adam, and A. Héron, Phys. Plasmas **13**, 056308 (2006).
[49] A. Pukhov and J. Meyer-ter Vehn, Phys. Rev. Lett. **76**, 3975 (1996).
[50] Y. Sentoku, K. Mima, S. Kojima, and H. Ruhl, Phys. Plasmas **7**, 689 (2000).
[51] M. Honda, J. Meyer-ter-Vehn, and A. Pukhov, Phys. Rev. Lett. **85**, 2128 (2000).
[52] L. O. Silva, R. A. Fonseca, J. W. Tonge, W. B. Mori, and J. M. Dawson, Phys. Plasmas **9**, 2458 (2002).
[53] Y. Sentoku, K. Mima, P. Kaw, and K. Nishikawa, Phys. Rev. Lett. **90**, 155001 (2003).
[54] J. M. Hill, M. H. Key, S. P. Hatchett, and R. R. Freeman, Phys. Plasmas **12**, 082304 (2005).
[55] M. Tzoufras, C. Ren, F. S. Tsung, J. W. Tonge, W. B. Mori, M. Fiore, R. A. Fonseca, and L. O. Silva, Phys. Rev. Lett. **96**, 105002 (2006).
[56] J. C. Adam, A. Héron, and G. Laval, Phys. Rev. Lett. **97**, 205006 (2006).
[57] L. A. Cottrill, A. B. Langdon, B. F. Lasinski, S. M. Lund, K. Molvig, M. Tabak, R. P. J. Town, and E. A. Williams, Phys. Plasmas **15**, 082108 (2008).
[58] O. Polomarov, I. Kaganovich, and G. Shvets, Phys. Rev. Lett. **101**, 175001 (2008).
[59] K. Molvig, Phys. Rev. Lett. **35**, 1504 (1975).
[60] L. Gremillet, G. Bonnaud, and F. Amiranoff, Phys. Plasmas **9**, 941 (2002).
[61] M. Fiore, L. Silva, C. Ren, M. Tzoufras, and W. Mori, Mon. Not. R. Astron. Soc. **372**, 1851 (2006).
[62] *Unsolved Problems in Astrophysics*, edited by J. N. Bahcall and J. P. Ostriker (Princeton University Press, Princeton, 1997).
[63] G. Krymskii, Dokl. Akad. Nauk SSSR **234**, 1306 (1977).
[64] R. Blandford and J. Ostriker, Astrophys. J. **221**, L29 (1978).
[65] A. R. Bell, Mon. Not. R. Astron. Soc. **182**, 147 (1978).
[66] A. R. Bell, Mon. Not. R. Astron. Soc. **182**, 443 (1978).
[67] W. Axford, E. Leer, and G. Skadron, Proceedings of the 15th International Cosmic Ray Conference (Bulgarian Academy of Sciences, Plovdiv, 1977), Vol. 11, p. 132.
[68] R. M. Kulsrud, Phys. Plasmas **2**, 1735 (1995).
[69] R. M. Kulsrud, *Plasma Physics for Astrophysics* (Princeton University Press, Princeton, NJ, 2005).
[70] W. Axford, Proceedings of the 17th International Cosmic Ray Conference (Centre d'etudes Nucleaires, Saclay, Gif-sur-Yvette, Paris, France, 1981), Vol. 12, p. 155.
[71] L. O. C. Drury, Rep. Prog. Phys. **46**, 973 (1983).
[72] R. Blandford and D. Eichler, Phys. Rep. **154**, 1 (1987).
[73] L. O. Silva, R. A. Fonseca, J. W. Tonge, J. M. Dawson, W. B. Mori, and M. V. Medvedev, Astrophys. J. **596**, L121 (2003).
[74] J. T. Frederiksen, C. B. Hededal, T. Haugbolle, and A. Nordlund, Astrophys. J. **608**, L13 (2004).
[75] M. E. Dieckmann, P. K. Shukla, and L. O. C. Drury, Astrophys. J. **675**, 586 (2008).
[76] A. Spitkovsky, Astrophys. J. Lett. **673**, L39 (2008).
[77] S. Martins, R. Fonseca, L. Silva, and W. Mori, Astrophys. J. Lett. **695**, L189 (2009).
[78] T. Piran, Rev. Mod. Phys. **76**, 1143 (2005).
[79] E. Nakar, Phys. Rep. **442**, 166 (2007).
[80] M. V. Medvedev, Astrophys. J. **540**, 704 (2000).
[81] J. G. Kirk and B. Reville, Astrophys. J. Lett. **710**, L16 (2010).
[82] M. V. Medvedev and A. A. Loeb, Astrophys. J. **526**, 697 (1999).
[83] T. N. Kato and H. Takabe, Astrophys. J. Lett. **681**, L93 (2008).
[84] C. K. Birdsall and A. B. Langdon, *Plasma Physics via Computer Simulation* (McGraw-Hill, New York, 1985).
[85] J. M. Dawson, Rev. Mod. Phys. **55**, 403 (1983).
[86] K. V. Roberts and H. L. Berk, Phys. Rev. Lett. **19**, 297 (1967).
[87] J. M. Dawson and R. Shanny, Phys. Fluids **11**, 1506 (1968).
[88] R. Morse and C. Nielson, Phys. Rev. Lett. **23**, 1087 (1969).
[89] R. C. Davidson, N. A. Krall, K. Papadopoulos, and R. Shanny, Phys. Rev. Lett. **24**, 579 (1970).
[90] R. Davidson, I. Haber, and D. Hammer, Phys. Lett. A **34**, 235 (1971).
[91] R. C. Davidson, D. A. Hammer, I. Haber, and C. E. Wagner, Phys. Fluids **15**, 317 (1972).
[92] R. Lee and M. Lampe, Phys. Rev. Lett. **31**, 1390 (1973).
[93] L. E. Thode and R. N. Sudan, Phys. Fluids **18**, 1552 (1975).
[94] L. Yin, B. J. Albright, H. A. Rose, K. J. Bowers, B. Bergen, D. S. Montgomery, J. L. Kline, and J. C. Fernandez, Phys. Plasmas **16**, 113101 (2009).
[95] R. Courant, K. Friedrichs, and H. Lewy, Math. Ann. **100**, 32 (1928).

[96]T. Takizuka and H. Abe, J. Comput. Phys. **25**, 205 (1977).
[97]M. Jones, D. Lemons, R. Mason, V. Thomas, and D. Winske, J. Comput. Phys. **123**, 169 (1996).
[98]C. McKinstrie, Phys. Fluids **31**, 1273 (1988).
[99]S. Ichimaru, *Basic Principles of Plasma Physics* (W. A. Benjamin, Reading, MA, 1973).
[100]P. Clemmow and J. Dougherty, *Electrodynamics of Particles and Plasmas* (Addison-Wesley, Reading, MA, 1990).
[101]R. C. Davidson, in *Handbook of Plasma Physics*, edited by M. N. Rosenbluth and R. Z. Galeev (North-Holland, Amsterdam, 1983), Vol. 1.
[102]P. Yoon, Phys. Plasmas **14**, 064504 (2007).
[103]R. C. Tautz and R. Schlickeiser, Phys. Plasmas **14**, 102102 (2007).
[104]J. R. Cary, L. E. Thode, D. S. Lemons, M. E. Jones, and M. A. Mostrom, Phys. Fluids **24**, 1818 (1981).
[105]P. H. Yoon and R. C. Davidson, Phys. Rev. A **35**, 2718 (1987).
[106]P. H. Yoon, Phys. Fluids B **1**, 1336 (1989).
[107]U. Schaefer-Rolffs, I. Lerche, and R. Schlickeiser, Phys. Plasmas **13**, 012107 (2006).
[108]A. Achterberg and J. Wiersma, Astron. Astrophys. **475**, 1 (2007).
[109]U. Schaefer-Rolffs and R. C. Tautz, Phys. Plasmas **15**, 062105 (2008).
[110]A. Bret, L. Gremillet, and D. Bénisti, Phys. Rev. E **81**, 036402 (2010).
[111]H. Lee and L. E. Thode, Phys. Fluids **26**, 2707 (1983).
[112]F. Califano, F. Pegoraro, and S. V. Bulanov, Phys. Rev. E **56**, 963 (1997).
[113]F. Califano, F. Pegoraro, S. V. Bulanov, and A. Mangeney, Phys. Rev. E **57**, 7048 (1998).
[114]T. Okada and W. Schmidt, J. Plasma Phys. **37**, 373 (1987).
[115]C. Deutsch, A. Bret, M.-C. Firpo, and P. Fromy, Phys. Rev. E **72**, 026402 (2005).
[116]F. Pegoraro, S. V. Bulanov, F. Califano, and M. Lontano, Phys. Scr., T **T63**, 262 (1996).
[117]A. Bret, L. Gremillet, and J. C. Bellido, Phys. Plasmas **14**, 032103 (2007).
[118]R. C. Tautz and R. Schlickeiser, Phys. Plasmas **12**, 122901 (2005).
[119]R. C. Tautz and R. Schlickeiser, Phys. Plasmas **13**, 062901 (2006).
[120]M. Lazar, R. Schlickeiser, and P. K. Shukla, Phys. Plasmas **13**, 102107 (2006).
[121]M. Lazar, R. Schlickeiser, and P. K. Shukla, Phys. Plasmas **15**, 042103 (2008).
[122]M. Lazar, R. Schlickeiser, S. Poedts, and R. C. Tautz, Mon. Not. R. Astron. Soc. **390**, 168 (2008).
[123]M. Lazar, R. C. Tautz, R. Schlickeiser, and S. Poedts, Mon. Not. R. Astron. Soc. **401**, 362 (2010).
[124]D. Cubero, J. Casado-Pascual, J. Dunkel, P. Talkner, and P. Hänggi, Phys. Rev. Lett. **99**, 170601 (2007).
[125]T.-Y. B. Yang, Y. Gallant, J. Arons, and A. Langdon, Phys. Fluids B **5**, 3369 (1993).
[126]T.-Y. B. Yang, J. Arons, and A. B. Langdon, Phys. Plasmas **1**, 3059 (1994).
[127]A. Stockem, M. E. Dieckmann, and R. Schlickeiser, Plasma Phys. Controlled Fusion **51**, 075014 (2009).
[128]M. Tzoufras, C. Ren, F. S. Tsung, J. W. Tonge, W. B. Mori, M. Fiore, R. A. Fonseca, and L. O. Silva, Phys. Plasmas **14**, 062108 (2007).
[129]R. C. Tautz, I. Lerche, R. Schlickeiser, and U. Schaefer-Rolffs, J. Phys. A **39**, 13831 (2006).
[130]R. C. Tautz and I. Lerche, J. Phys. A **39**, 14833 (2006).
[131]R. C. Tautz, J.-I. Sakai, and I. Lerche, Astrophys. Space Sci. **310**, 159 (2007).
[132]R. C. Tautz and I. Lerche, J. Phys. A **40**, F677 (2007).
[133]B. B. Godfrey, W. R. Shanahan, and L. E. Thode, Phys. Fluids **18**, 346 (1975).
[134]A. Bret and C. Deutsch, Phys. Plasmas **12**, 082704 (2005).
[135]A. Bret, Europhys. Lett. **74**, 1027 (2006).
[136]A. Bret and C. Deutsch, Phys. Plasmas **13**, 022110 (2006).
[137]F. Jüttner, Ann. Phys. **339**, 856 (1911).
[138]G. Amelino-Camelia, Nature (London) **450**, 801 (2007).
[139]P. Wright and G. Hadley, Phys. Rev. A **12**, 686 (1975).
[140]G. Benford, Phys. Rev. Lett. **28**, 1242 (1972).
[141]G. Benford, Plasma Phys. **15**, 483 (1973).
[142]R. C. Davidson, B. H. Hui, and C. A. Kapetanakos, Phys. Fluids **18**, 1040 (1975).
[143]G. Rowlands, M. E. Dieckmann, and P. K. Shukla, New J. Phys. **9**, 247 (2007).
[144]R. Schlickeiser and P. K. Shukla, Astrophys. J. Lett. **599**, L57 (2003).
[145]F. Califano, D. Del Sarto, and F. Pegoraro, Phys. Rev. Lett. **96**, 105008 (2006).
[146]B. G. Kalman, C. Montes, and D. Quemada, Phys. Fluids **11**, 1797 (1968).
[147]B. Hao, Z.-M. Sheng, and J. Zhang, Phys. Plasmas **15**, 082112 (2008).
[148]B. Hao, Z.-M. Sheng, C. Ren, and J. Zhang, Phys. Rev. E **79**, 046409 (2009).
[149]A. Stockem and M. Lazar, Phys. Plasmas **15**, 014501 (2008).
[150]M. Lazar, A. Smolyakov, R. Schlickeiser, and P. K. Shukla, J. Plasma Phys. **75**, 19 (2009).
[151]A. Stockem, M. Lazar, P. K. Shukla, and A. Smolyakov, J. Plasma Phys. **75**, 529 (2009).
[152]A. B. Mikhailovskii, *Theory of Plasma Instabilities* (Consultant Bureau, New York, 1974), Vol. 1.
[153]J. Neufeld and P. H. Doyle, Phys. Rev. **121**, 654 (1961).
[154]Y. Kazimura, J. Sakai, T. Neubert, and S. Bulanov, Astrophys. J. **498**, L183 (1998).
[155]M. Honda, Phys. Rev. E **69**, 016401 (2004).
[156]G. O. Ludwig, Plasma Phys. Controlled Fusion **49**, 1521 (2007).
[157]Shafiq-ur-Rehman,, X. Wang, and Y. Liu, Phys. Plasmas **15**, 042701 (2008).
[158]S. Rehman, W. Xiaogang, L. Jian, L. Yian, and L. Yue, Plasma Sci. Technol. **11**, 661 (2009).
[159]A. Karmakar, N. Kumar, G. Shvets, O. Polomarov, and A. Pukhov, Phys. Rev. Lett. **101**, 255001 (2008).
[160]J. G. Siambis, Phys. Fluids **22**, 1372 (1979).
[161]F. Pegoraro and F. Porcelli, Phys. Fluids **27**, 1665 (1984).
[162]S. M. Mahajan and R. D. Hazeltine, Phys. Plasmas **9**, 1882 (2002).
[163]B. A. Shadwick, G. M. Tarkenton, and E. H. Esarey, Phys. Rev. Lett. **93**, 175002 (2004).
[164]A. Bret, M. E. Dieckmann, and C. Deutsch, Phys. Plasmas **13**, 082109 (2006).
[165]I. V. Timofeev, K. V. Lotov, and A. V. Terekhov, Phys. Plasmas **16**, 063101 (2009).
[166]L. O. Silva, *Relativistic Jets: The Common Physics of AGN, Microquasars and Gamma-ray Bursts* (AIP, Ann Arbor, Michigan, 2006), pp. 109–128.
[167]P. A. Norreys, F. N. Beg, Y. Sentoku, L. O. Silva, R. A. Smith, and R. M. G. M. Trines, Phys. Plasmas **16**, 041002 (2009).
[168]T. M. O'Neil, J. H. Winfrey, and J. H. Malmberg, Phys. Fluids **14**, 1204 (1971).
[169]T. M. O'Neil and J. H. Winfrey, Phys. Fluids **15**, 1514 (1972).
[170]K. Papadopoulos, Phys. Fluids **18**, 1769 (1975).
[171]H. P. Freund, I. Haber, P. Palmadesso, and K. Papadopoulos, Phys. Fluids **23**, 518 (1980).
[172]I. B. Bernstein, J. M. Greene, and M. D. Kruskal, Phys. Rev. **108**, 546 (1957).
[173]W. E. Drummond, J. H. Malmberg, T. M. O'Neil, and J. R. Thompson, Phys. Fluids **13**, 2422 (1970).
[174]W. M. Manheimer, Phys. Fluids **14**, 579 (1971).
[175]L. E. Thode, Phys. Fluids **19**, 305 (1976).
[176]W. L. Kruer and J. M. Dawson, Phys. Fluids **13**, 2747 (1970).
[177]M. V. Goldman, Phys. Fluids **13**, 1281 (1970).
[178]C. B. Wharton, J. H. Malmberg, and T. M. O'Neil, Phys. Fluids **11**, 1761 (1968).
[179]A. Luque and H. Schamel, Phys. Rep. **415**, 261 (2005).
[180]L. Muschietti, I. Roth, C. W. Carlson, and R. Ergun, Phys. Rev. Lett. **85**, 94 (2000).
[181]S. D. Bale, P. J. Kellogg, D. E. Larson, R. P. Lin, K. Goetz, and R. P. Lepping, Geophys. Res. Lett. **25**, 2929, doi:10.1029/98GL02111 (1998).
[182]G. Sarri, M. E. Dieckmann, C. R. D. Brown, C. A. Cecchetti, D. J. Hoarty, S. F. James, R. Jung, I. Kourakis, H. Schamel, O. Willi, and M. Borghesi, Phys. Plasmas **17**, 010701 (2010).
[183]R. Morse and C. Nielson, Phys. Fluids **14**, 830 (1971).
[184]M. E. Dieckmann, Plasma Phys. Controlled Fusion **51**, 124042 (2009).
[185]J. Wiersma and A. Achterberg, Astron. Astrophys. **428**, 365 (2004).
[186]Y. Lyubarsky and D. Eichler, Astrophys. J. **647**, 1250 (2006).
[187]V. Y. Mart'yanov, V. V. Kocharovsky, and V. V. Kocharovsky, Sov. Phys. JETP **107**, 1225 (2008).
[188]M. Medvedev, M. Fiore, R. Fonseca, L. Silva, and W. Mori, Astrophys. J. **618**, L75 (2005).
[189]D. A. Hammer and N. Rostoker, Phys. Fluids **13**, 1831 (1970).
[190]J. Sakai, S. Saito, H. Mae, D. Farina, M. Lontano, F. Califano, F.

Pegoraro, and S. V. Bulanov, Phys. Plasmas **9**, 2959 (2002).
[191]J. W. Eastwood, Comput. Phys. Commun. **64**, 252 (1991).
[192]M. E. Dieckmann, B. Eliasson, and P. K. Shukla, Phys. Plasmas **11**, 1394 (2004).
[193]F. Califano, T. Cecchi, and C. Chiuderi, Phys. Plasmas **9**, 451 (2002).
[194]P. Chang, A. Spitkovsky, and J. Arons, Astrophys. J. **674**, 378 (2008).
[195]C. Deutsch, A. Bret, M.-C. Firpo, L. Gremillet, E. Lefebvre, and A. Lifschitz, Laser Part. Beams **26**, 157 (2008).
[196]M. Roth, T. E. Cowan, M. H. Key, S. P. Hatchett, C. Brown, W. Fountain, J. Johnson, D. M. Pennington, R. A. Snavely, S. C. Wilks, K. Yasuike, H. Ruhl, F. Pegoraro, S. V. Bulanov, E. M. Campbell, M. D. Perry, and H. Powell, Phys. Rev. Lett. **86**, 436 (2001).
[197]H. Ruhl, A. Macchi, P. Mulser, F. Cornolti, and S. Hain, Phys. Rev. Lett. **82**, 2095 (1999).
[198]A. Stockem, M. E. Dieckmann, and R. Schlickeiser, Plasma Phys. Controlled Fusion **50**, 025002 (2008).
[199]A. Bret and M. E. Dieckmann, Phys. Plasmas **15**, 062102 (2008).
[200]L. Sironi and A. Spitkovsky, Astrophys. J. **698**, 1523 (2009).
[201]A. Bret and M. E. Dieckmann, Phys. Plasmas **15**, 012104 (2008).
[202]O. Buneman, Phys. Rev. **115**, 503 (1959).
[203]R. Lovelace and R. Sudan, Phys. Rev. Lett. **27**, 1256 (1971).
[204]F. Haas, Phys. Plasmas **15**, 022104 (2008).
[205]L. N. Tsintsadze, Phys. Plasmas **16**, 094507 (2009).
[206]F. Haas, P. Shukla, and B. Eliasson, J. Plasma Phys. **75**, 251 (2009).
[207]F. Haas and M. Lazar, Phys. Rev. E **77**, 046404 (2008).
[208]F. Haas, G. Manfredi, and M. Feix, Phys. Rev. E **62**, 2763 (2000).
[209]A. Bret and F. Haas, Phys. Plasmas **17**, 052101 (2010).
[210]G. Manfredi and F. Haas, Phys. Rev. B **64**, 075316 (2001).
[211]F. Haas, Phys. Plasmas **12**, 062117 (2005).
[212]B. Eliasson and P. K. Shukla, Phys. Scr. **78**, 025503 (2008).
[213]A. Bret, Phys. Plasmas **14**, 084503 (2007).
[214]A. Bret, Phys. Plasmas **15**, 022109 (2008).
[215]H. Ren, Z. Wu, J. Cao, and P. K. Chu, Phys. Lett. A **372**, 2676 (2008).
[216]S. Ali and P. K. Shukla, Eur. Phys. J. D **41**, 319 (2007).
[217]A. Bret, F. J. Marín-Fernández, and J. M. Anfray, Plasma Phys. Controlled Fusion **51**, 075011 (2009).
[218]A. Bret and C. Deutsch, Phys. Plasmas **12**, 082109 (2005).
[219]E. Epperlein, Plasma Phys. Controlled Fusion **27**, 1027 (1985).
[220]B. Vermersch and L. Gremillet, private communication (2010).
[221]I. P. Shkarofsky, T. W. Johnston, and M. P. Bachynski, *The Particle Kinetics of Plasmas* (Addison-Wesley, Reading, MA, 1966).
[222]A. Bret, Laser Part. Beams **28**, 491 (2010).
[223]J. J. Honrubia and Y. Meyer-ter-Vehn, Nucl. Fusion **46**, L25 (2006).
[224]A. Bret, Astrophys. J. **699**, 990 (2009).
[225]A. Spitkovsky, Astrophys. J. Lett. **682**, L5 (2008).
[226]M. Michno and R. Schlickeiser, Astrophys. J. **714**, 868 (2010).
[227]R. U. Abbasi, T. Abu-Zayyad, M. Al-Seady, M. Allen, J. F. Amman, R. J. Anderson, G. Archbold, K. Belov, J. W. Belz, D. R. Bergman, S. A. Blake, O. A. Brusova, G. W. Burt, C. Cannon, Z. Cao, W. Deng, Y. Fedorova, C. B. Finley, R. C. Gray, W. F. Hanlon, C. M. Hoffman, M. H. Holzscheiter, G. Hughes, P. Hüntemeyer, D. Ivanov, B. F. Jones, and C. C. H. Jui, Phys. Rev. Lett. **104**, 161101 (2010).
[228]B. Reville, J. G. Kirk, and P. Duffy, Plasma Phys. Controlled Fusion **48**, 1741 (2006).
[229]E. Amato and P. Blasi, Mon. Not. R. Astron. Soc. **392**, 1591 (2009).
[230]M. A. Riquelme and A. Spitkovsky, Astrophys. J. **694**, 626 (2009).
[231]M. Lemoine and G. Pelletier, Mon. Not. R. Astron. Soc. **402**, 321 (2010).
[232]A. Bell, Mon. Not. R. Astron. Soc. **353**, 550 (2004).
[233]A. Bell, Mon. Not. R. Astron. Soc. **358**, 181 (2005).
[234]E. G. Zweibel and J. E. Everett, Astrophys. J. **709**, 1412 (2010).
[235]V. N. Zirakashvili, V. S. Ptuskin, and H. J. Völk, Astrophys. J. **678**, 255 (2008).
[236]J. Niemiec, M. Pohl, T. Stroman, and K.-I. Nishikawa, Astrophys. J. **684**, 1174 (2008).
[237]B. Hegelich, B. Albright, J. Cobble, K. Flippo, S. Letzring, M. Paffett, H. Ruhl, J. Schreiber, R. Schulze, and J. Fernandez, Nature (London) **439**, 441 (2006).
[238]T. Toncian, M. Borghesi, J. Fuchs, E. d'Humieres, P. Antici, P. Audebert, E. Brambrink, C. Cecchetti, A. Pipahl, L. Romagnani, and O. Willi, Science **312**, 410 (2006).
[239]H. Schwoerer, S. Pfotenhauer, O. Jackel, K. Amthor, B. Liesfeld, W. Ziegler, R. Sauerbrey, K. Ledingham, and T. Esirkepov, Nature (London) **439**, 445 (2006).
[240]M. Roth, Plasma Phys. Controlled Fusion **51**, 014004 (2009).
[241]H. Ruhl, T. Cowan, J. Dahlburg, P. Parks, and R. Stephens, Nucl. Fusion **44**, 438 (2004).
[242]A. Bret, Phys. Plasmas **16**, 094505 (2009).
[243]M.-C. Firpo, A. F. Lifschitz, E. Lefebvre, and C. Deutsch, Phys. Rev. Lett. **96**, 115004 (2006).
[244]V. V. Zaitsev, N. A. Mityakov, and V. O. Rapoport, Sol. Phys. **24**, 444 (1972).
[245]G. Foroutan, B. Li, P. Robinson, I. Cairns, and M. Moslehi-Fard, Phys. Plasmas **12**, 042905 (2005).
[246]M. E. Dieckmann, G. C. Murphy, A. Meli, and L. O. C. Drury, Astron. Astrophys. **509**, A89 (2010).